Important Notice

UNIVERSITY OF CALGARY

Seismic Azimuthal Anisotropy and Fracture Analysis from PP Reflection Data

by

Ye Zheng

A THESIS

SUBMITTED TO THE FACULTY OF GRADUATE STUDIES

IN PARTIAL FULFILMENT OF THE REQUIREMENTS FOR THE

DEGREE OF DOCTOR OF PHILOSOPHY

DEPARTMENT OF GEOLOGY AND GEOPHYSICS

CALGARY, ALBERTA

MARCH, 2006

UNIVERSITY OF CALGARY

FACULTY OF GRADUATE STUDIES

The undersigned certify that they have read, and recommend to the Faculty of Graduate Studies for acceptance, a thesis entitled "Seismic Azimuthal Anisotropy and Fracture Analysis from PP Reflection Data" submitted by Ye Zheng in partial fulfilment of the requirements of the degree of doctor of philosophy.

Supervisor, Dr. Don. C. Lawton Department of Geology and Geophysics University of Calgary	Co-supervisor, Dr. John Bancroft Department of Geology and Geophysics University of Calgary
Dr. Larry R. Lines Department of Geology and Geophysics University of Calgary	Dr. Robert Brady Department of Geology and Geophysics University of Calgary
Dr. Nigel Shrive Department of Civil Engineering University of Calgary	Dr. Mauricio Sacchi Department of Physics University of Alberta

_____

Date

Abstract

Many of the reservoirs, such as carbonates, tight clastics and basement reservoirs, are often fractured. In oil and gas exploration and development, one may require the delineation of the distribution and orientation of fractures. Fractures can not only provide pore space to hold oil and gas in place, but can also increase permeability to provide a pathway for fluid flowing from reservoir to well locations. There are three existing methods for extracting fracture information from PP seismic data. They are: (1) NMO velocity method, (2) residual moveout method, and (3) amplitude method. Each of them has advantages and disadvantages.

All three existing methods have some limitations, as some factors influence the precision and accuracy of the results of fracture analysis. A dipping reflector may induce "false" azimuthal anisotropy of the seismic amplitudes. Furthermore, in structural areas, detecting fractures from unmigrated CMP gathers will misposition fracture information. Therefore, migration must be incorporated into fracture analysis. Because the widely used common-offset migration will smear the incident angles, prestack common-angle time migration was developed in this dissertation and tested on synthetic and field data. The prestack common-angle migration solves smearing of incident angle, mispositioning and anisotropy induced by dipping reflectors simultaneously.

A new method, δ inversion, was developed. It is an integration of the NMO velocity method and the moveout method for extracting Thomsen's parameter, $\delta^{(v)}$, from the residual moveout on the bottom of the fractured layer.

A practical workflow for fracture analysis using PP reflection data is presented in this dissertation. Both the amplitude method and the δ inversion are employed in the workflow. The amplitude method gives detailed information on every time sample. In contrast, the δ inversion gives the information for the entire fractured layer. This workflow was successfully applied to both physical modeling data and field data. The results match the original model and the well production rates.

Acknowledgements

I would like to thank my supervisors, John Bancroft and Don Lawton for their guidance and help on the research for my PhD program. Although I was not on campus regularly as I was working downtown fulltime during the past years, they gave me great help on my research and correction of my dissertation.

I also want to thank Veritas DGC Inc. for the permission to use computer system and the Pinedale data set for my research. Thanks to my colleagues, David Gray, David Wilkinson, Dragana Todorovic-Marinic and Tyrone Deane for their help. David Gray is the person who raised my interest in the area of AVO and fracture analysis, and his help is unforgettable.

Thanks to Shangxu Wang of the Petroleum University of China, Xiangyang Li of the Edinburgh Anisotropy Project, and the Geophysical Key Lab, China National Petroleum Corporation, for the permission to use their physical modeling data set. Without the modeling data, my PhD program would not been completed in time. Thanks also to Michael Kendall and James Wookey of the University of Leeds, UK, for allowing me to use their numerical modeling package ATRAK, and to Glenn Larson and Devon Canada Corporation for providing seismic data and geophysical/geological interpretation in the associated area.

The important support for my work came from my family, my dear wife, Ying, and daughter, Dana. They are the first readers of my dissertation and gave me many great suggestions. They deserve special thanks.

Table of Contents

List of Tables

List of Figures and Illustrations

List of Symbols and Abbreviations

A	AVO intercept
B	AVO gradient
B^{ani}	anisotropic AVO gradient
B^{iso}	isotropic AVO gradient
D	Fracture reflectivity
h	half source-receiver offset
t	travel time
t_0	zero offset two way travel time
V	seismic velocity
V_{nmo}	NMO velocity
V_{rms}	RMS velocity
V_p	P wave velocity
V_s	S wave velocity
β	dip angle
β^*	apparent dip angle
Δ	difference
$\varepsilon, \delta, \gamma$	Thomsen's anisotropic parameters
$\varepsilon^{(v)}, \delta^{(v)}, \gamma^{(v)}$	Thomsen's anisotropic parameters for HTI media
θ	incident angle
ρ	bulk density
λ, μ	Lamé elastic moduli
φ	azimuth angle

AA	Azimuthal Anisotropy
AGC	Automatical Gain Control
AVO	Amplitude Variations with Offset
CMP	Common Mid-Point
HTI	Horizontal Transverse Isotropy

NMO	Normal MoveOut
P wave	compressional wave
PP	reflected P wave from an incident P wave
PS	converted S wave from an incident P wave
RMS	Root Mean Square
S wave	shear wave
TTI	Tilted Transverse Isotropy
VTI	Vertical Transverse Isotropy

Chapter One: Introduction

1.1 Introduction to fractures and fracture analysis

The increasing demand of oil and gas in the world makes geoscientists put a lot of effort into the exploration of different kinds of hydrocarbon reservoirs. Many of the reservoirs, such as carbonates, tight clastics and basement reservoirs, are often fractured. Fractures play important roles in hydrocarbon production. They may have a positive or negative impact on hydrocarbon production. They can provide pore space in reservoir rocks to hold oil and gas in place, and also increase the permeability of the reservoir rocks for oil and gas to flow easily to well bores. On the other hand, cemented or mineralized fractures may act as barriers of fluid flow (Nelson, 2001; Aguilera, 1995). Consequently, the distribution and orientation of fractures are important for geophysicists, geologists and reservoir engineers to evaluate the reservoir and make development plans.

Reservoir fractures are naturally occurring macroscopic planar discontinuities in rocks due to deformation or physical diagenesis (Nelson, 2001). Fractures can be classified as shear fractures, extension fractures and tension fractures according to the movement of the matrix walls on the two sides of the fractures and the nature of the stress that causes fracturing. Shear fractures are those whose matrix walls are parallel to each other but move in opposite directions. They are parallel to the intermediate principal stress axis and angular to the maximum principal stress axis. Extension fractures are those whose matrix walls move away from each other and perpendicular to the plane of the fractures. They are parallel to both maximum and intermediate principal stress axes. Tension fractures are similar to extension fractures, but the minimum principal stress is tensile (Aguilera, 1995). Figure 1.1 shows these three types of fracture and their relationship with principal stresses.

The pattern of the fractures reflects the state of the stress when fracturing occurred. It may be not linked to the current stress field. During long geological times, it is very likely that rocks were fractured more than once under different stress fields with different principal directions. Therefore, the overall fracture system can be very complex. However, the stress field within the Earth at present time causes fractures to open in the maximum stress direction and to close perpendicular to this direction (Crampin and Leary, 1993; Crampin, 2000). In other words, the open fractures may be aligned under the condition of the current stress field. Open fractures are of interest for hydrocarbon exploration, since they can provide storage space and passage for flow of oil and gas.

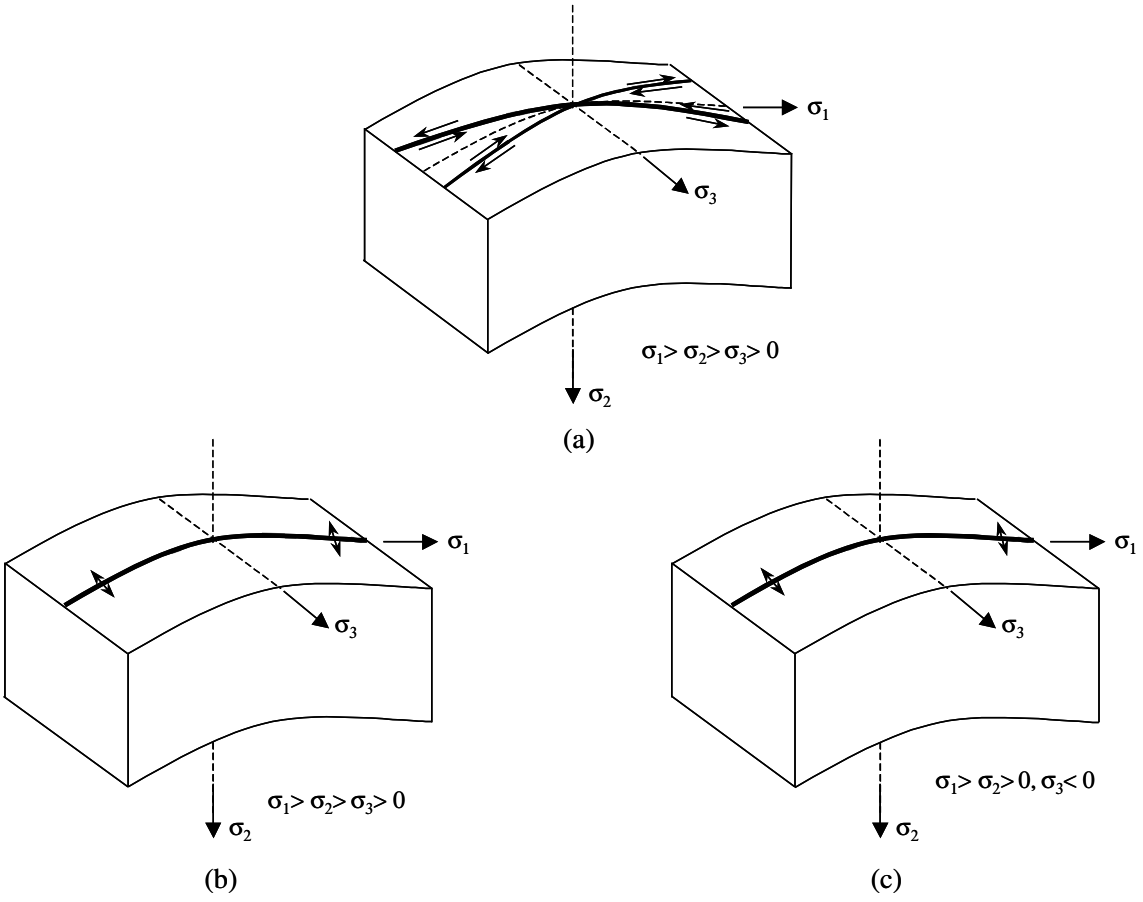

Figure 1.1 Different types of fracture and their relationship with principal stresses. (a) shear fracture; (b) extension fracture and (c) tensile fracture (compressional stress is defined as positive).

Fractures can be measured directly by well logging or by checking core samples. However, these measurements can only be applied around well bores. Indirect measurements for fractures are required, because a good depiction of the density and the orientation of fractures can help select optimal drilling locations. In sedimentary rocks, aligned and fluid-saturated open fractures are one of the main causes of seismic azimuthal anisotropy (Crampin and Leary, 1993).

Layered rock is the simplest anisotropic case with broad geophysical application. Layered rock has only one distinct direction, while the other two directions in Cartesian coordinates are equivalent to each other. Layered rock is referred to as transverse isotropic medium. When the axis of symmetry is vertical, it is called a Vertically Transverse Isotropic (VTI) medium. If the axis of symmetry is horizontal, it is called a Horizontally Transverse Isotropic (HTI) medium. When the axis of symmetry is neither vertical nor horizontal, it is called Tilted Transverse Isotropic (TTI) medium. Rocks with vertical open fractures can be considered as HTI media, or Azimuthally Anisotropic (AA) media. When seismic waves travel through or reflect from the fractured zone, the fractured rocks will affect the amplitude and travel time of the waves. It provides an opportunity to extract the fracture information from seismic waves by measuring the amplitude and/or velocity anisotropy.

Aligned vertical fractures cause azimuthal anisotropy of seismic shear waves (S waves) as well as compressional waves (P waves). Crampin et al. (1980) first reported the observation of shear wave splitting caused by aligned fractures from earthquake data. Alford (1986), and Lynn and Thomsen (1990) analyzed shear wave reflection data for shear wave splitting from multicomponent seismic surveys. They estimated the shear wave anisotropy from the time delays of the slow shear wave, and the fracture orientation from the direction of the fast shear wave. Many people have now studied shear wave splitting for fracture analysis (e.g. Lefeuvre et al., 1992; Mueller, 1992; Chaimov et al., 1995; Thomsen et al., 1995) from shear reflection data. Shear wave splitting analysis has also been applied to PS converted wave data (Gaiser, 2000; Olofsson et al., 2003; Van

Dok et al., 2003). Nebrija et al. (2004) used transmitted shear wave from offset Vertical Seismic Profile (VSP) data to estimate fracture parameters.

Seismic PP reflection data can be used for fracture analysis as well. Crampin et al. (1980) extracted fracture information from P wave velocity anisotropy. Thomsen (1988) discussed the normal moveout (NMO) velocity at the directions parallel and perpendicular to the strike of the fractures. Tsvankin (1997) gave an equation of the NMO velocity in an arbitrary direction. Lefeuvre et al (1992) first utilized amplitude variation with azimuth from PP reflection data to detect fractures. Rüger (1998) analyzed the amplitude variation with azimuth for reflected waves in theory. These methods will be reviewed in Chapter 2. There are many publications about the applications of the fracture analysis from PP reflection data (e.g. Garotta, 1989; Xu and Lu 1991; Lynn et al., 1996; Teng and Mavko, 1996; Craft et al., 1997; Li, 1999; Gray and Head, 2000; MacBeth and Lynn, 2001; Zheng and Gray, 2002; Gray et al., 2002, 2003; Chapman and Liu, 2004; Chi et al., 2004; Johansen et al., 2004; Parney, 2004; Zheng et al., 2004). These works are all based on the assumption of a single fracture system, i.e. fractures are aligned in a dominant direction. When multi-fractures with different orientation exist, the seismic amplitude response will be more complicated. Chen et al. (2005) presented a comparison of single and multi fractures on synthetic data. When the fracture density is kept the same, the multi-fracture system produces less amplitude variation with azimuth than the single fracture system.

Since seismic PP reflection surveys are widely available and cost efficient, it is useful to explore methods for fracture analysis using PP data. In practice, there are three methods of fracture analysis techniques using PP reflection data. They are (1) the NMO velocity method, (2) the residual moveout method, and (3) the amplitude method. Methods 1 and 2 use the travel time information of the seismic data, whereas method 3 uses amplitudes of the seismic data.

1) The NMO velocity method measures azimuthal NMO velocity variation of the reflection from the bottom of the fractured zone (Thomsen, 1988; Xu and Lu, 1991; Tsvankin, 1997). It is assumed that the direction of the fast NMO velocity is parallel to the direction of the fracture strike. The difference of the fast and slow NMO velocities can be an indicator of the fracture density.

2) The residual moveout method measures residual moveout of the reflection from the bottom of the fractured zone after applying NMO correction to the seismic gathers with isotropic velocities (Li, 1999). It is similar to the NMO velocity method, but more practical. The residual moveout versus azimuth are in a sinusoidal pattern. The direction with the most negative moveout (correspondent to the minimum travel time) is assumed to be the direction of the fracture strike. The magnitude of the moveout variation can also be an indicator of the fracture density.

3) The amplitude method measures amplitude variation with azimuth of the reflected waves from either the top or bottom boundary of the fractured zone (Lynn et al., 1996; Rüger, 1998; Gray and Head, 2000). It is assumed that the direction of the minimum AVO gradient is the direction of the fracture strike and the magnitude of the AVO gradient variation can be another indicator of the fracture density. This method produces fracture reflectivity for each CMP location and time sample.

The methods utilize different information carried in the seismic data and have their own advantages and disadvantages. The NMO velocity method and residual moveout method are sensitive to the whole block of the fractured zone. Thus, these two methods can only detect fractures from the reflection off the bottom boundary of the fractured zone. The amplitude method is sensitive to the contrast of the fracture (the difference of fracture density across a seismic interface). Therefore, it can, in principle, detect fractures from either the top or bottom boundary of the fractured zone. From the

processing point of view, the NMO velocity method and residual moveout method might be more stable than the amplitude method, because the amplitude of the seismic reflections may be altered during acquisition and processing, while travel time is relatively reliable. However, if the amplitudes of the seismic data are well preserved or recovered, the amplitude method gives higher resolution both temporally and spatially than the NMO velocity and residual moveout methods. To avoid the shortcomings of each method and to stabilize the results, the best way is to integrate all three methods so that more confident results can be achieved, compared to using only one method.

The assumption of determining fracture orientation for the three methods is questionable. There is an ambiguity on the estimated fracture orientation, which will be discussed in detail in Chapter 3. To solve the ambiguity, additional information is needed.

1.2 The objectives of this dissertation

The objectives of this dissertation are to provide a comprehensive review of existing methods of subsurface fracture analysis from PP seismic data, to point out the shortcomings of the methods, to present means to overcome these shortcomings, to present a new method to extract Thomsen's anisotropic parameter $\delta^{(v)*}$, and to present a practical workflow for fracture analysis. They are accomplished by:

- Reviewing the three methods on fracture analysis using seismic PP reflection data and discuss the advantages and disadvantages of those methods.
- Investigating the factors that will affect the precision and accuracy of fracture analysis.
- Discussing ambiguity of the estimated fracture orientation.
- Incorporating prestack time migration into fracture analysis so that fracture analysis can be used in structural areas.

- Extracting Thomsen's parameter, $\delta^{(v)}$, from seismic data.
- Presenting a practical workflow for fracture analysis.
- Applying this workflow on a physical modeling dataset and a field dataset.

This dissertation is focused on using PP reflection data for fracture analysis. The fractures are assumed to be vertical and open, saturated with fluid, and aligned in a dominant direction. Closed or cemented fractures are beyond the scope of this dissertation and will not be discussed.

1.3 The structure of this dissertation

Chapter 1 gives a brief introduction to fractures and methods of fracture analysis using PP seismic data, outlines the objectives of the dissertation, and also highlights the contributions of the author.

Chapter 2 reviews the anisotropy theory for both Vertical Transverse Isotropic (VTI) and Horizontally Transverse Isotropic (HTI) media. The approximations for azimuthal NMO velocity and amplitude variation with offset and azimuth for HTI media are also reviewed. Numerical modeling is conducted to verify the amplitude variation. The three methods used by industry for fracture analysis from seismic PP reflection data are reviewed and discussed. These methods are (1) NMO velocity method, (2) residual moveout method, and (3) amplitude method.

Chapter 3 is the main part of the author's work. It discusses the factors that affect the precision and accuracy of fracture analysis, and introduces common-angle time migration for fracture analysis by correctly positioning reflectors and improving amplitude preservation. The ambiguity of the estimated fracture orientation is discussed in this chapter as well. This ambiguity problem is shared by all three methods, and

---

[*] $\delta^{(v)}$ is a Thomsen's anisotropic parameter for Horizontally Transverse Isotropic (HTI) media.

therefore additional information besides PP seismic data is needed to solve the ambiguity. An example solution is given using FMI* log.

A new method, named δ inversion, is also developed in Chapter 3. This method estimates Thomsen's parameter, $\delta^{(v)}$, from the residual moveout of the reflection on the bottom of the fractured layer. The δ inversion combines the NMO velocity method and residual moveout method.

Based on the discussion and the remedy methods developed in Chapter 3, a practical workflow for seismic data in structural areas is given. This workflow combines the amplitude method and δ inversion in order to obtain stable and reliable fracture information.

Chapter 4 describes the application of the workflow presented in Chapter 3 on a physical modeling dataset recorded on a fractured model. Both the amplitude method and δ inversion were able to map fracture correctly and the results from both methods are similar.

Chapter 5 describes the application of the workflow on a real dataset in the Pinedale field, Wyoming, USA. The distributions of the fractures detected by the amplitude method and δ inversion are similar. They both outline the major fracture features in the area. A correlation map is created from the fracture reflectivity map and $\delta^{(v)}$ map. The correlation map agrees with the gas production rates.

Chapter 6 states conclusions and future direction in this research area.

---

* FMI (**F**ormation **M**icro**I**mager) provides microresistivity images in water-base mud. It can give in situ images of fractures. The vertical and azimuthal resolution of FMI is about 5 mm.

1.4 The contributions of the author in this dissertation

Most of the contributions of the author can be found in Chapter 3, which discusses the practical methods to detect fractures in structural areas, and factors that will affect the precision and accuracy of the results of fracture analysis. The contributions of the author are outlined below:

- Analyzed quantitatively the impact of a dip layer that introduces "false" amplitude anisotropy.
- Discussed and demonstrated the benefit of using common-angle time migration for fracture analysis.
- Developed a new method for extracting Thomsen's anisotropic parameter, $\delta^{(v)}$, from the residual moveout of the reflection from the bottom of fractured layers.
- Discovered and analyzed the ambiguity of the estimated fracture orientation by the three methods, and presented a practical solution to solve the problem.
- Presented a practical workflow for fracture analysis in structural areas. The workflow uses both the amplitude method and the δ inversion.
- Applied the workflow to a physical modeling dataset and a field dataset.

For the dissertation, the author developed some tools on different platforms, in Matlab, and in C for a Unix system.

- Wrote code for a Unix system for common-angle prestack time migration.
- Developed software for a Unix system for δ inversion, which is a combination of the NMO velocity and the residual moveout methods.
- Wrote code in Matlab for the comparison of the amplitude variations from a dipping reflector above an isotropic medium and a flat reflector above an anisotropic medium.

Chapter Two: Seismic wave reflectivity in anisotropic media and the methods for fracture analysis

2.1 Introduction

There are many fractured hydrocarbon reservoirs in the world. The fractures not only provide storage space to hold oil and gas in reservoirs, but also increase the permeability of reservoirs, or provide pathways for oil and gas flowing to well bores to be produced. On the other hand, cemented or mineralized fractures are barriers of oil and gas flow. Depiction of open fracture density and orientation is an important aspect of seismic reservoir characterization. It is important for geologists, geophysicists and reservoir engineers to have detailed maps of fracture density and orientation when they are making development plans for fractured reservoirs. Based on the fracture information, they can optimize their development plans accordingly. They can choose optimal locations for production and injection wells to maximize the economic values of the reservoirs.

Direct measurements of fractures in subsurface rocks are available from well logs and core samples. However, they only provide information around boreholes and information can only be collected after drilling. Seismic data contain information from underground structures as well as the rock properties of the reservoirs in a larger area. Saturated with fluid, vertically fractured reservoirs can be considered as Horizontally Transverse Isotropic (HTI) or Azimuthally Anisotropic (AA) media. When seismic waves travel through or are reflected from the boundaries of the fractured reservoirs, the fractures will leave “fingerprints” in the seismic data, although the fracture information is sometimes weak and difficult to be extracted from the seismic data.

When considering the wavelength of seismic data, the Earth can be considered as a smoothly varying homogeneous medium except at geological interfaces. The deformation of the medium caused by seismic waves is generally very small, unless in the area near the seismic sources, where it is usually not of interest. In the case of small

deformation, linear elastic theory can be used to study seismic wave propagation. Stress is a linear function of strain, and vice versa (Bullen and Bolt, 1985). Both stress and strain have nine components, but only six components are independent because of the symmetry. A stiffness matrix with 36 elastic constants links stress and strain together. However, there are only 21 independent constants for general anisotropic media. For the simplest case, isotropic media, the independent constants are reduced to only two, the Lamé parameters, λ and μ (See Appendix A for details). P wave velocity, V_p and S wave velocity, V_s can be expressed using these parameters as

$$V_p = \sqrt{\frac{\lambda + 2\mu}{\rho}}, \tag{2.1a}$$

$$V_s = \sqrt{\frac{\mu}{\rho}}, \tag{2.1b}$$

where ρ is the bulk density of the medium.

2.2 Anisotropy and Thomson's parameters

The velocity of seismic waves is dependent on the elastic moduli and bulk density of the medium. In most cases, crustal rocks are treated as isotropic materials, whose elastic moduli are the same in different directions. In reality, most crustal rocks are anisotropic materials, whose elastic moduli are different in different directions. Furthermore, sedimentary rocks are layered. Even if each individual layer is isotropic, the entire layered rock sequence may be anisotropic, when the thickness of the layer is less than the wavelength of the seismic waves (Backus, 1962; Helbig, 1984; Thomsen, 1986). Layered rock is the simplest anisotropic case with broad geophysical application. It has only one distinct direction (axis of symmetry), while the other two directions in Cartesian coordinates are equivalent to each other. Therefore, it is called a transverse isotropic medium. When the distinct direction is vertical, it is called a Vertically Transverse Isotropic (VTI) medium. If the distinct direction is horizontal, it is called a Horizontally

Transverse Isotropic (HTI) medium. When the distinct direction is neither vertical nor horizontal, it is called a Tilted Transverse Isotropic (TTI) medium. To describe this simplest case of anisotropy, only five elastic moduli are needed, two Lamé parameters, λ and μ, and three Thomsen's parameters, ε, δ and γ (Thomsen, 1986) (See Appendix A for details).

Sedimentary rocks are usually horizontally layered, so they are generally VTI media. The vertical direction is the axis of symmetry in this case. Vertical seismic waves travel with a different velocity than horizontal seismic waves. In general, when traveling in VTI medium, the velocity of a seismic wave is dependent on the angle between the vertical axis and the seismic raypath (i.e. take-off angle), the Lamé parameters, λ and μ, and the Thomsen's anisotropy parameters. The seismic phase velocities for different modes of waves for weak anisotropy can be expressed as (Thomsen, 1986)

$$V_p(\theta) = V_{p0}(1 + \delta \sin^2\theta \cos^2\theta + \varepsilon \sin^4\theta), \tag{2.2a}$$

$$V_{sv}(\theta) = V_{s0}(1 + \frac{V_{p0}^2}{V_{s0}^2}(\varepsilon - \delta)\sin^2\theta \cos^2\theta), \tag{2.2b}$$

$$V_{sh}(\theta) = V_{s0}(1 + \gamma \sin^2\theta), \tag{2.2c}$$

where, V_p, V_{sv} and V_{sh} are phase velocities for P, SV and SH waves, respectively. In addition, V_{p0} and V_{s0} are P and S wave velocities along the vertical axis (distinct direction normal to the thin layers). The Thomsen's parameters are ε, δ and γ, and θ is the angle between vertical axis and the normal to the wavefront. When θ is 0^o, the wavefront is propagating downward. When θ is 90^o, the wave travels horizontally.

As in Figure 2.1, the phase angle is defined as the angle between the wavefront normal and the vertical axis, while the group angle is the angle between the raypath and the vertical axis. Similarly, the phase velocity is the wave propagating velocity in the direction of the wavefront normal, and the group velocity is the wave propagating

velocity in ray direction. In isotropic media, the seismic wavefront normal is the same as the seismic raypath.

From equation (2.2), Thomsen (1988) derived the P wave NMO velocity for small offsets (short spread) for VTI media:

$$V_{nmo} \cong V_{p0}\sqrt{1+2\delta}\,. \qquad (2.3)$$

Depending on the sign of δ, the NMO velocity might be greater or less than the vertical P wave velocity. For some rocks, δ is negative, but generally the misalignment of mineral particles makes δ positive (Sayers, 2004).

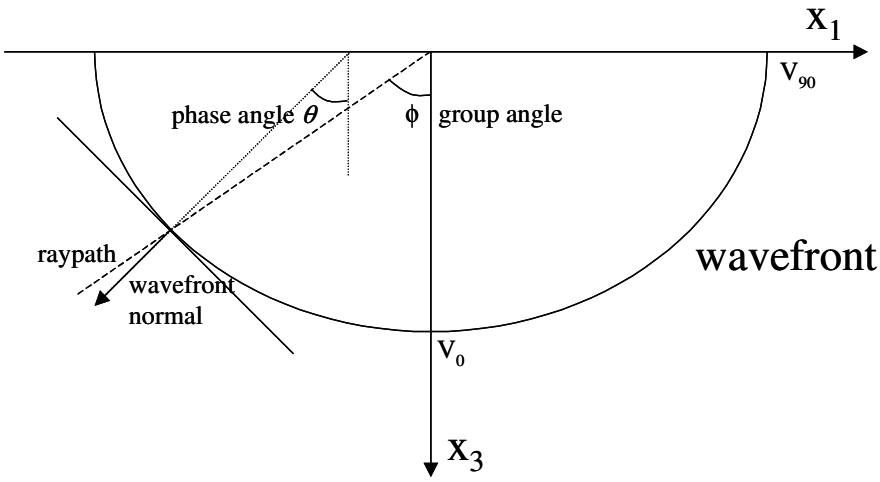

Figure 2.1. The definitions of phase (wavefront) angle and group (ray) angle (after Thomsen, 1986).

Rocks with vertically open fractures can be considered as a stack of vertical plates, or a HTI medium. The HTI medium is a VTI medium rotated 90^{o} about a horizontal axis. HTI is also called azimuthal anisotropic (AA) medium, since the velocity of seismic waves varies with the azimuthal direction of the wave propagation. By modifying his parameters to fit the geometry of HTI media, Thomsen (1988) presented

the equations for the NMO velocity for different modes of seismic waves in the direction perpendicular to the direction of fracture strike. Tsvankin (1997) derived the P wave NMO velocity at an arbitrary azimuth for an HTI medium:

$$V_{nmo}^2 = V_0^2(1 + 2\delta^{(v)}\cos^2(\varphi - \varphi_0)), \qquad (2.4)$$

where V_{nmo} is the P wave NMO velocity for small offsets, V_0 is the P wave velocity when seismic wave traveling vertically downward, φ_0 is the azimuth direction normal to the fractures, φ is the azimuth direction of the seismic ray path (Figure 2.2). $\delta^{(v)}$ is a Thomsen's parameter for HTI media, equivalent to δ in VTI media.

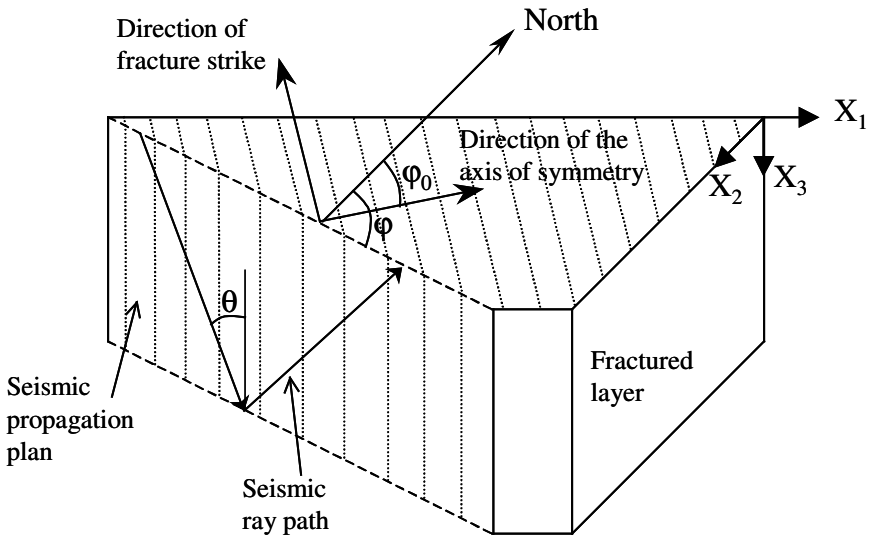

Figure 2.2. Definition of azimuth angles and incident angle. φ_0: azimuth angle of the axis of symmetry of fractured zone; φ: azimuth angle of seismic ray path; θ: incident angle of seismic wave.

2.3 Reflection coefficients of PP waves on boundaries of azimuthal anisotropic media

Since the elastic properties (or seismic velocities) of HTI medium are different at different azimuths, the reflection coefficients for a PP wave incident on a boundary of an HTI medium will be different at different azimuths. This difference will show on full-azimuth surface seismic recordings. By examining amplitudes of a reflected wave at different azimuths, one may extract the orientation and the fracture intensity of fractured reservoirs. Rüger (1998, 2002) derived an approximate equation of PP reflection coefficient at an arbitrary azimuth for an HTI medium over another HTI medium with the axis of symmetry in the same direction (the direction normal to the fracture strike). In special cases, one of the two layers can be isotropic, where all of the Thomsen's anisotropic parameters are zero.

For an interface between two isotropic layers, Shuey (1985) showed that the reflection coefficient of a PP reflection at an individual angle θ can be approximated as (valid for weak contrast of velocity and bulk density)

$$R(\theta) = A + B\sin^2\theta + C\sin^2\theta\tan^2\theta, \qquad (2.5)$$

where, $A = \frac{1}{2}(\frac{\Delta V_p}{V_p} + \frac{\Delta\rho}{\rho})$, $B = \frac{1}{2}\frac{\Delta V_p}{V_p} - 2(\frac{V_s}{V_p})^2\frac{\Delta\rho}{\rho} - 4(\frac{V_s}{V_p})^2\frac{\Delta V_s}{V_s}$, $C = \frac{1}{2}\frac{\Delta V_p}{V_p}$, V_p is the average P wave velocity of the top and bottom layers, V_s is the average S wave velocity of the top and bottom layers, and ρ is the average density of the rock of the two layers. Δ denotes the difference of the elastic property between the two layers. For example, $V_p = \frac{V_{p1} + V_{p2}}{2}$ and $\Delta V_p = V_{p2} - V_{p1}$, where V_{p1} is the P velocity in the top layer and V_{p2} is the P velocity in the bottom layer.

When an incident angle is less than 30°, the third term ($\sin^2\theta\tan^2\theta$) is small compared to the second term ($\sin^2\theta$). Therefore, the third term *C* is negligible for useful offset ranges, and equation 2.5 becomes

$$R(\theta) = A + B\sin^2\theta. \qquad (2.6)$$

Coefficient *A* is often called the AVO intercept, which is the P wave reflectivity ($R_p = \frac{1}{2}(\frac{\Delta V_p}{V_p} + \frac{\Delta\rho}{\rho})$). *B* is called AVO gradient. As a special case, when V_P/V_S = 2, $B = R_p - 2R_s$, where $R_s = \frac{1}{2}(\frac{\Delta V_s}{V_s} + \frac{\Delta\rho}{\rho})$, which is the S wave reflectivity.

When the media are HTI, Rüger (1998, 2002) shows that equation (2.6) can be modified to accommodate the azimuthal variation of the reflection coefficients. Then, the AVO gradient, *B*, of the equation (2.6), is composed of the azimuthal invariable part B^{iso} and the anisotropic contribution B^{ani} multiplied with the squared cosine of the azimuthal angle between the seismic ray path and the normal direction of fracture strike (refer to Figure 2.2 for angle definition),

$$B = B^{iso} + B^{ani}\cos^2(\varphi - \varphi_0), \qquad (2.7)$$

where,

$$B^{iso} = \frac{1}{2}\frac{\Delta V_p}{V_p} - 2(\frac{V_s}{V_p})^2\frac{\Delta\rho}{\rho} - 4(\frac{V_s}{V_p})^2\frac{\Delta V_s}{V_s},$$

$$B^{ani} = \frac{1}{2}[\Delta\delta^{(v)} + 2(\frac{2V_s}{V_p})^2\Delta\gamma^{(v)}].$$

$\delta^{(v)}$ and $\gamma^{(v)}$ are the Thomsen's parameters for HTI medium. $\Delta\delta^{(v)}$ is the difference of $\delta^{(v)}$ between top and bottom layers, and $\Delta\gamma^{(v)}$ is the difference of $\gamma^{(v)}$ between top and bottom layers. V_p and V_s are P and S wave velocities in vertical direction (or parallel to the fracture strike direction).

By defining $D = \frac{1}{2}[\Delta\delta^{(v)} + 2(\frac{2V_s}{V_p})^2 \Delta\gamma^{(v)}]$ as fracture reflectivity and combining equations (2.6) and (2.7), Rüger's equation for small incident angles (<30^o) can be rewritten as

$$R(\varphi,\theta) = A + [B + D\cos^2(\varphi - \varphi_0)]\sin^2\theta\,, \qquad (2.8)$$

where, B=B^{iso} and D=B^{ani}.

When an incident angle is greater than 30^o, the third term ($\sin^2\theta\tan^2\theta$) in equation (2.5) becomes important, and the amplitude varies with azimuth in a more complicated pattern than what described by equation (2.8). In this case Rüger's (1998, 2002) equation (2.8) extents to

$$R(\varphi,\theta) = A + [B + D\cos^2(\varphi - \varphi_0)]\sin^2\theta + C\sin^2\theta\tan^2\theta \quad , \qquad (2.9)$$

where, $C = \frac{1}{2}\{\frac{\Delta V_p}{V_p} - \Delta\varepsilon^{(v)}\cos^4(\varphi - \varphi_0) + \Delta\delta^{(v)}\sin^2(\varphi - \varphi_0)\cos^2(\varphi - \varphi_0)\}$, $\varepsilon^{(v)}$ and $\delta^{(v)}$ are the Thomsen's parameter for HTI media. $\Delta\varepsilon^{(v)}$ is the difference of $\varepsilon^{(v)}$ between top and bottom layers, and $\Delta\,\delta^{(v)}$ is the difference of $\delta^{(v)}$ between top and bottom layers.

2.4 Numerical model test of azimuthal amplitude variation

To verify Rüger's equation, a synthetic modeling test was conducted to study the amplitude variation with azimuth using a raytracing modeling package, ATRAK, provided by the University of Leeds, UK. The model is composed of two layers (Figure 2.3). The top layer of the model is an isotropic layer with a P wave velocity of 3000 m/s, an S wave velocity of 1500 m/s and a bulk density of 2.2 g/cm^3. The simulated thickness of the top layer is 500 m. The bottom layer is an HTI layer with a P wave velocity of 3500 m/s, an S wave velocity of 2400 m/s in the fracture strike direction, a bulk density of 2.3 g/cm^3. The Thomsen's parameters for the bottom layer are: $\varepsilon^{(v)} = -0.15$, $\gamma^{(v)} = -0.1$, and $\delta^{(v)} = -0.35$. For this model, fracture reflectivity, D, is 0.031.

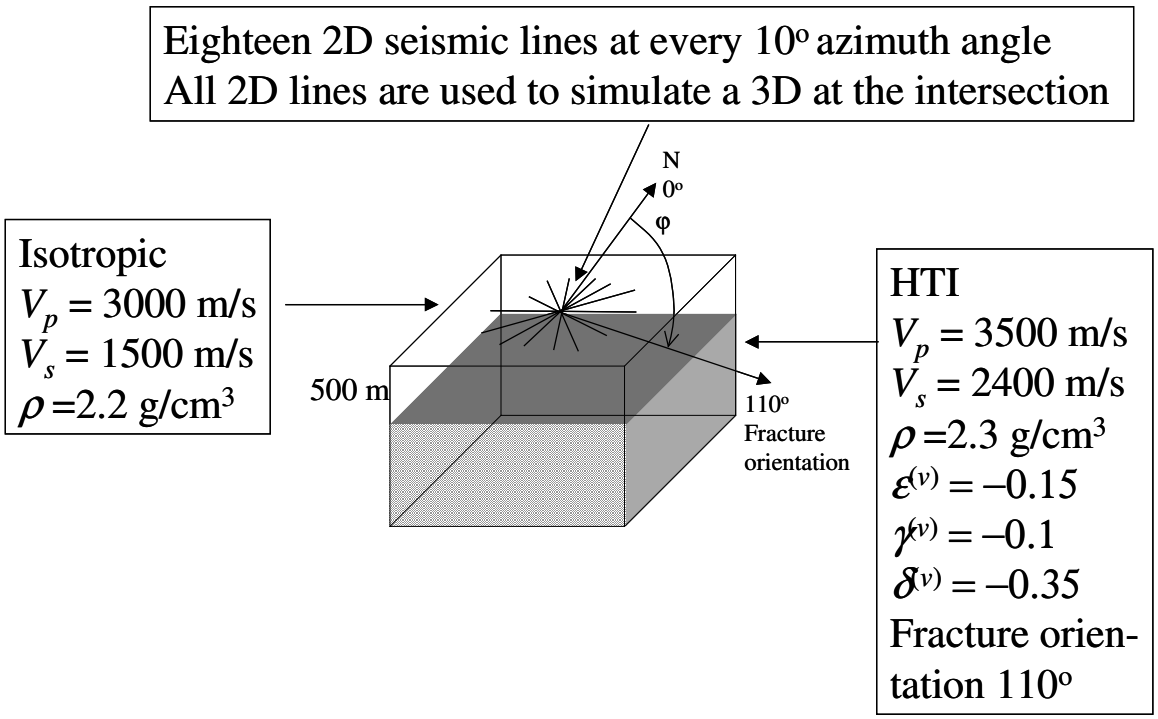

Figure 2.3. A simple model used for verifying Rüger's equation (equations 2.8 and 2.9). The top layer is isotropic and the bottom one is an HTI layer. Eighteen 2D lines were shot at different azimuth with an increment of 10°. The recordings of the eighteen 2D lines were used to simulate a 3D gather at the intersection of the 18 lines for investigating amplitude variation with offset and azimuth.

Eighteen 2D lines were shot at different azimuths with an increment of 10^o. All of the 2D lines were used to simulate a 3D gather at the intersection of the 18 lines and amplitude variation with offset and azimuth is examined on the 3D gather. The amplitudes of the reflected seismic wave from the interface between the two layers at different azimuths and offsets are shown on Figure 2.4. It is clear, at small source receiver offsets (< 500 m or 27^o), the period of the amplitude variation with azimuth is 180^o. Since the fracture reflectivity for this model is positive, the minimum AVO gradient (in the offset range of 0 – 500 m) is in the fracture strike direction (110^o). However, at large offsets (>500 m), the pattern of the amplitude variation with azimuth becomes more complex, which is a combination of 90^o and 180^o periods.

Figures 2.5 and 2.6 show amplitude variation with azimuth at two different offsets (300 and 900 m, respectively). There are two lines in the Figures 2.5 and 2.6. The solid line is the amplitude measured from the ATRAK synthetic data and the dashed line is the theoretical amplitude calculated from Rüger's (1998, 2002) equations (equations 2.8 and 2.9). His equation predicts the amplitude very well with minor errors, compared to the amplitude from ATRAK modeling data. At small offsets (< 500 m or 27^o), the amplitude changes with azimuth is dominated by term $\cos^2(\varphi-\varphi_0)$ and match the prediction of equation 2.8, since the amplitude variation curve (Figure 2.6) is sinusoidal with the period of 180^o.

However, at large offsets (>500 m), the curve of the amplitude variation with azimuth becomes more complicated and matches the prediction of equation 2.9, which is a sinusoid of the period of 180^o superposed by other sinusoids with the period of 90^o. The complicated curve is the combined contribution of $\cos^2(\varphi-\varphi_0)$, $\cos^4(\varphi-\varphi_0)$ and $\sin^2(\varphi-\varphi_0)\cos^2(\varphi-\varphi_0)$ at far offsets, because the third term, $\sin^2\theta\tan^2\theta$, in equation 2.9 is not negligible.

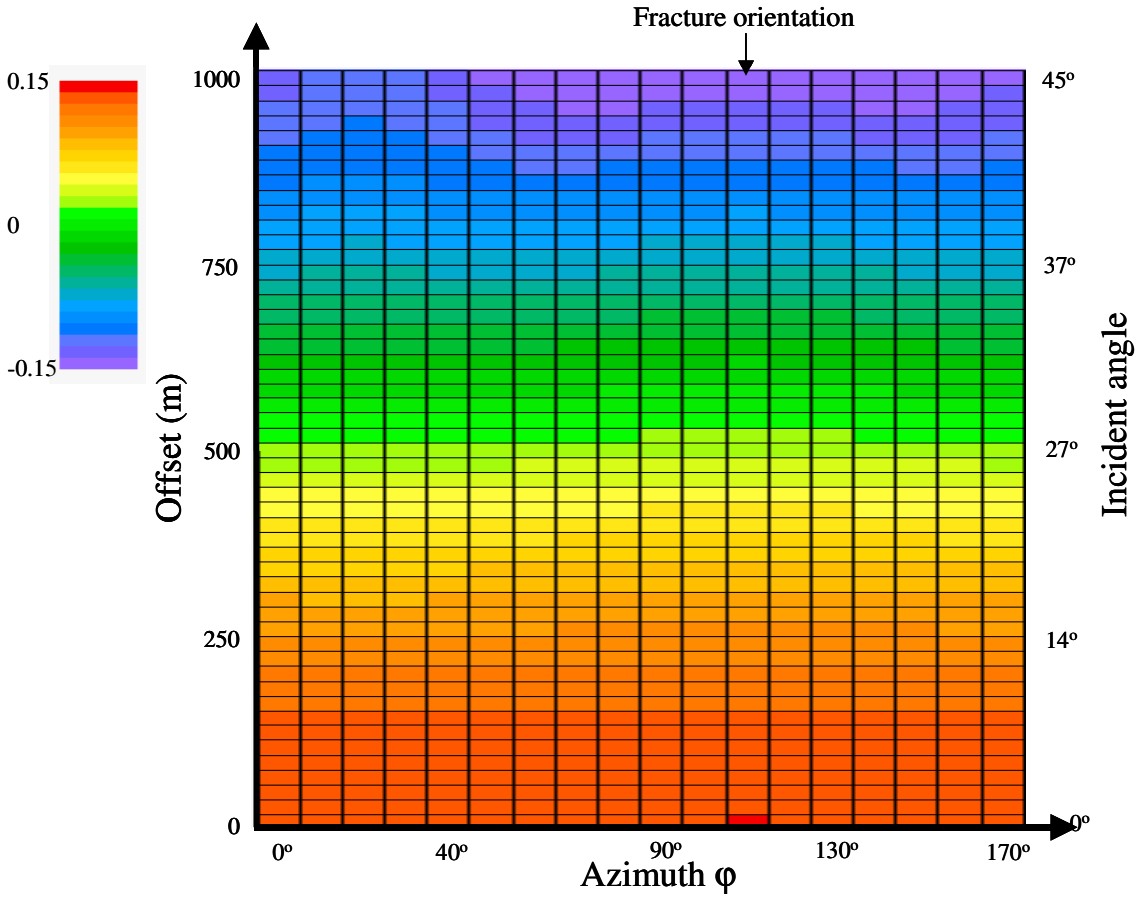

Figure 2.4. Amplitude variation with azimuth at different offset of reflected seismic wave from the interface or the top of the HTI layer in the model (Figure 2.3). At small offsets (< 500 m or 27°), the amplitude changes with azimuth is dominated by the term $\cos^2(\varphi-\varphi_0)$. However, at large offsets (>500 m), the pattern of the amplitude variation with azimuth becomes more complicated, which is the combination of $\cos^2(\varphi-\varphi_0)$, $\cos^4(\varphi-\varphi_0)$ and $\sin^2(\varphi-\varphi_0)\cos^2(\varphi-\varphi_0)$.

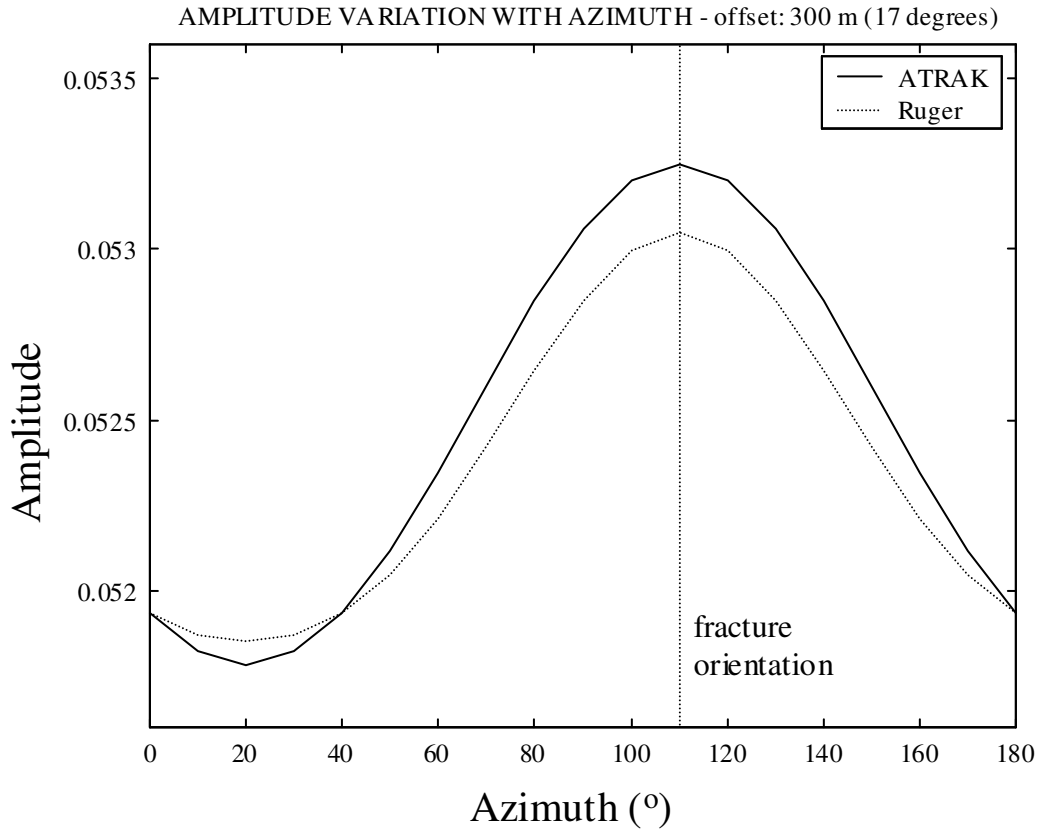

Figure 2.5. Reflection amplitude variation with azimuth at an offset of 300 m (17°). The solid line shows the amplitude of the synthetic data modeled by ATRAK. The dashed line is the amplitude calculated from equation 2.8. It is clear that the curve of amplitude variations with azimuth is a sinusoid with the period of 180°.

Conclusions can be drawn that for small incident angle of seismic waves, reflection amplitude varies with azimuth with a period of 180°. For small offset ranges, the AVO gradient reaches its extreme values in the directions parallel and perpendicular to the direction of fracture strike. When *D* is positive, the minimum AVO gradient is in the direction of fracture strike. When *D* is negative, the minimum AVO gradient is in the direction perpendicular to the direction of fracture strike. When a 3D seismic survey with a good azimuth and offset coverage is available, there is an opportunity to extend AVO analysis to invert fracture reflectivity and fractures orientation from seismic PP reflection data.

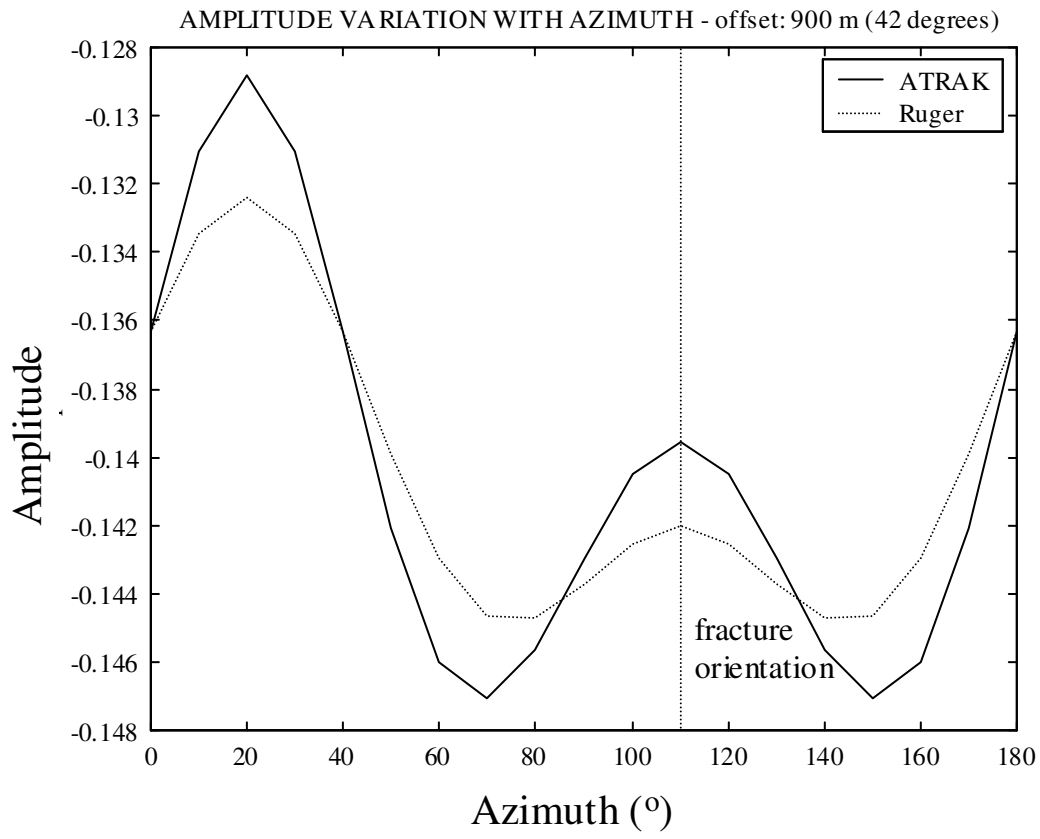

Figure 2.6. Reflection amplitude variation with azimuth at an offset of 900 m (42^o). The solid line shows the amplitude of the synthetic data modeled by ATRAK. The dashed line is the amplitude calculated from equation 2.9. It is clear that the curve of amplitude variations with azimuth is a sinusoid with the period of 180^o superposed by other sinusoids of the period of 90^o.

For seismic waves at large incident angles, the short period (90^o) component will appear, or even dominate the amplitude variation with azimuth, and make the pattern of the amplitude variation more complicated. If the large offset Rüger's equation (equation (2.8)) is used for fracture analysis, the result may be unstable, because the equation has too many variables. Therefore, for fracture analysis using Rüger's equation in practice, it is better to limit the maximum incident angle to 30^o.

2.5 Methods for fracture analysis from PP data

In the 1980's, geophysicists started to use pure shear (S) wave data to observe shear wave birefringence (shear wave splitting) when the S waves travel through fractured reservoirs (Alford, 1986; Lynn and Thomsen, 1992). The high cost of acquisition of pure S wave data and the requirement of special equipment prevent the method from being widely used in exploration. Since the early 1990's, it became popular to use PP reflection data to detect fractures (Xu and Lu, 1991; Lefeuvre et al, 1992; Lynn et al., 1996; Teng and Mavko, 1996; Craft et al., 1997; Li, 1999; Gray and Head, 2000), because improved technology of acquisition provides high quality PP data and improved processing technology yields high resolution and fidelity gathers, sections and seismic attributes.

Currently, there are three types of techniques for extracting fracture information from PP data in the industry. One method is to examine the azimuthal variation of NMO velocity (the NMO velocity method). Another is to examine the azimuthal variation of residual moveout (the residual moveout method). The third method is to examine the amplitude variation with azimuths (the amplitude method). While the first two methods utilize azimuthal velocity anisotropy, the third one utilizes the azimuthal amplitude anisotropy. Each of these methods has its advantages and disadvantages.

2.5.1 The NMO velocity method

Since vertically fractured reservoirs are azimuthal anisotropic media, velocities of both P and S waves are different when they travel at different azimuth angles to the fractures. The horizontal velocity is higher for seismic waves traveling parallel to the fractures than traveling perpendicular to the fractures. Note that the horizontal velocity is not the same as the normal moveout (NMO) velocity. With the short-spread limitation, for weak anisotropy, the P wave NMO velocity at an arbitrary azimuth is given by Tsvankin (1997):

$$V_{nmo}^2 = V_0^2(1 + 2\delta^{(v)}\cos^2\varphi), \qquad (2.10)$$

where V_0 is the velocity of the seismic wave traveling vertically; φ is the azimuthal angle between seismic ray path and the normal direction of fractures. $\delta^{(v)}$ is the Thomsen's anisotropic parameter (Thomsen, 1986, Tsvankin, 1997) for HTI medium.

Equation (2.10) shows that V_{nmo} changes with the angle between seismic ray path and the normal direction of fractures. It is an 180^o periodical function. When φ is 90^o, the seismic wave travels parallel to the fractures, the NMO velocity is the same as the vertical velocity. When φ is 0^o, the seismic wave travels perpendicular to the fractures, the NMO velocity reaches its maximum if $\delta^{(v)}$ is positive, or minimum otherwise.

Equation (2.10) may be used to fit the NMO velocities from different directions to find out φ and $\delta^{(v)}$, provided NMO velocities from velocity analysis have enough resolution and reliability.

The first order approximation of equation (2.10) is:

$$V_{nmo} = V_0(1 + \delta^{(v)}\cos^2\varphi). \qquad (2.11)$$

Xu and Lu (1991) undertook an experiment in which they built a physical model using a stack of vertical Plexiglass plates to simulate a vertically fractured medium. On the bottom of the model, a shallow hole was milled out to simulate a dome shaped anomaly. The modeling scale is 1:10,000. The simulated model is about 868 m thick, and the dome is about 127 m high with a radius of about 584 m (Figure 2.7).

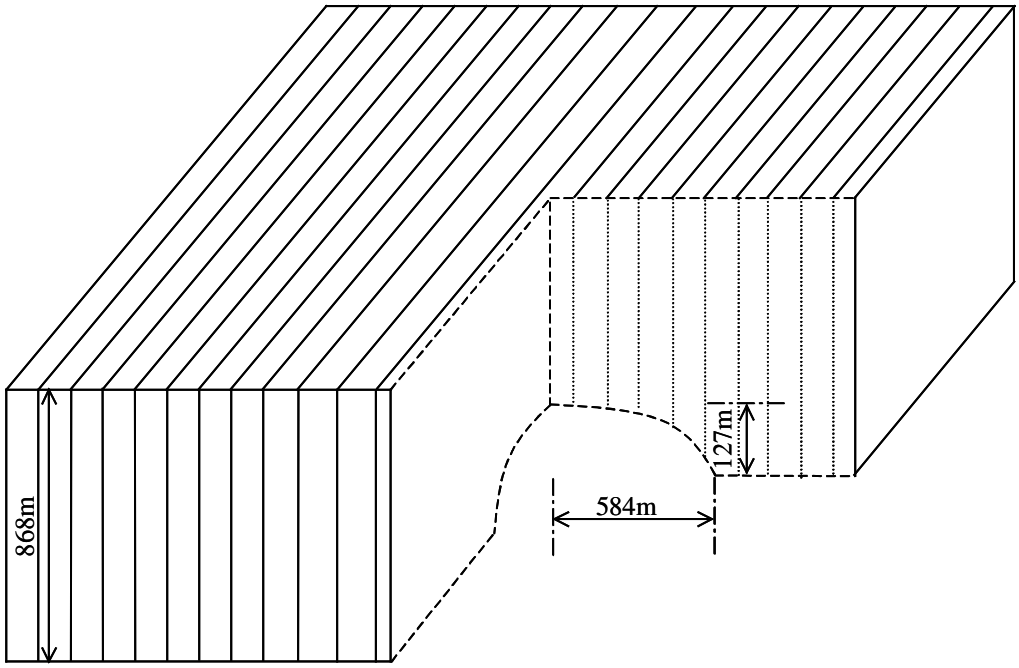

Figure 2.7. Schematic diagram of the model Xu and Lu (1991) used for fracture analysis.

The model was assembled in water and pressure was applied at the both ends in order to squeeze out the air between plates and get good contacts between plates. Two 2D lines were shot at orthogonal directions on the top surface of the model, one is parallel and another is perpendicular to the strike direction of the fractures. The travel time (measured from stacked sections) from the surface to the flanks of the dome on the perpendicular line is longer than that on the parallel line. From velocity analysis, the stacking velocity on the parallel line is 2950 m/s, and perpendicular line 2650 m/s. There is about 13% P wave anisotropy. This physical experiment indicates that fracture information may be extracted from PP wave by measuring NMO velocity variation at different azimuths.

2.5.2 The residual moveout method

Since velocity analysis may not give accurate azimuthal NMO velocities, it would be difficult in practice to determine the velocity anisotropy. Li (1999) presented an alternate way to detect fractures using PP data. After applying NMO correction using an isotropic velocity (average velocity of all azimuths), residual moveout will remain in the NMO corrected gathers. In one direction, the events may be flat, one direction under-corrected, and another direction overcorrected. Since it is relative easy to examine residual moveout, this method may have advantage over the NMO velocity method.

The residual moveout varies with azimuth (Li, 1999):

$$\Delta t = (t_{\perp} - t_{\parallel})\cos 2\varphi , \qquad (2.12)$$

where $t_{\perp}$ is the equivalent zero-offset travel time for the ray path perpendicular to the fractures, while $t_{\parallel}$ is the equivalent zero-offset travel time for the ray path parallel to the fractures, and φ is the azimuthal angle between ray path and the strike direction of fracture.

Equation (2.12) is also an 180^{o} periodic function and Δt has a similar shape to V_{nmo} in equation (2.11). Li (1999) gave synthetic tests for three different models in his paper. Only the third model, which has three layers, is shown here. The top and bottom layers are isotropic. There is an azimuthal anisotropic layer in the middle. The P and S wave velocities and the Thomsen's parameter ($\varepsilon^{(v)}$, $\delta^{(v)}$ and $\gamma^{(v)}$) of the model are given in Table 2.1. Since both P and S wave velocities are higher in the top layer than the anisotropic layer, the anisotropic layer is equivalent to Class IV sandstone (Rutherford and Williams, 1989; Castagna et al., 1998). There are four 2D lines with different angles from the strike direction of fracture (Figure 2.8). NMO corrected gathers are shown in Figure 2.9.

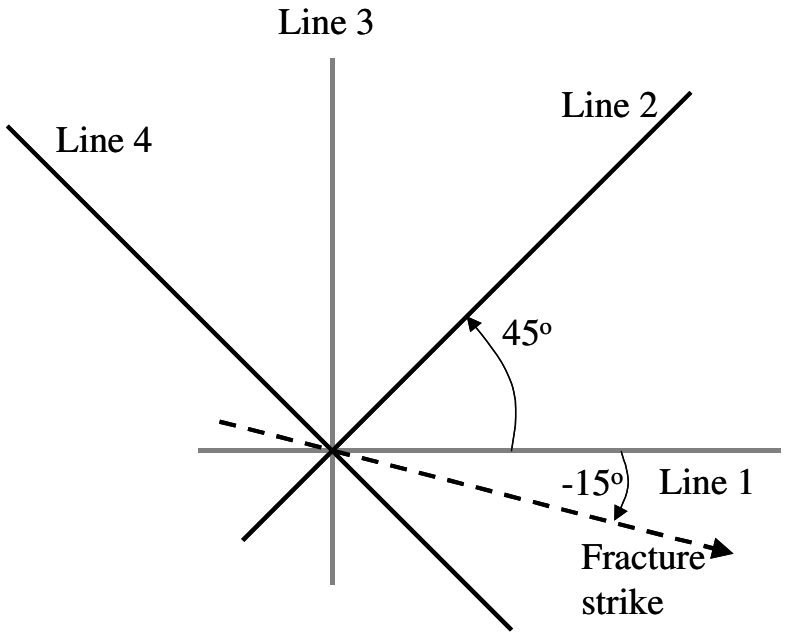

Figure 2.8 Four 2D lines with different angles from the fracture strike directions. Lines 1 and 3 are perpendicular to each other, so are Lines 2 and 4. (after Li, 1999)

From Figure 2.9, it can be seen that there are two events at around 1.0 and 1.25 s, respectively. The first one is from the top of the fractured layer. It is flat at all azimuths, since the medium above this interface is isotropic. The second one is from the bottom of the fractured layer. Azimuthal anisotropy can be seen on this event. The benchmark is the first panel at the most left-hand side. It is a gather recorded from a line (not shown in Figure 2.8) parallel to the fracture strike direction. Both events are flat, which means the NMO velocity is correct for seismic wave traveling along the fracture strike direction. Line 1 has the smallest residual moveout, since its direction is close to the fracture strike direction. While Line 3 has the largest positive residual moveout, since it is almost perpendicular to the fracture strike direction and the seismic wave needs longer time to travel from the top to the bottom of the fractured layer. Li (1999) picked the residual moveout from all four lines and calculated the fracture orientation, which is -15^{o} and matches the synthetic model very well.

Table 2.1 Parameters of the model used in the study (after Li, 1999)

model		density (g/cm^3)	V_p (m/s)	V_s (m/s)	$\varepsilon^{(v)}$	$\delta^{(v)}$	$\gamma^{(v)}$	thickness (m)
High/low	Layers 1, 3	2.3	3048	1574	0	0	0	1500
(shale/sand)	Layer 2	2.19	2183	1502	0.27	0.26	-0.16	300

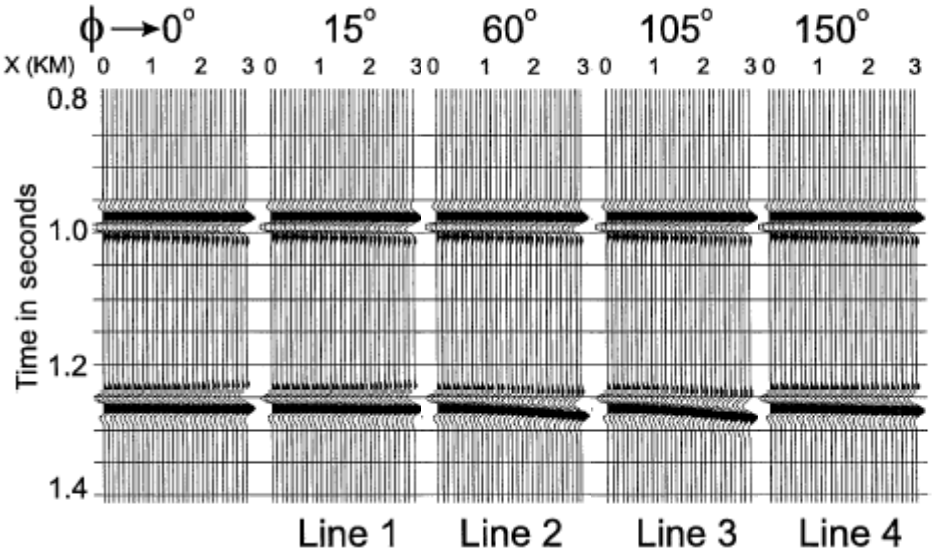

Figure 2.9 CMP gathers for different azimuths calculated for the shale/fractured gas sand model with a high/low impedance contrast. (modified from Li, 1999)

The same analysis was also applied to field data by Li (1999). Four 2D lines were shot in the North Sea (Figure 2.10). All lines nearly intersect each other at the same point. The target zone is fractured chalk where the top of the chalk is about 2000 m from the sea floor and has a thickness of approximately 200 m. NMO corrected gathers from the four lines are shown in Figure 2.11. The horizons of the top and bottom of the chalk are picked at the CMP gathers. The interval travel time from the two horizons varies from different offsets and lines. The longer the offset, the more interval time variation. Line 2 has the longest interval travel time at the same offset compared to other lines, which

indicates this line is close to the perpendicular direction of fracture. Interval travel times (called interval moveout by Li) are measured and used to calculate fracture orientation in order to remove the impact of statics. The analysis shows the fracture orientation is about –43^{o} from line 1, which matches the geological observation.

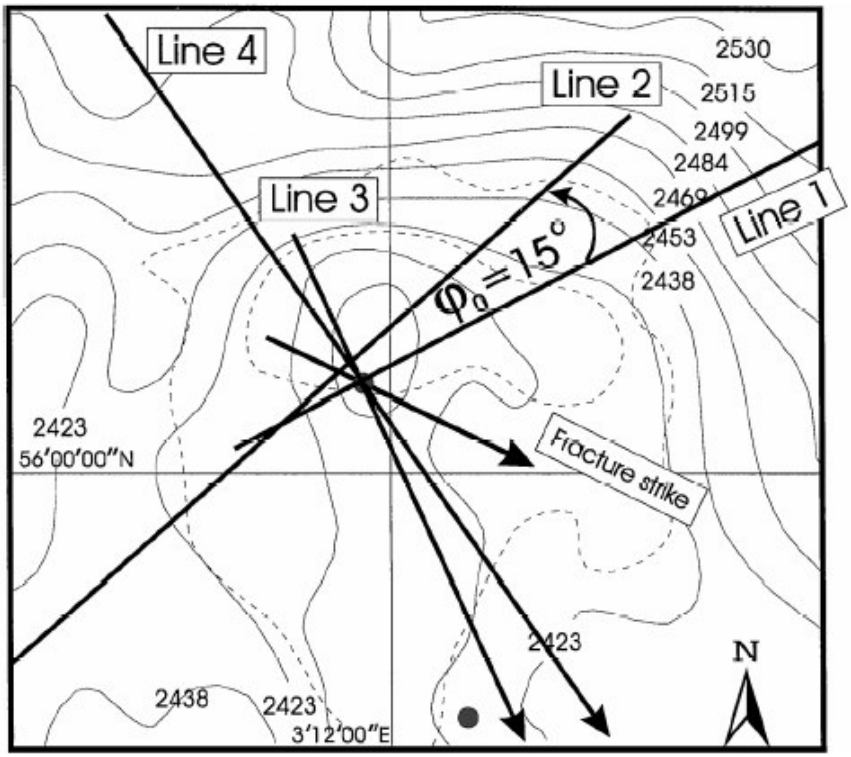

Figure 2.10 Field data example. Map of four seismic lines from the North Sea. Lines 1 and 3 intersect each other at CMPs 420 (line 1) and 440 (line 3), while lines 2 and 4 intersect at 730 (line 2) and 830 (line 4). (after Li, 1999)

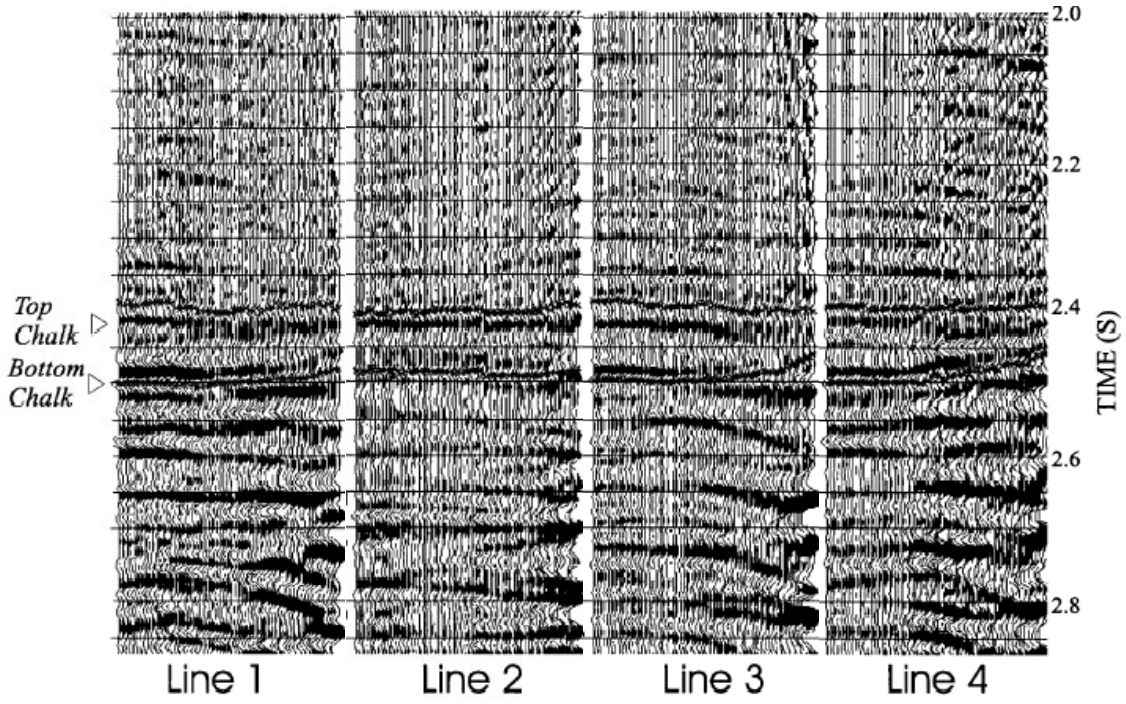

Figure 2.11. The NMO corrected CMP gathers at the intersecting points of the four lines shown in Figure 2.10 (modified from Li, 1999)

2.5.3 The amplitude method

Both velocity and moveout methods of P wave data can provide P wave anisotropy information, but no S wave information. S wave velocity will not be affected by the fluid content in reservoirs, but P waves will. Therefore, S waves can provide more information about reservoir rocks than P waves can, since they are dependent on elastic rock properties and not fluids. Using AVO inversion, S wave information can be extracted from PP reflection data, and it is in PP time.

The AVO gradient, which is largely influenced by S wave velocity, varies along azimuths, when the medium is azimuthally anisotropic. In the case of one isotropic layer overlying an azimuthal anisotropic layer, for a ray path perpendicular to the fractures, the AVO gradient gets its one extreme value (minimum or maximum). For ray path parallel

to the fractures, the AVO gradient reaches another extreme value. The sign of D of equation (2.8) determines at which azimuthal direction the maximum value of AVO gradient occurs. One might measure amplitude from all offsets and azimuths, then apply AVO inversion from the measurements using equation (2.8) to get the fracture reflectivity and orientation.

Some work has been done using azimuthal variation of AVO gradient to detect fracture orientation and reflectivity (e.g. Lynn and Thomsen, 1990; Lynn et al., 1996; Mallick et al., 1998; Gray and Head, 2000; MacBeth and Lynn, 2001; Gray et al., 2002; Hall and Kendall, 2003; Luo and Evans, 2004). Fracture reflectivity and orientation distribution were extracted from PP reflection data. The results matched geological and engineering data from the field and greatly helped drilling plans.

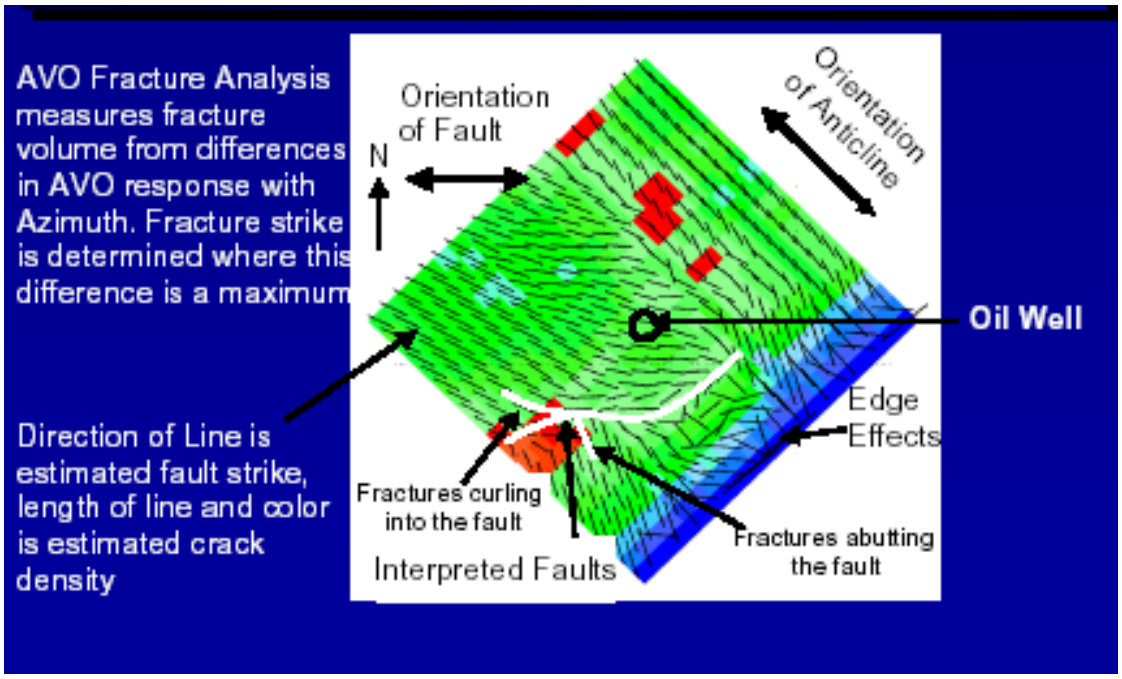

Figure 2.12 Fracture strike and fracture reflectivity estimated from the PP seismic data in a half-mile by half-mile area around well 43-33 in Manderson Field, WY, USA. (after Gray and Head, 2000).

A good example is given by Gray and Head (2000). Figure 2.12 shows the estimated fracture orientation and fracture reflectivity around Well 43-33 in Manderson Field, Wyoming, USA. There is a short line in each CMP bin. The direction of the lines shows the measured fracture orientation. While the length of the lines and the background colors show the measured fracture reflectivity. The result of the fracture analysis matches the findings on core samples.

2.6 Summary and discussion

Vertically fractured reservoirs can be considered as azimuthal anisotropic or HTI media. For such a kind of medium, P wave NMO velocity of the reflected wave from the bottom of the fractured reservoir varies with the azimuth of seismic raypaths, and amplitudes of the reflected waves from both top and bottom of the reservoir do vary with the azimuth. By measuring the variation of the velocity and/or amplitude, one is able to estimate the fracture reflectivity and the orientation of the fractured reservoirs. There are three techniques that are found in the geophysical literature. Each of the methods has its advantage and disadvantage.

The NMO velocity and residual moveout methods are less sensitive to signal-to-noise ratio of the seismic data, compared to the amplitude (AVO) method. In practice, picking residual moveout differences at different azimuths is easier than picking NMO velocity difference. Therefore the residual moveout method is more applicable to real data than the NMO velocity method. However, both of them can only detect the lower boundary of a fractured reservoir, provided that the fractured zone is thick enough to cause detectable travel time difference. In comparison, the amplitude method can detect both upper and lower boundaries of a fractured reservoir. When the thickness of fractured zones is small or the fractured zone is deep, the velocity difference caused by the fractured zone may not be detectable by the NMO velocity or residual moveout methods. The amplitude method may be the only choice in this case.

True amplitude or AVO compliant processing is required by the amplitude method, while it is not a must for the other two methods. When the amplitude method is used for fracture analysis, one should make sure that the amplitude information is preserved in the entire processing flow; otherwise, the result from fracture analysis will be incorrect.

All the three methods of fracture analysis from PP seismic data have an ambiguity of the estimated fracture orientation. The ambiguity in fracture orientation will be discussed in detail in Section 3.5.

Chapter Three: Challenges and practical solutions for fracture analysis

3.1 Introduction

There are many factors that can affect the accuracy of fracture analysis. If these factors are not handled properly, false fractures may be interpreted; the estimated fracture reflectivity, orientations and locations of fractures may not be correct. These factors are:

i. Dipping reflectors will introduce false azimuthal anisotropy, therefore the dip effect should be removed before fracture analysis;
ii. Fracture information extracted from the unmigrated CMP gathers in structural areas will be mispositioned, so migration should be applied to the seismic data prior to fracture analysis;
iii. Because widely used common-offset prestack migration may degrade the quality of fracture analysis, a better migration algorithm is required;
iv. The ambiguity of the estimated fracture orientation from seismic data needs to be solved. The ambiguity problem is shared by all three methods mentioned in Chapter 2.

In this chapter, these problems will be discussed in detail, and methods to address the problems will be presented in theory and tested by examples of synthetic and real data. This chapter will conclude with a practical workflow for processing.

As mentioned in Chapter 2, the three methods of fracture analysis use different information of seismic data. The NMO velocity method and residual moveout method use travel time, while the amplitude method uses amplitude. Each method has its advantage and disadvantage. It is better to use both travel time and amplitude information so that the result of fracture analysis will be more reliable than that of a single method.

In this chapter, the NMO velocity method and the residual moveout method will be integrated into a new method, named δ inversion. Then, both the δ inversion and the amplitude method will be applied to common-angle migrated gathers to crosscheck result.

3.2 Dip-induced "anisotropy"

A dipping reflector in isotropic media can introduce azimuthal variation of the amplitude of seismic reflection waves, similar to that caused by azimuthally anisotropic media. For a given offset, the incident angle for the seismic wave traveling in the strike direction of the dip reflector is larger than that traveling in the dip direction. Therefore the amplitudes of the reflected seismic waves in the two directions are different, because of the different incident angles.

Levin (1971) derived an equation of the stacking velocity for a reflection from a dipping reflector. To extend his work, an equation of the amplitude variation versus offset and azimuth for a reflection from a dipping reflector is derived and presented here. Figure 3.1(a) shows a dipping reflector in a volume (x, y, z) with the dip β and the Y-axis chosen to be parallel to the dip direction. The strike direction is parallel to the X-axis. A 2D seismic line is defined on the surface by the blue line *BE* with an azimuthal angle φ. All zero-offset raypaths will be normal to the dipping reflector with reflections points that lie on the line *CE*. All raypaths will lie on the plane defined by *BCE*.

As shown in Figure 3.1(b), *BC* is normal to the dipping reflector, *AC* normal to the ground surface and the angle *ACB* is equal to β, and the angle *ABD* is φ. In the right-angle triangle *ABC*, by defining the distance *BC* as 1.0, then

$$AC = \cos\beta, \tag{3.1a}$$

$$AB = \sin\beta. \tag{3.1.b}$$

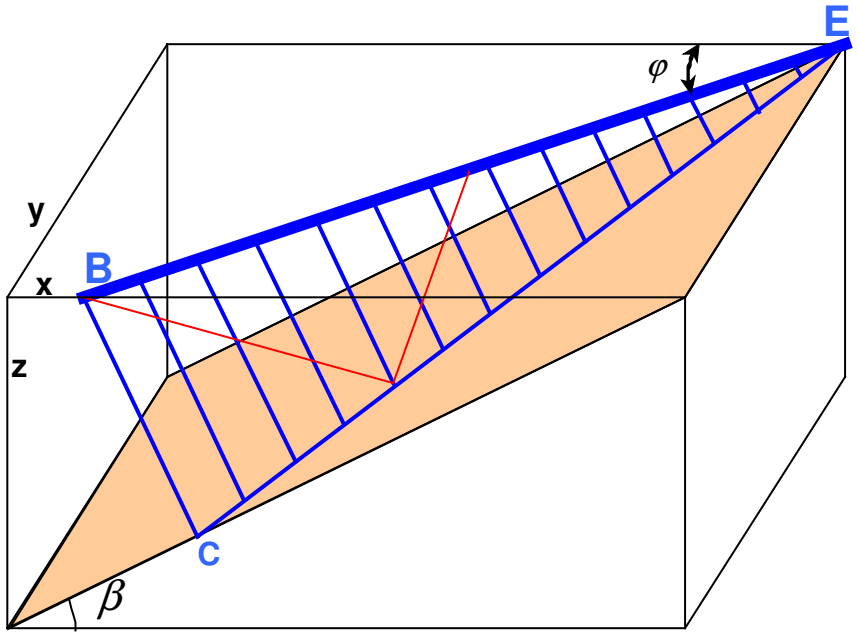

(a)

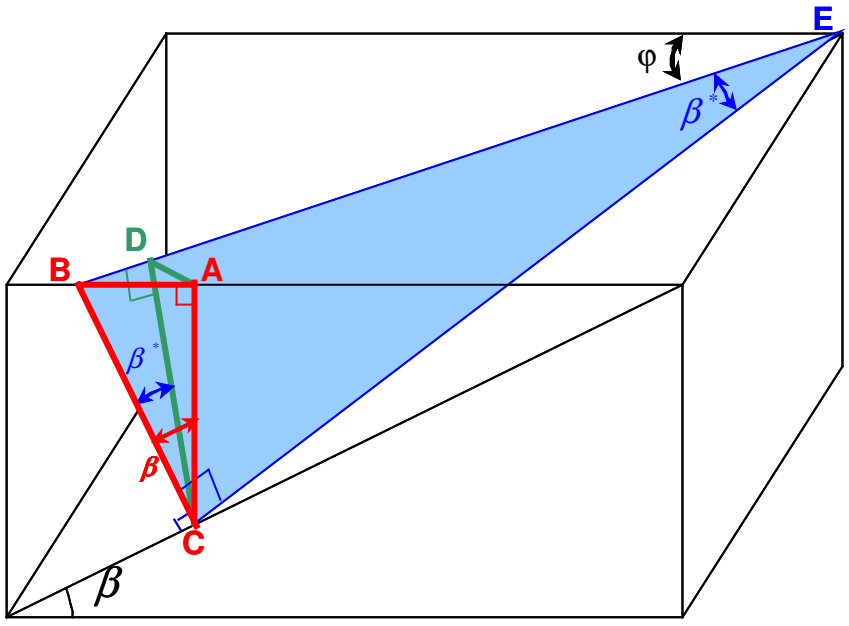

(b)

Figure 3.1. Geometry for defining the apparent dip for a 2D seismic line above a 3D dipping reflector (courtesy of J. Bancroft).

The line *AC* is projected onto the plane *BCE* to produce the line *DC* that is normal to the line 2D line on the surface *BE*. The length of *BD* is

$$BD = AB\cos\varphi = \sin\beta\cos\varphi . \tag{3.1c}$$

The triangles *BCD* and *BCE* are similar, therefore the angles *BEC* and *BED* are the same, called β^*, which is the apparent dip angle of the dipping reflector with respect to the 2D seismic line *BE*.

$$\sin\beta^* = \frac{BD}{BC} = \sin\beta\cos\varphi . \tag{3.1d}$$

Now the problem in 3D space is simplified to a problem in 2D plane (Figure 3.2). Assuming a source is at point *S*, and a receiver is at point *R*. The apparant dip angle of the reflector is β^*. S' is the mirror image of the source S with respect to the dip reflector. The angle between lines *SR* and *RN* is β^*. *M* is the midpoint between source *S* and receiver *R*, and MM_0 is normal to the reflector. Travel time for seismic waves from the source location, *S*, to the reflection point, *G*, and is bounced back to the receiver location, *R*, is equivalent to travel time from S' to *R*. From the geometry shown in Figure 3.2, it is not difficult to find out the relationships between these line segments are

$$SN = x\sin\beta^* \ , \tag{3.2a}$$

$$SS_0 = d + \frac{1}{2}SN \ , \tag{3.2b}$$

$$SS' = 2SS_0 = 2d + x\sin\beta^* \ , \tag{3.2c}$$

$$RN = x\cos\beta^* , \tag{3.2d}$$

$$NS' = SS' - SN = 2d \ , \tag{3.2e}$$

$$RS' = \sqrt{NS'^2 + RN^2} = \sqrt{4d^2 + x^2\cos^2\beta^*} \ , \tag{3.2f}$$

where d is the distance from the midpoint M to the reflector, MM_0; x is the source-receiver offset, SR. According to the cosine law, the incident angle, θ, can be written as

$$\cos\theta = \frac{SS'^2 + RS'^2 - x^2}{2 \cdot SS' \cdot RS'} = \frac{2d}{\sqrt{4d^2 + x^2 \cos^2 \beta^*}}. \qquad (3.3)$$

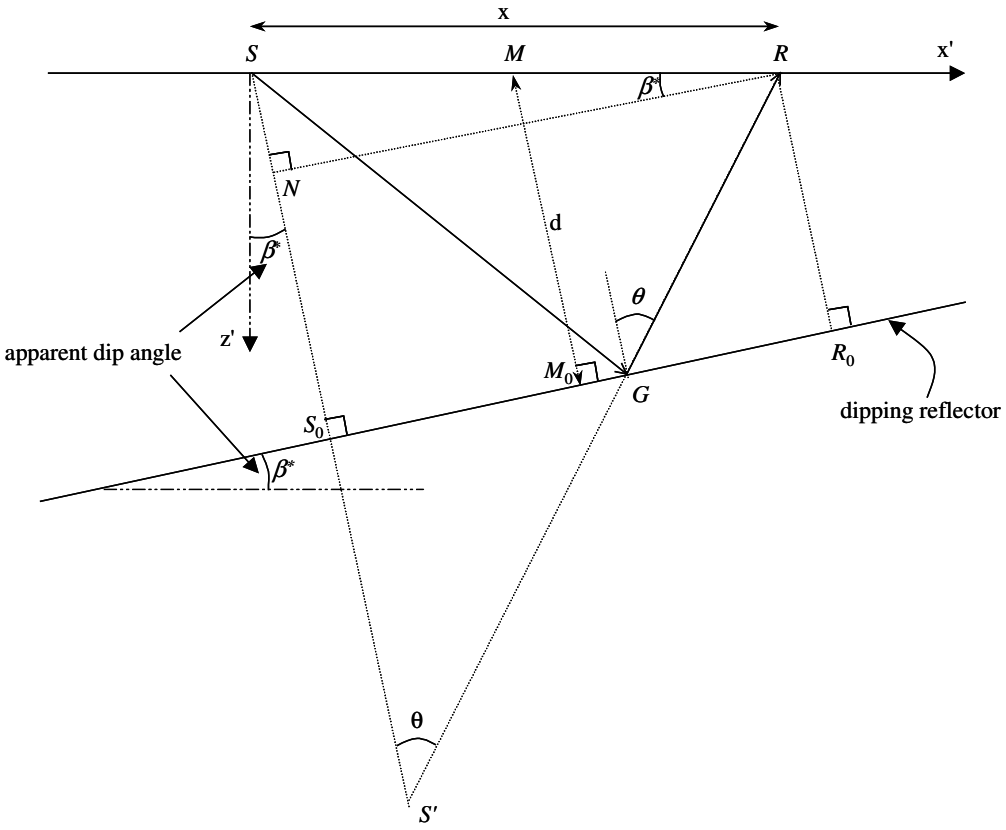

Figure 3.2. Geometry of a 2D seismic line with a dipping reflector.

By substituting equation (3.1d) into (3.3), equation (3.3) becomes

$$\cos\theta = \frac{2d}{\sqrt{4d^2 + x^2 - x^2 \sin^2 \beta \cos^2 \varphi}}. \qquad (3.4)$$

Note that the incident angle for the flat reflector ($\beta = 0$) with the same offset, θ_0, is defined by

$$\cos\theta_0 = \frac{2d}{\sqrt{4d^2 + x^2}}, \tag{3.5a}$$

$$\sin\theta_0 = \frac{x}{\sqrt{4d^2 + x^2}}. \tag{3.5b}$$

By using the relationship $\sin^2\theta = 1 - \cos^2\theta$ and after some manipulations, the incident angle for a dip reflector is

$$\begin{aligned}
\sin^2\theta &= 1 - \cos^2\theta = 1 - \frac{4d^2}{4d^2 + x^2 - x^2\sin^2\beta\cos^2\varphi} \\
&= 1 - \frac{4d^2}{4d^2 + x^2}\frac{1}{1 - \frac{x^2}{4d^2 + x^2}\sin^2\beta\cos^2\varphi} \\
&\cong 1 - \cos^2\theta_0(1 + \frac{1}{2}\sin^2\theta_0\sin^2\beta\cos^2\varphi)
\end{aligned}.$$

Therefore, as the first order approximation,

$$\sin^2\theta = \sin^2\theta_0(1 - \frac{1}{2}\cos^2\theta_0\sin^2\beta\cos^2\varphi). \tag{3.6}$$

Substituting equation (3.6) into Shuey's AVO equation (equation 2.6), the amplitude variation with incident angle and azimuth for the reflections from a dipping reflector is

$$R(\varphi) = A + B(1 - \frac{1}{2}\cos^2\theta_0\sin^2\beta\cos^2\varphi)\sin^2\theta_0. \tag{3.7}$$

By defining $D = -\frac{1}{2} B \cos^2 \theta_0 \sin^2 \beta$, equations (2.8) and (3.7) are the same. In practice, when seismic data are being processed, there is no knowledge if the reflector is dipping or not. For a dipping reflector in an isotropic medium, the pattern of the amplitude variation with azimuth is similar to a pattern for a flat reflector in an anisotropic medium. Therefore, it is impossible to distinguish what causes the amplitude variation with azimuth. It is necessary to remove the dip effect before azimuthal AVO analysis.

If the dipping angle of reflectors is small, the amplitude variation with azimuth caused by the dipping reflectors might not be significant. However, when the dipping angles are greater than 5^o, the effect of the dipping reflectors cannot be ignored. Figure 3.3 shows an example of the amplitude variation with azimuth caused by a dipping reflector (30^o) in an isotropic medium comparable to that caused by a flat reflector in an HTI anisotropic medium ($D = 0.05$).

Two models were used to generate this example. There are two layers and the top layer is isotropic for both isotropic (Figure 3.3(a)) and anisotropic (Figure 3.3(b)) models. The P wave velocity is 3300 m/s in the top layer and S wave velocity 1500 m/s. The P wave velocity is 3500 m/s in the lower layer and S wave velocity 2333 m/s for the isotropic model. For the HTI anisotropic model, the lower layer P wave velocity is 3500 and S wave velocity 2333 m/s along the direction of fracture orientation. There is a dipping reflector with a dip angle of 30^o in the isotropic model, while the HTI anisotropic model have a flat reflector and the fracture reflectivity, D, is 0.05. Amplitude curves are calculated (using equations 2.8 for the isotropic model and 3.7 for the anisotropic model) at different incident angles (0^o, 10^o, 20^o and 30^o, respectively).

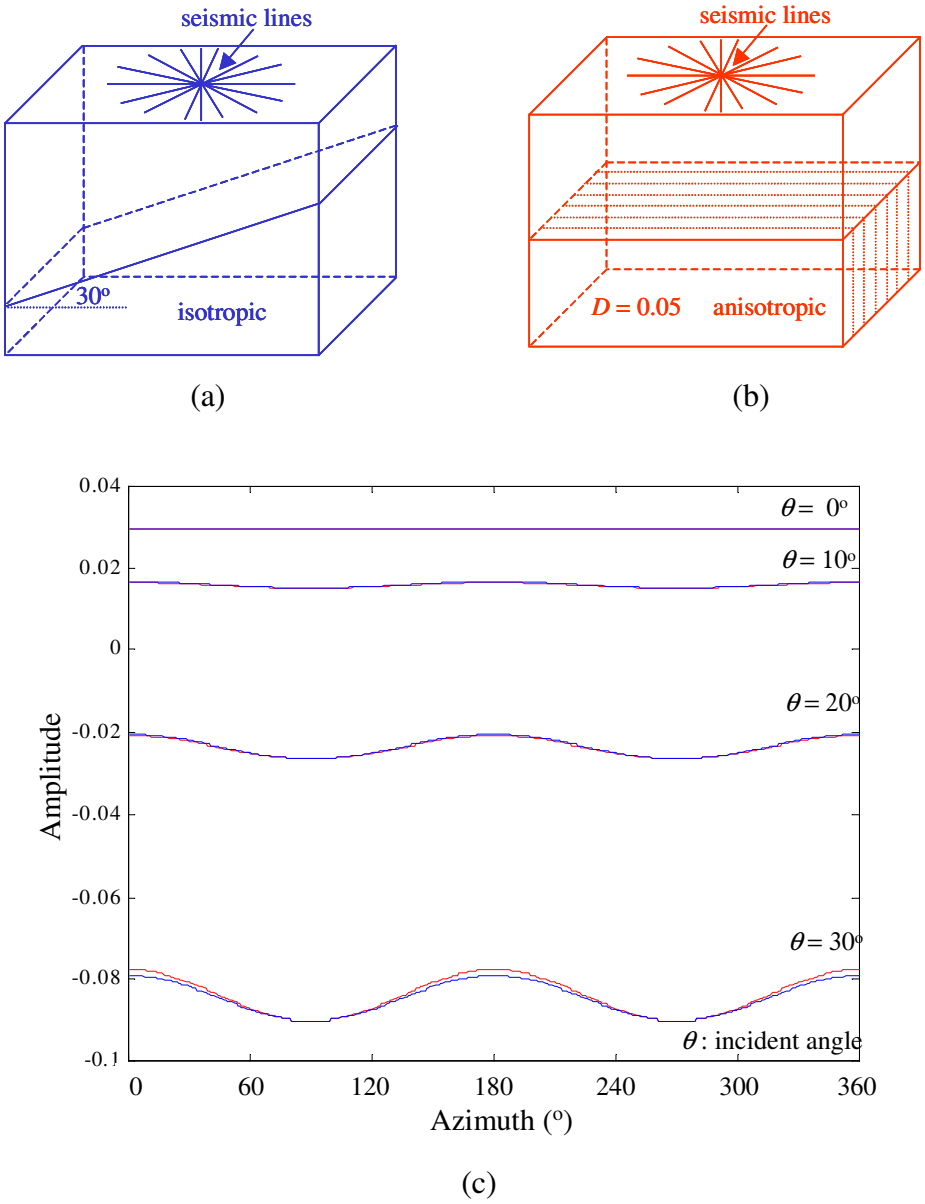

Figure 3.3. The comparison of amplitude from two models. One is (a) a dipping reflector on an isotropic medium, and another is (b) a flat reflector on an HTI medium. (c): Amplitude variations with azimuth from the two models are shown at four different incident angles (θ). Red curves show the amplitude from the HTI/flat reflector model, while the blues show the amplitude from the isotropic/dipping reflector model.

There are four pairs of curves in Figure 3.3(c). The red curves are the amplitude from the flat reflector on an anisotropic medium; and the blue curves are the amplitude

from the dipping reflector on an isotropic medium. As shown in the figure, the red and blue curves are very close. These two models create almost same amplitude response. If the dip effect is not removed before fracture analysis, it becomes difficult to distinguish whether the amplitude variation of azimuth is caused by azimuthal anisotropy or a dipping reflector.

Prestack migration can eliminate the impact of dipping reflectors, provided the algorithm preserves phase and amplitude. The next section will introduce a common-angle migration method, which removes the dip effect, reduces the incident angle smearing and produces amplitude-preserved migrated gathers for fracture analysis.

3.3 Positioning of fracture analysis and common-angle migration

Fractures often occur in highly structured areas (Zheng and Gray, 2002; Zheng and Wang, 2005). The reflection energy from a dipping reflector on unmigrated CMP gathers is smeared along the dip. However, fracture analysis is often applied on the unmigrated CMP gathers, resulting in two problems. One is incorrect positioning, and another is the dip-induced anisotropy ("false" fracture) as discussed in the previous section. The effect of these two problems can be effectively removed by applying fracture analysis on amplitude and azimuth preserved prestack migrated gathers.

Conventional prestack migration is often performed in common-offset domain, which may cause amplitude smearing in angle domain. Figure 3.4 is a Cheop's pyramid (traveltime surface of a 2D time migration operator) (a) and its map view (b) showing the 2D travel time from a scatter point in a constant velocity medium. A Cheop's pyramid is a surface defined in space (x, h, t), where x is migration offset (the distance from the CMP location of input trace to scatter point), h is half seismic acquisition offset (one half of the distance from source to receiver), and t is time. The shape of Cheop's pyramid is defined by the double square root (DSR) equation:

$$t = t_s + t_r = \sqrt{(\frac{t_0}{2})^2 + (\frac{x-h}{V_{rms}})^2} + \sqrt{(\frac{t_0}{2})^2 + (\frac{x+h}{V_{rms}})^2}\ , \qquad (3.8)$$

where t_0 is the vertical two-way time from the surface to the image point; t_s is the travel time from the source location to the image point; and t_r is the travel time from the receiver location to the image point.

For time migration, the scatter point is assumed to be located at the apex of the pyramid, and all possible reflection times lie on this surface defined by their pyramid. In principle, Kirchhoff migration sums the energy lying on the pyramid with proper weights, and places it at the apex. Common-offset migrated gathers are generated by summing the energy along constant offsets, and placing the energy at the scatter point location for each offset. Similarly, common-angle (incident angle) gathers can be generated by summing up energy along the common-angle (incident angle) lines.

In Figure 3.4(b), there are three sets of lines. The closed black lines are common travel times; the green lines are common incident angles; and the horizontal purple lines are common offset lines. Solid angles in (c) illustrate the same angle of incident at three spatial locations for a small angle of incidence, while (d) shows a larger angle of incidence. The correspondent common-angle lines are marked in dashed lines in (b). As shown in Figure 3.4, common-offset and common-incident angle lines are different. For a given offset, when the source and receiver are moving further away from the scatter point, the incident angle becomes smaller. When reflections along the common-offset lines are summed, the reflections from different incident angles are summed together. In other words, the incident angles are smeared. Because AVO analysis (and its extension, the amplitude method for fracture analysis) is performed in incident angle domain, it will be more accurate to migrate seismic data in common incident angle domain and output a common-angle migrated gathers for AVO analysis. This section presents a common-angle time migration method developed for this dissertation.

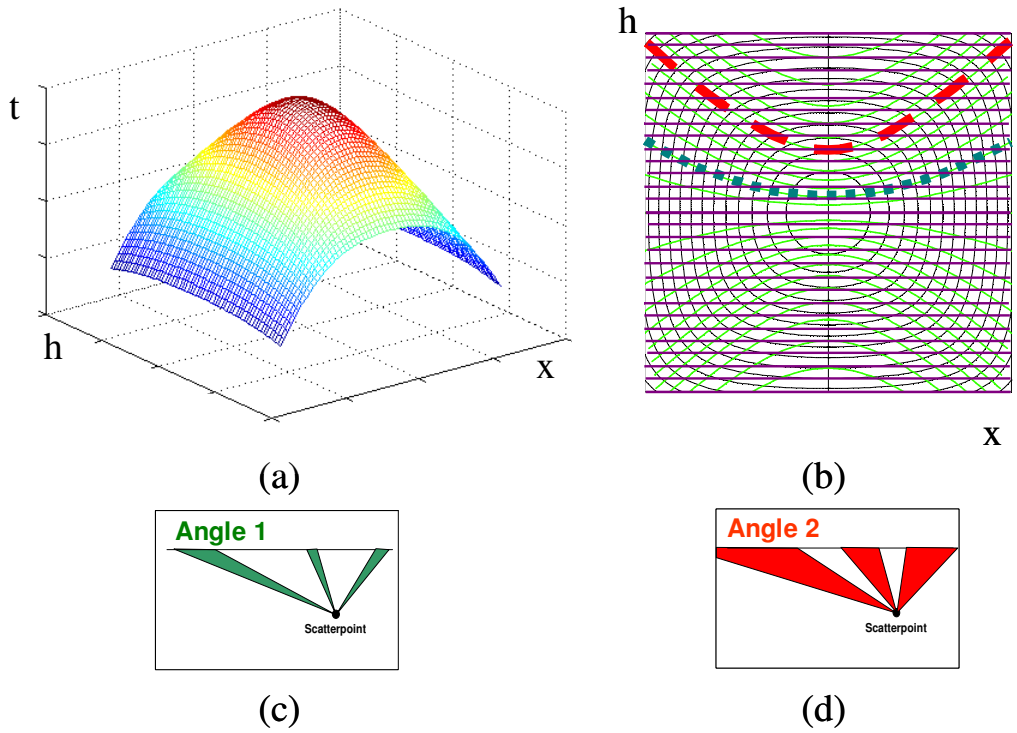

Figure 3.4. Cheop's pyramid (a) and its map view (b) showing the 2D travel time from a scatter point in a constant velocity medium. There are three sets of lines on (b). The closed black lines are common travel times (the contour of the Cheop's pyramid); the green lines are common incident angles; and the horizontal purple lines are common offset lines. Solid angles in (c) illustrate the same angle of incident at three spatial locations for a small angle, while (d) shows a larger angle (courtesy of J. Bancroft).

Travel times for 3D data can be mapped to a Cheop's shape by

$$t = t_s + t_r = \sqrt{(\frac{t_0}{2})^2 + (\frac{h_s}{V_{rms}})^2} + \sqrt{(\frac{t_0}{2})^2 + (\frac{h_r}{V_{rms}})^2}\ , \qquad (3.9)$$

where h_s is the distance from the source location to the image location and h_r is the distance from the receiver location to the image location (Figure 3.5).

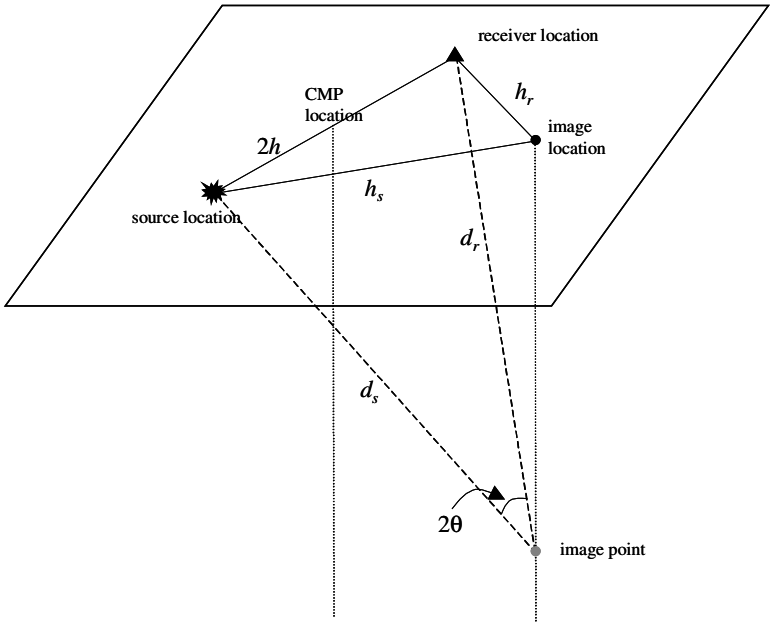

Figure 3.5. The diagram shows the calculation of incident angle of seismic wave reflected at an image point (scatter point) for given source and receiver locations.

The common-angle prestack time migration used in this dissertation assumes that, just like other time migrations, lateral velocity variation is moderate; therefore root-mean-square (RMS) velocity can be used for migration. The Kirchhoff migration operator (or Cheop's pyramid for 2D data) is only defined by the zero-offset two-way time and the RMS velocity at the location of the image point. The ray path from source point to image point or from image point to receiver point is a straight line on a time section. Ray bending due to vertical velocity variation is incorporated in the RMS velocity. The apparent length of the ray path are computed to the pseudo depth by assuming the RMS velocity is locally constant. The actual or true depth of the image point is computed using average velocity in all azimuths. For every input trace, the travel times from the source and receiver to every image point are calculated. The incident angles are also calculated as shown in Figure 3.5. For known locations of source, receiver and image point, the incident angle is one half of the opening angle between the incident and reflected rays, i.e.,

$$\theta = \frac{1}{4}\cos^{-1}\left(\frac{d_s^2 + d_r^2 - 4h^2}{2d_s d_r}\right), \tag{3.10}$$

where θ is the incident angle, d_s is the distance from source location to imaging point; d_r is the distance from receiver location to imaging point; and h is one half of the distance from source to receiver.

For 3D data, the total travel time t from source to image point (t_s) and image point to receiver (t_r) is calculated using the double square root (DSR) equation (equation 3.9). Once the total travel time is calculated, a sample on this trace at the corresponding travel time is weighted and accumulated on the output trace zero offset time t_0. After migration, the energy at a scatter point comes from all times that satisfy the DSR equation for this location, and migration moves the energy at each input point to all possible scatter point locations. In other words, migration is a mapping process that maps one point to whole volume, and whole volume to one point as well. In addition for common-angle migration, incident angle must also be calculated for every sample so that the samples in input traces can be migrated to correspondent angles in the output gathers (see Table 3.1 for details). A run-time comparison is done for the common-offset and the common-angle migration. The common-angle migration takes about 1.5 times more CPU time than the common-offset migration.

Table 3.1 Pseudo code for common angle time migration

```
for (i=0; i < ntraces - 1; i++) // loop through all input traces
{
    for (ii = 0; ii < N; ii++)     // prepare N copies of the input data for anti-aliasing
   {                               // with different high cut filter (Gray, 1992)
        fdata(ii) = highCutFilter(data);
   }

    for (j = 0; nlocations - 1; j++)       //  loop through all output locations
    {
        for (k = 0; k < nsamples - 1; k++)   // loop through all samples
        {
            v = vel(k);                    // get rms velocity
            hs = ; hr = ; ds = ; dr = ;  // calculated from geometry and depth of
                                           //  imaging point
            t0 = k * sampleRate;
            ts = sqrt(0.25 * t0^2 + hs^2 / v^2);      // travel time from source to
                                                      // imaging point
            tr = sqrt(0.25 * t0^2 + hr^2 / v^2);      // travel time from receiver to
                                                      // imaging point
            travelTime = tr + ts;
            weight = t0 / sqrt(tr * ts);              // oblique factor
            weight *= 1. / v^2 * travelTime;          // spherical spreading factor for 3D
            weight *= 1. / v * sqrt(travelTime);      // spherical spreading factor for 2D
            angle = int (0.25 * arccos((ds^2 + dr^2 - 4 * h^2) /
                    (2 * ds * dr)) * RADIAN2DEGREES + 0.5);
            fIdx =  ; // get the index of array fdata for the correct copy of input data
                      // based on the maximum frequency of the anti-aliasing
                      // filter (Lumley et al, 1994)

            // sum up data in output traces
            output(angle, j, k) += weight * fdata(fIdx, travelTime)
        }
    }
}

for(j = 0; nlocations; j++)     // loop through all output locations
{                               //  again to apply phase correction
    applyPhaseCorrection        //  45° for 2D, 90° for 3D
}
```

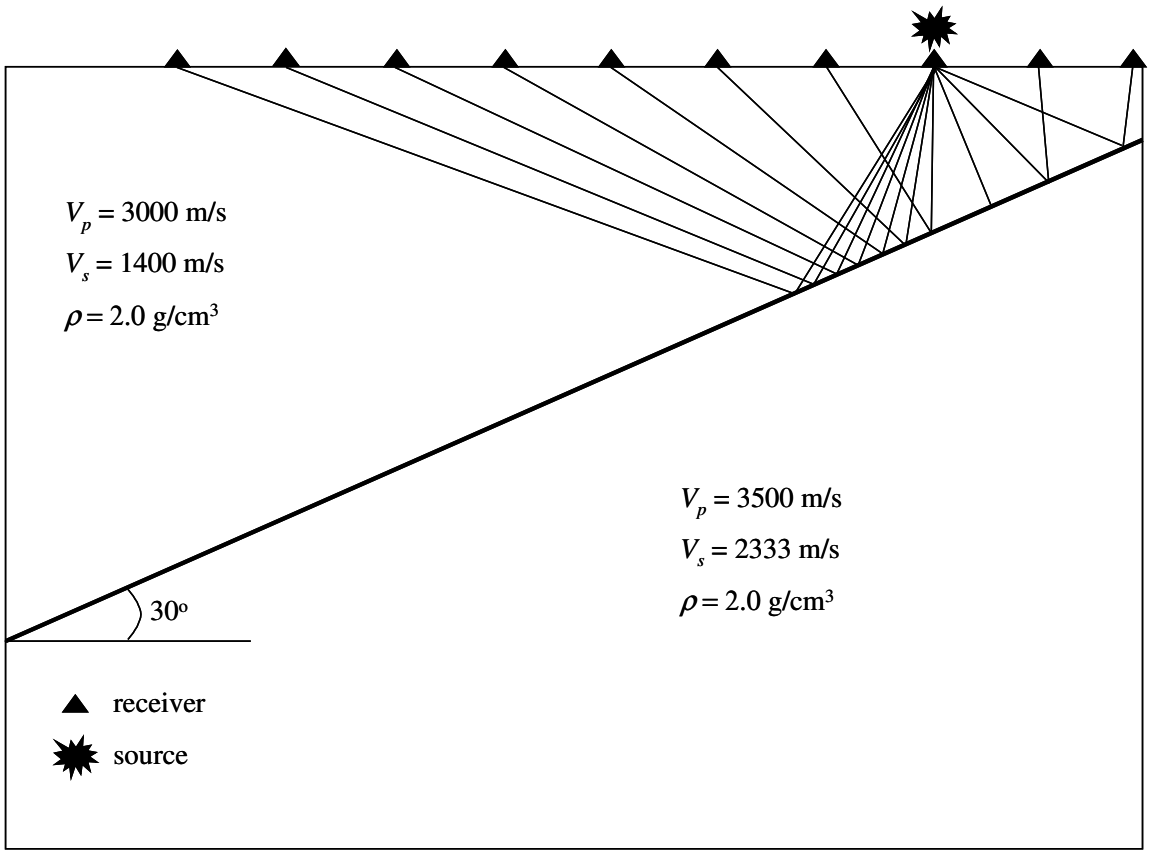

Figure 3.6. A 2D model with a single 30^o dip was used for testing common-angle migration. In the upper layer, the P wave velocity is 3000 m/s, and the S wave velocity is 1400 m/s. In the bottom layer, the P wave velocity is 3500 m/s, and the S wave velocity is 2333 m/s. The density in both layers is 2.0 g/cm^3.

3.4 Comparison of common-angle and common-offset migrations

The common-angle migration was tested on a 2D numerical modeling data set that was conducted using the ATRAK. The model consisted of two layers with a 30^o dipping interface (Figure 3.6). In the top layer, the P wave velocity is 3000 m/s, the S wave velocity is 1400 m/s and the density is 2.0 g/cm^3. In the bottom layer, the P wave velocity is 3500 m/s, the S wave velocity is 2333 m/s and the density is 2.0 g/cm^3. The maximum number of receivers per shot was 201, with 100 receivers on each side of the source location and one receiver at the source location with a receiver spacing of 20 m, the maximum offset was 2000 m. The source spacing was 80 m.

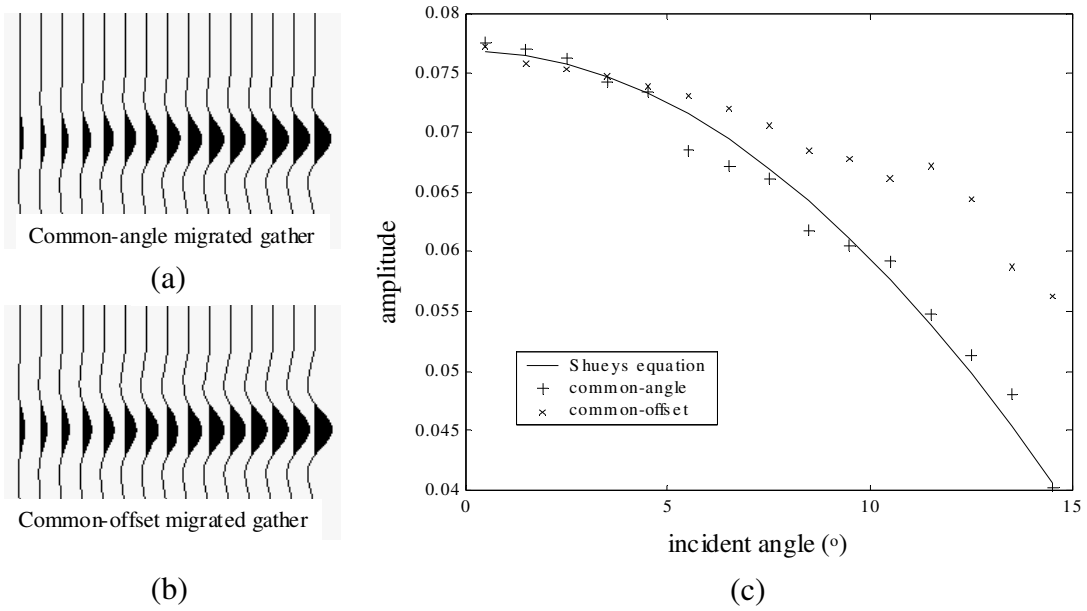

Figure 3.7 Amplitude comparison of prestack migrated gathers: (a) gathers from common-angle migration, (b) from common-offset migration, and (c) the comparison of amplitudes from both migrations at each incident angle.

Both common-angle and common-offset migrations were performed on the numerical synthetic data. The common-angle migration directly outputs to a common incident angle gather at each CMP location, while common-offset migration outputs a common-offset gather. For easy comparison, the output gathers of common-offset migration were converted to common incident angle gathers using a 1D layered velocity model (a common practice in seismic industry). Gathers from both migrations at a CMP point are shown in Figure 3.7. Figure 3.7 (a) is a common-angle migrated gather, and (b) is a common-offset migrated gather in angle domain. Amplitude values were measured at the peak of each gather and plotted in Figure 3.7 (c) that also shows theoretical values (solid line) calculated using Shuey's AVO equation (equation 2.7). The amplitudes from the common-angle migration (+) match the theoretical amplitudes better than that of common-offset migration (x), and the incident angle for common-offset migration is overestimated.

The relationship between the amplitude and incident angle is important for AVO analysis. As illustrated in the above modeling example, the AVO results from common-angle migrated gathers will be more accurate than that from common-offset migration. There are two factors causing the common-offset migration to yield less accurate amplitudes of migrated gathers. The first is the smearing of the incident angle in common-offset migration (see Figure 3.4(b)) where energy is summed along the horizontal lines (purple lines). However, the incident angles along a common offset line vary, therefore the incident angle is smeared. The second factor is that the estimation of the incident angles on the migrated gathers is based on the 1-D velocity model, which is incorrect. If the 1-D velocity model is valid assumption, there is no need to apply migration. The common-angle migration preserves amplitudes and solves the two problems simultaneously.

The common-angle migration was also applied to a 3D field data set in the Pinedale area, Wyoming, USA. There is a thrust fault-fold system in the area. For details about this area, please refer to Chapter 5 of this dissertation.

A line of common-angle migrated data is shown in Figure 3.8 (a). On the section, it is clearly shown the fold system and a fault on the west frank of the fold. As a comparison, the common-offset migrated section of the same line is shown on Figure 3.8 (b). Overall, the two sections give similar structure of the fault-fold system. However, the common-angle migration provides more details, especially the image of the fault on the west flank of the fold (highlighted by an oval), because applying area weighting (Zheng et al., 2001) in common-angle domain works better than in common-offset domain.

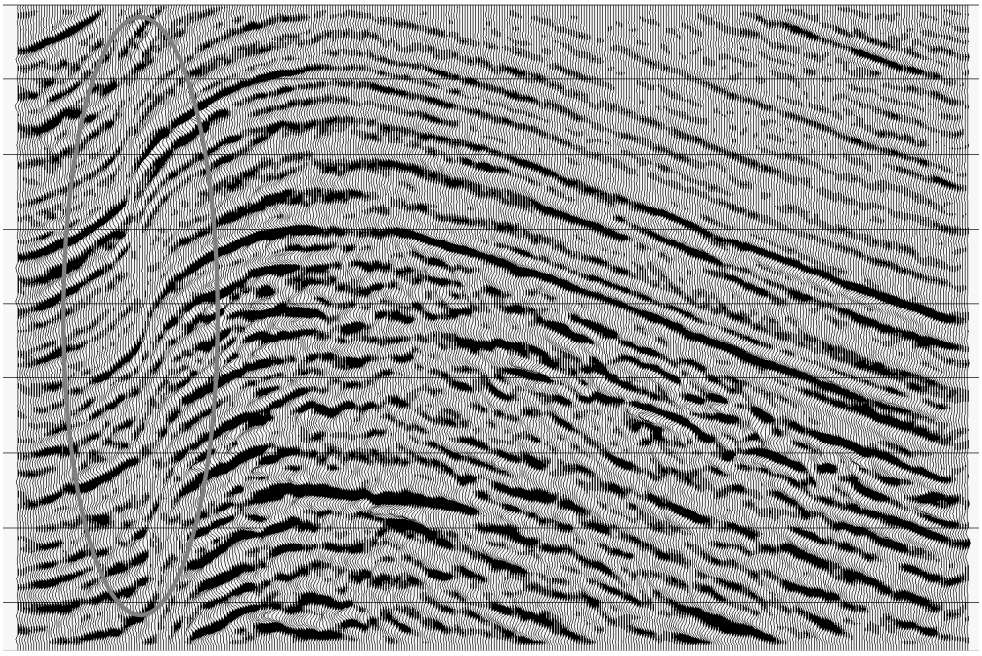

(a)

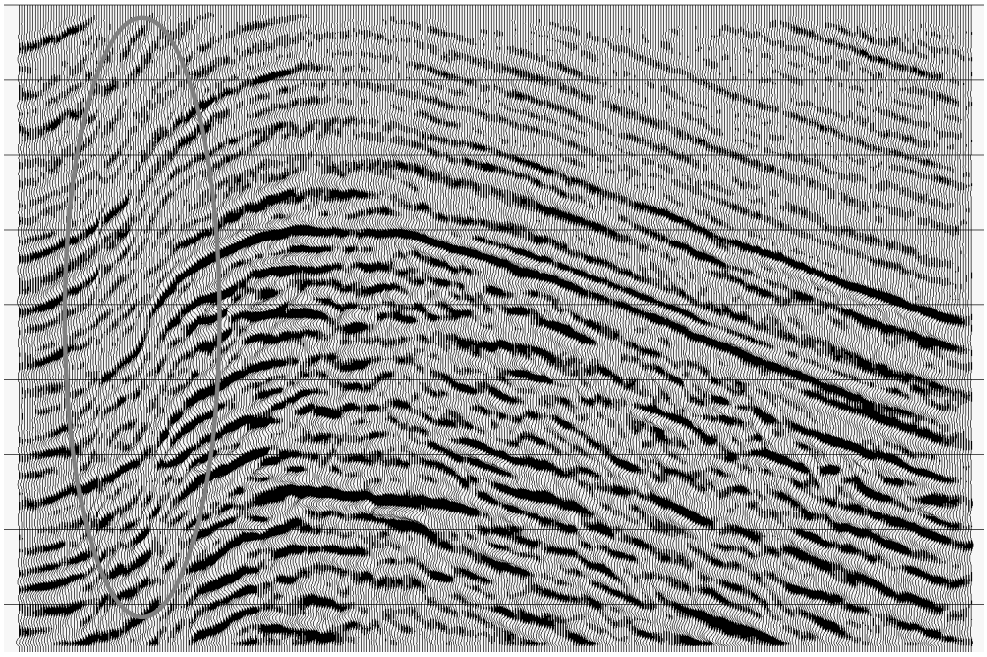

(b)

Figure 3.8. Migrated sections: (a) common-angle migration, (b) common-offset migration. Common-angle migration provides slightly better image of the structure, especially the fault highlighted by an oval.

Based on the tests conducted on the synthetic and field data sets, common-angle migration not only preserves amplitude information, but also gives slightly better image than the conventional common-offset migration.

3.5 Extraction of the Thomsen's parameter, $\delta^{(v)}$, from residual moveout

Li (1999) indicated that the residual moveout of the reflection from the bottom of a fractured layer varies sinusoidally with azimuth. Tsvankin (1997) gave NMO velocity at an arbitrary azimuth equation (2.10). This equation can be expanded to extract the Thomsen's parameter $\delta^{(v)}$ directly from the residual moveout for a fractured zone.

A fractured reservoir layer beneath an isotropic overburden is illustrated in Figure 3.9. The velocity of the isotropic overburden is V_1 and the thickness is d_1. The velocity of the fractured reservoir layer is $V_2(\varphi)$, which is a function of azimuth, and the thickness of the layer is d_2. The total thickness of the two layers is $d = d_1 + d_2$. The two-way vertical travel time for these two layers are: $t_{01} = 2d_1 / V_1$, and $t_{02} = 2d_2 / V_2$, respectively. Therefore the RMS velocity for the bottom of the fractured layer (Dix, 1955) is

$$V_{rms}^{\ 2} = \frac{t_{01}V_1^2 + t_{02}V_2^2}{t_{01} + t_{02}} = \frac{t_{01}V_1^2 + t_{02}V_2^2}{t_0}, \tag{3.11}$$

where V is the RMS velocity for the bottom of the fractured layer.

The variation of t_0 may be negligible for most cases, because for most reservoirs, the thickness of the reservoir, d_2, is far less than the thickness of the overburden, d_1, and the velocity variation with azimuth in the fractured layer is small. With the assumption of constant t_0, by differentiating both sides with respect to V_2, equation (3.11) becomes

$$\Delta V_{rms} = \frac{1}{2}\frac{t_{02}}{t_0}\frac{V_2}{V_{rms}}\Delta V_2 . \qquad (3.12)$$

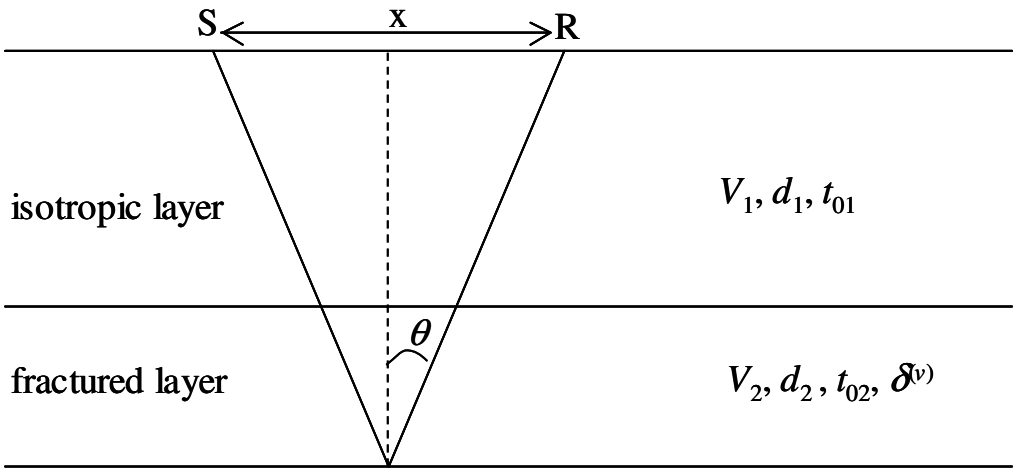

Figure 3.9. An isotropic overburden with the velocity V_1 and thickness d_1 is on the top of a fractured reservoir with the velocity V_2 and thickness d_2. The total thickness of the two layers is $d = d_1 + d_2$.

Equation (3.12) gives the relationship of the RMS velocity changes versus the velocity change in the fractured zone.

The NMO equation for the reflection from the bottom of the fractured layer is

$$t^2 = t_0^2 + \frac{x^2}{V_{rms}^{\ 2}}, \qquad (3.13)$$

where x is the distance between seismic source and receiver, t is the seismic travel time from the source to the receiver, and V_{rms} is the RMS velocity defined by equation (3.11). By differentiating both sides, equation (3.13) becomes

$$\Delta t = -\frac{1}{t}\frac{x^2}{V_{rms}^{\ 3}}\Delta V_{rms}, \tag{3.14}$$

where Δt is the residual moveout caused by the velocity perturbation ΔV_{rms}. By using the relationship $\cos\theta = t_0 / t$ (where straight ray assumption is applied), after combining equations (3.12) and (3.14) and some manipulations, the residual moveout can be expressed as

$$\Delta t = -\frac{1}{2t}\frac{x^2}{V_{rms}^{\ 3}}\frac{t_{02}V_2}{t_0 V_{rms}}\Delta V_2, \tag{3.15a}$$

$$\Delta t = -\frac{t_{02}V_2}{2V_{rms}^{\ 2}}\frac{t_0}{t}\frac{x^2}{t_0^2 V_{rms}^{\ 2}}\Delta V_2, \tag{3.15b}$$

$$\Delta t = -\frac{d_2}{V_{rms}^{\ 2}}\frac{t_0}{t}\frac{x^2}{4d^2}\Delta V_2, \tag{3.15c}$$

$$\Delta t = -\frac{d_2}{V_{rms}^{\ 2}}\cos\theta\sin^2\theta\Delta V_2. \tag{3.15d}$$

The velocity perturbation of the fractured layer with respect to the strike direction of the fractures can be obtained from equation (2.10),

$$\Delta V_2 = V_{02}\delta^{(v)}\cos^2\varphi, \tag{3.16}$$

where, V_{02} is the velocity in the direction of the fracture strike. φ is the angle between the seismic ray path and the fracture strike direction.

By substituting equation (3.16) into equation (3.15), residual moveout at the bottom of the fractured layer can be expressed as

$$\Delta t = -\frac{d_2 V_{02}}{V_{rms}^{\ 2}} \delta^{(v)} \cos\theta \sin^2\theta \cos^2\varphi, \qquad (3.17)$$

where V_{rms} is the RMS velocity at the bottom of the fractured layer. V_{02} is the interval velocity of the fractured layer along the direction of the fracture strike. $\delta^{(v)}$ is the Thomsen's parameter of the fractured layer. θ is the incident angle of the seismic wave. φ is the azimuthal angle between the seismic ray path and the fracture strike direction.

Equation (3.17) can be used for δ inversion to get both $\delta^{(v)}$ and the strike direction of the fractures, although there is an ambiguity in the direction. The issue of ambiguity will be discussed in the next section.

To avoid the influence of overburden azimuthal anisotropy, events on the top and bottom of the reservoirs should be picked and the residual statics should be calculated for both events. The difference of the residual statics is the residual moveout purely caused by the reservoir, therefore, it should be the input for the δ inversion.

3.6 Ambiguity of the estimated fracture orientation

From the fracture analysis of wide-azimuth PP reflection seismic data, the estimated fracture reflectivity is relative stable and not influenced by the polarity of the seismic data. However, fracture orientations cannot be uniquely extracted from PP seismic data and the estimated fracture orientations are sensitive to the polarity of seismic data. Other information besides the amplitudes and NMO velocities of PP seismic data is required to uniquely determine the fracture orientation.

For the amplitude method of fracture analysis, Rüger's equation (equation 2.8) is used in the industry to extract fracture information from the amplitude of seismic records. For a given incident angle, the amplitude variation curve is a sinusoid with a period of 180^o. There are four unknowns in the equation, A, B, D and φ_0. There is an intrinsic

ambiguity when equation (2.8) is used for inversion. Mathematically, there is no unique solution from equation (2.8), no matter how many data are available. If the sign of D is changed, B is regrouped and at the same time φ_0 is rotated by 90^o, another set of D, B and φ_0 that still satisfy the equation can be found. In other words, for a given data set, $R(\varphi, \theta)$, there are always two sets of resolutions, (A, B, D, φ_0) and (A, B', D', φ_0') for equation (2.8), where $B' = B + D$, $D' = -D$ and $\varphi_0' = \varphi_0 - 90$. When only fracture property is concerned, changing the sign of fracture reflectivity D is equivalent to rotating the fracture orientation φ_0 by 90^o. In practice, there is no knowledge of the sign of D before fracture analysis. Therefore, during the analysis in this dissertation, fracture reflectivity D is forced to be positive, but now the detected fracture orientation might be in error by 90^o, because D could be either positive or negative.

If the polarity of the seismic data is changed by 180^o, the estimated fracture orientation will be in error by 90^o. Changing polarity is equivalent to multiplying by –1 to the two sides of equation (2.8). Thus the fracture reflectivity becomes negative (assuming it is positive in reality). Since D is forced to be positive in the analysis, the estimated fracture orientation, φ_0, will be rotated by 90^o. By taking the seismic wavelet effect into account, for an interface with positive D, at the times with negative amplitude, the estimated fracture orientation will be rotated by 90^o.

In conclusion, the estimated fracture orientation from the amplitude method might be the true fracture orientation, or might be perpendicular to the true fracture orientation. In other words, there is a 90^o ambiguity for the estimated fracture orientation.

Similar to the amplitude method, the fracture orientation detected from the NMO velocity method, the residual moveout method or the δ inversion also has the 90^o ambiguity, because the equations used for these methods, equations (2.10), (2.11) and (3.17), are similar to Rüger's equation (2.8) and have no unique solutions. These methods share the same intrinsic ambiguity as the amplitude method.

Additional information is needed to help solve the ambiguity. The information can be FMI logs, core samples, regional stress field, or fast shear wave direction from shear wave splitting analysis of PS converted waves.

3.6.1 Synthetic data examples

Synthetic datasets were created to test the fracture analysis method with different polarities of seismic data. The synthetic datasets were modeled using Rüger's equation (equation 2.8). This will give some ideas how the polarity of the seismic data affects the results of fracture analysis. The model has an isotropic layer on the top with P wave velocity 3000 m/s and S wave velocity 1500 m/s, underlying by a fractured layer. The fracture layer has a P wave velocity 3300 m/s, S wave velocity 1700 m/s along the direction of fracture orientation, $\delta^{(v)} = 0$, $\gamma^{(v)} = 0.05$ the fracture orientation is 45°. The reflection interface is a Class I type interface (Rutherford & Williams, 1989) with positive intercept (A) and negative gradient (B). The fracture orientation is set to 45° (φ_0) and the fracture reflectivity (D) is positive. A synthetic gather with a zero phase Ricker wavelet was created using equation (2.8) (Figure 3.10 (a)). A gather with negative polarity (Figure 3.10 (b)) was generated by multiplying –1 on the gather in Figure 3.10 (a). Then fracture analysis with the amplitude method was then applied to these gathers. During the inversion, D was forced to be positive.

Figure 3.10 shows the results of fracture analysis for different polarities of the input gathers. There are two rows and three columns. The top row is positive polarity and the bottom row is negative polarity. The first column shows the seismic gathers as the input of fracture analysis. The second column is the estimated fracture reflectivity for the correspondent gathers. The vertical axis of both the first and second columns is time. The third column is the estimated fracture orientation in map view in the CMP bin associated with the input gather at the time marked by a horizontal line in the first and second columns. When the polarity of the input gather is positive, the estimated fracture

orientation is 45°, which matches the model. While the polarity of the input gather changed to negative, the estimated fracture orientation is –45°, which is in error by 90°, compared to the known input model.

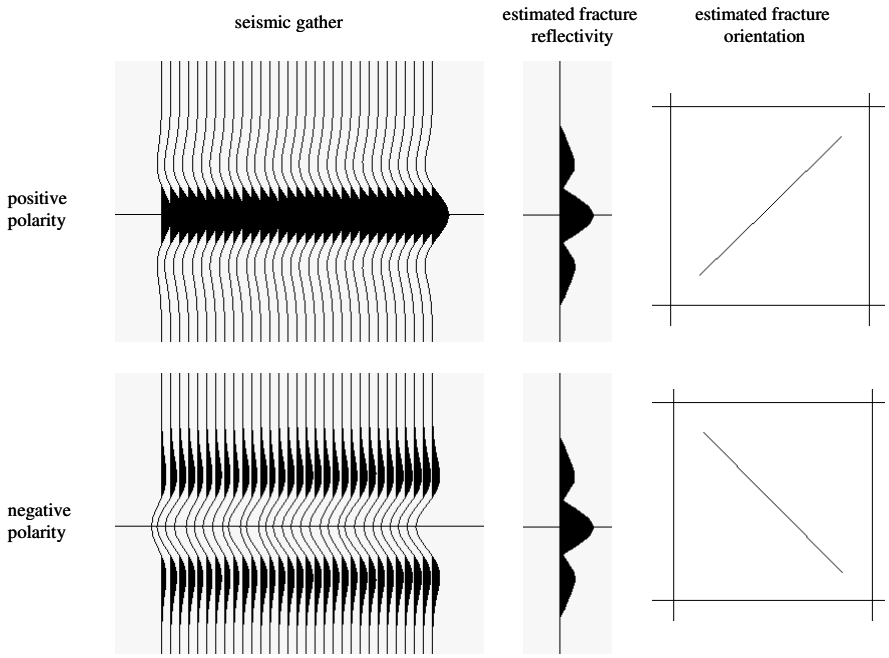

Figure 3.10. Results of fracture analysis for the different polarities of the input gather. The first column shows the seismic gathers as the input of fracture analysis; and the second column is the estimated fracture reflectivity for the correspondent gathers. The vertical axis of both the first and second columns is time. The third column is the estimated fracture orientation in map view in the CMP bin associated with the input data at the time marked by a horizontal line in the first and second columns. The top row is in positive polarity and the bottom row is in negative polarity.

To investigate the 90° ambiguity of the estimated fracture orientation for the NMO velocity method and the residual moveout method, synthetic models (Figure 3.11(a)) were built using the ATRAK modeling package. The models are composed of three layers with an azimuthally anisotropic layer in the middle, and both the first and

third layers are isotropic. The strike direction of the fractures is at 90° azimuth. The P wave velocity of the first layer is 2800 m/s, 3000 m/s for the second layer along the direction of the fracture strike, and 3500 m/s for the third layer. The Thomsen's parameter $\delta^{(v)}$ of the second layer is negative (-5.5%) for one model and positive (+2%) for another. Eighteen (18) 2D lines were shot at different azimuths (every 10°) (the same acquisition geometry as that in Figure 2.2) for both models.

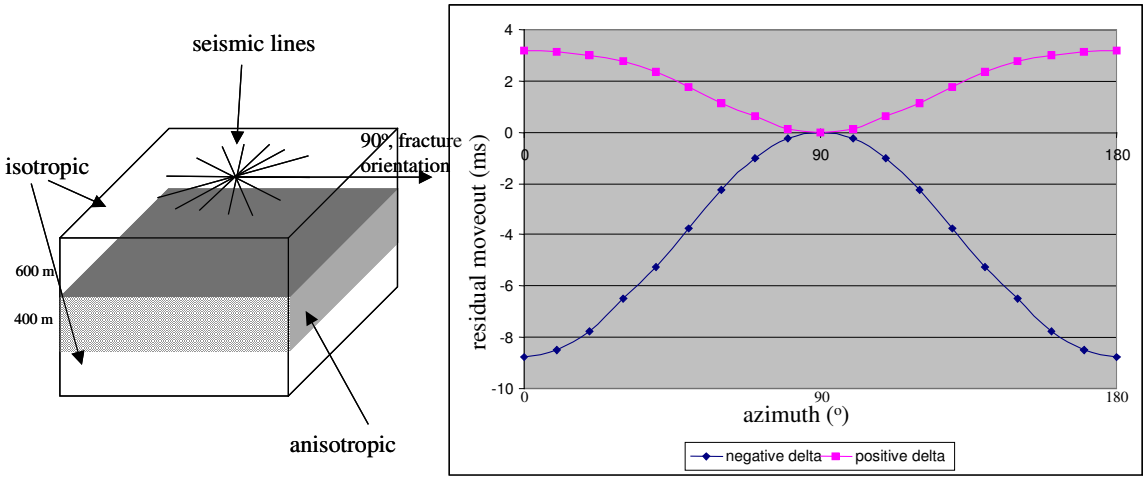

Figure 3.11. (a) The model used for tests. (b) Residual moveout (measured as time shift at an offset of 1000 m) for the reflection from the bottom of the fractured layer. The blue diamonds represent the residual moveout from the model with negative $\delta^{(v)}$ (-5.5%), the pink squares for positive $\delta^{(v)}$ (+2%). Both pink squares and blue diamonds show sinusoidal pattern, but with opposite polarities. The azimuth angle is measured from the axis of symmetry (perpendicular to fracture strike).

For both modeling datasets, the reflections from the bottom of the fractured layer were NMO corrected using the isotropic RMS velocity for the bottom of the reservoir. After NMO correction, the residual moveout (measured as time shift at an offset of 1000 m) were picked (Figure 3.11(b)). The residual moveout from the model with negative (blue diamonds) and positive (pink squares) $\delta^{(v)}$ both show sinusoidal pattern with a

period of 180°, but with opposite polarities. When $\delta^{(v)}$ is negative (-5.5%), the fast NMO velocity (or the most negative moveout) is in the fracture strike direction. When $\delta^{(v)}$ is positive (+2%), the slow NMO velocity (or the most positive moveout) is in the strike direction of the fractures. Without knowing the sign of the $\delta^{(v)}$, it is impossible to determine the fracture orientation from NMO velocity or residual moveout alone. It is not always true to assume the direction of the fast NMO velocity is the direction of fracture strike, although many people think so.

3.6.2 Field data example

One 3D seismic dataset from a gas field in Alberta, Canada was used to test the impact of different polarities of the seismic gathers on the estimated fracture orientation. Figure 3.12 shows one line of estimated fracture reflectivity and orientation from the amplitude method. On the left side, the color shows the fracture reflectivity and the wiggle traces are the seismic stacked section. Red color represents high fracture reflectivity and green means low fracture reflectivity. Purple color means there are no significant fractures. A deviated well 11-24 is marked in black line; and the top and bottom of the reservoir (formation Fahler G) is marked in red and purple on each section. On both top and bottom of the reservoir, there are high values of the fracture reflecivities. On the right side, the estimated fracture orientation is shown in color, and every thing else is the same as that on the left side. The estimated fracture orientation at the top of the reservoir is –40° and at the bottom, 50°. The difference between them is 90°. Note that the top of the Fahler G is in a trough on the stacked section, while the bottom of Fahler G is in a peak on the stacked section. Therefore, the polarities of seismic data for the top and bottom of the reservoir are different. It is not surprising that the estimated fracture orientation is different by 90° for the top and bottom of the reservoir. From the PP seismic data alone, it is not clear which is the correct fracture orientation.

In order to solve the ambiguity of the detected fracture orientation, geological interpretation and FMI (**F**ormation **M**icro**I**mager) log were integrated. FMI log can provide a high resolution (~5 mm) downhole image showing the orientation of fractures. The FMI log from well 11-24 (provided by Devon Canada) indicates that the fracture orientation in the Fahler G formation is 55°, and the orientation was confirmed by interpreters. Therefore the orientation detected from seismic data is correct at the base and in error by 90° at the top of the reservoir. The information from the interpretation of the FMI log solves the ambiguity. The fracture reflectivity shows there are fracture density changes at the top and bottom of the reservoir.

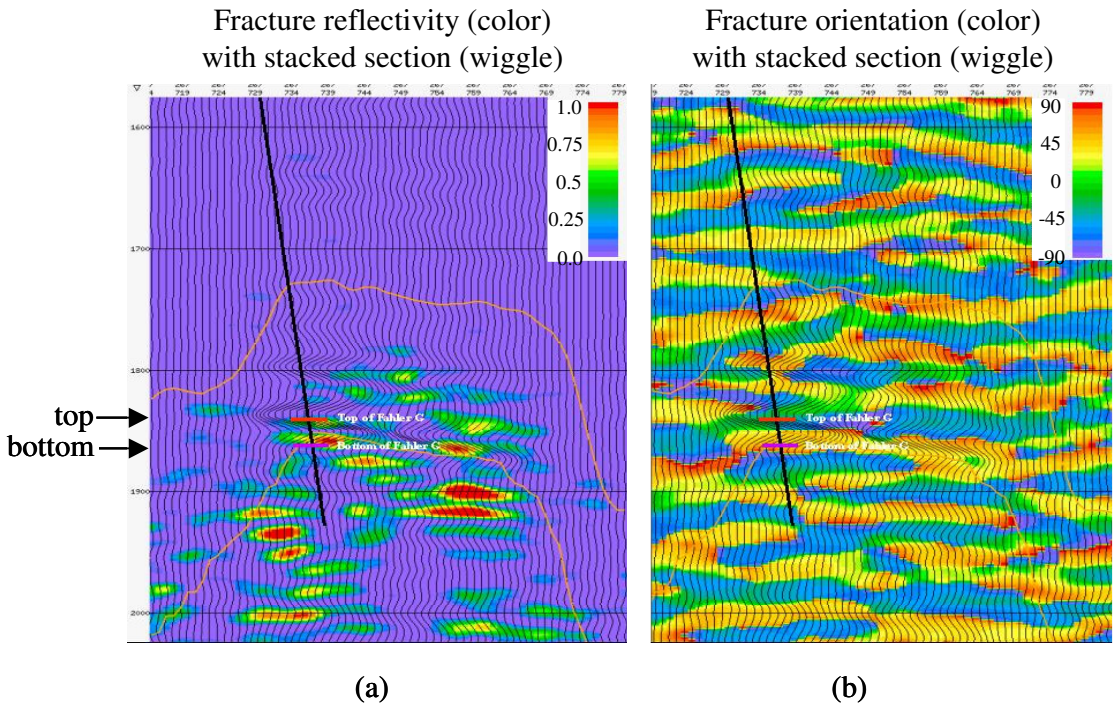

Figure 3.12. The left panel (a) is fracture reflectivity (color). The background wiggle traces are stacked section. The right panel (b) is fracture orientation (color) with stacked section (wiggle). A deviated well is marked by a black line and two short horizontal bars indicate the top (red) and bottom (purple) of the reservoir (Fahler G). At the bottom of the reservoir, fracture analysis gives correct fracture orientation. However, at the top of the reservoir, the orientation is off by 90°.

3.7 Summary

There are many factors that may affect the reliability and accuracy of fracture analysis. Some of them can be controlled during the processing in order to minimize their impact, such as both dip-induced "anisotropy" and mispositioning of fracture information in structured areas can be eliminated by common-angle migration. However, the ambiguity of the estimated fracture orientation cannot be solved by PP reflection data alone. The ambiguity may be solved by integrating information from well logs, regional stress field, core samples, or PS converted wave data.

The Thomsen's parameter, $\delta^{(v)}$, can be extracted from the residual moveout of the reflection from the bottom of the fractured layer. The extracted $\delta^{(v)}$ can be used as an indicator of fractures and to crosscheck the fracture reflectivity obtained from the amplitude method.

3.8 A recommended processing flow for fracture analysis

Theoretically, common-azimuth and common-angle depth-migrated gathers are the best for fracture analysis in a complex, structured area. However, they are costly. Alternately, common-azimuth and common-angle time migration is cost-effective. A practical workflow for fracture analysis is presented here. As shown in Figure 3.13, fracture analysis starts from amplitude preserved gathers. It is a challenging task to obtain amplitude preserved gathers. Noise and multiples must be carefully removed from the data, and the signal is carefully scaled so that the relative amplitude in time, offset and azimuth is preserved. Surface consistence scaling and deconvolution should be used instead of trace-by-trace scaling and deconvolution, to avoid the distortion of amplitude and phase of the gathers.

When the lateral velocity change is not significant, the seismic ray path can be approximately assumed to be restricted in the plane defined by these three points, source, receiver and image point. Therefore, the azimuth of the subsurface ray path at the image point can be assumed to be the same as the surface acquisition azimuth. To preserve azimuth information during migration, the gathers are split into a few azimuthal sectors based on the acquisition azimuth (the azimuth defined by the direction from source location to receiver location). More sectors mean a more accurate azimuth, however there is a lower fold in each sector with a corresponding decrease of signal-to-noise level. In practice, eight sectors might be optimal to balance the quality of migration and the accuracy of azimuth for most surveys.

For most land surveys, the distribution of seismic traces for each incident angle is not even or the spatial sampling in angle domain is irregular. When the gathers are split into azimuthal sectors, the situation becomes worse. To compensate this irregularly sampled data, area weighting (Zheng et al., 2001) is used for this purpose. The properly weighted gathers on each azimuth sector are then input into a common-angle, true amplitude prestack migration algorithm to get migrated common incident angle gathers.

By merging the migrated common-angle gathers from all sectors, amplitude and azimuth preserved migrated gathers in incident angle domain are obtained. Since the migration velocity used at this processing stage is isotropic, there is usually some residual moveout on the reflection from the bottom of fractured zone. The residual moveout is calculated for each horizon and applied to the migrated gathers. Now there are two datasets. One set is the prestack common-angle migrated gathers with residual moveout removed (data A). The other is residual moveout for each horizon (data B). Two different methods of fracture analysis can be used for the datasets, the amplitude method for data A and the δ inversion for data B. The fracture information calculated from both methods can be crosschecked. If they do not agree with each other, the previous steps of processing must be reviewed and the data require reprocessing until the fracture information detected by the two methods agrees.

Please note that the amplitude method measures the fracture (anisotropy) reflectivity on all interfaces, while the δ inversion utilizes the travel time difference of seismic waves traveling in different directions through the whole thickness of the fractured zone to extract Thomsen's parameter $\delta^{(v)}$. Therefore, the amplitude method can provide higher resolution for the distribution of fractures in time, while the δ inversion can only give a general trend, or an average $\delta^{(v)}$ over the entire fractured zone. The pattern of the fracture distributions from both the amplitude method and the δ inversion should be similar. The similarity or correlation of the fracture distribution derived from the amplitude method and the δ inversion will increase the reliability of the result of fracture analysis.

In this dissertation, the estimated fracture reflectivity is normalized so that the values are between 0 and 1, because typically the seismic data were scaled (multipled) by an arbitrary constant. The meaningful part of the values is the contrast of the values from one place to another. The higher values correspondent to higher fracture reflectivity, and vice versa. Therefore, normalized fracture reflectivity will make the interpretation more straightforward than the absolute fracture reflectivity.

The last step of fracture analysis is to eliminate the ambiguity of the measured fracture orientation, which needs extra information other than PP seismic data. The extra information may come from well logs, regional stress field, core samples, a seismic converted wave survey or pure shear wave survey. When shear wave information is available, it is also possible to quantify another Thomsen's parameter, $\gamma^{(v)}$, which is the relative difference of the fast and slow shear wave velocities.

In the next two chapters, the application of integrating the amplitude method and the δ inversion will be presented. The above workflow will be tested on a physical modeling dataset and a field dataset.

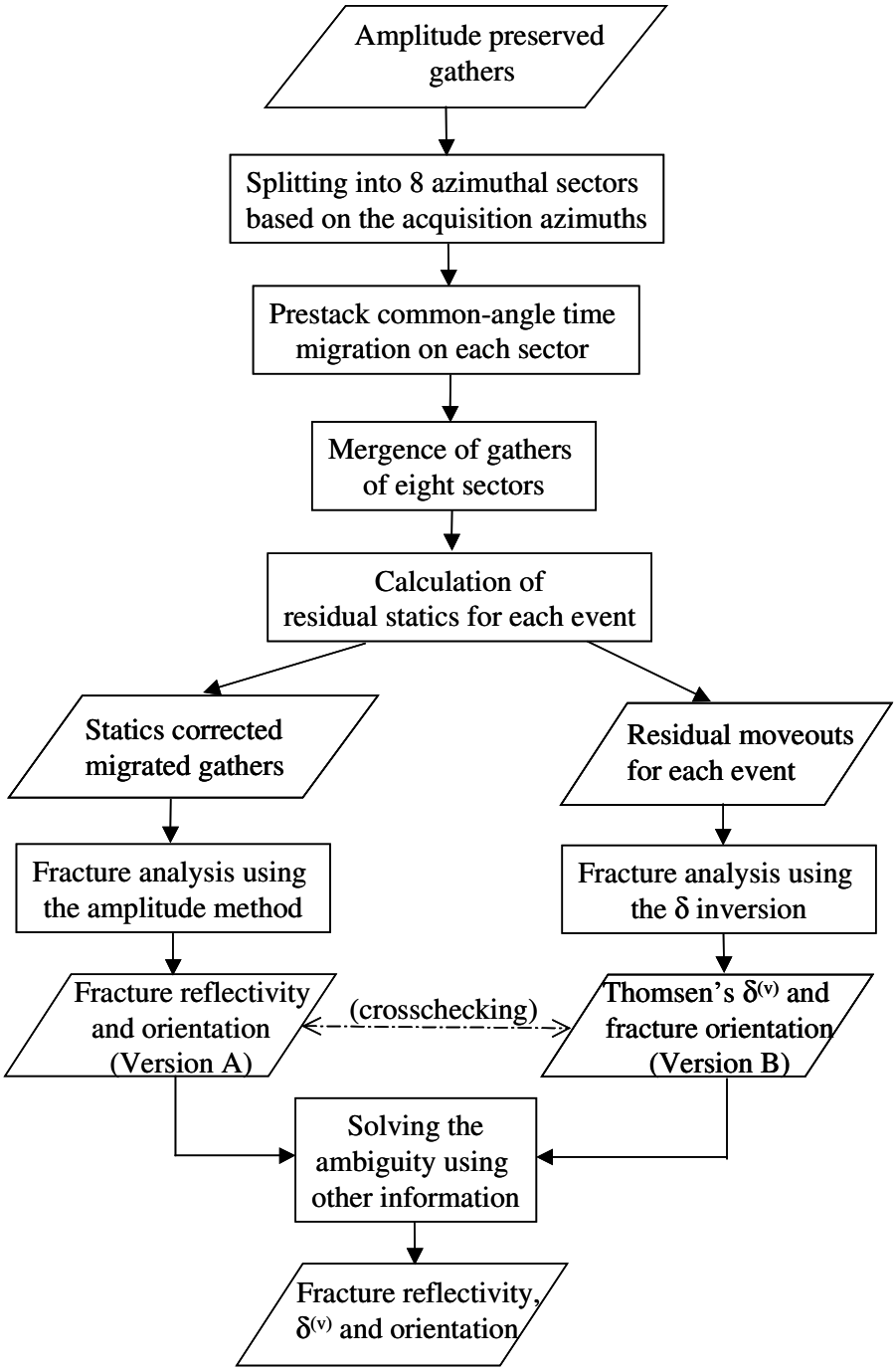

Figure 3.13. A recommended processing flow for fracture analysis in complex structured areas using both the amplitude method and the δ inversion. It is cost-effective to employ prestack common-angle time migration on azimuthally sectored data.

Chapter Four: Application of fracture analysis to physical modeling data

4.1 Introduction

To evaluate the workflow described in the previous chapter, fracture analysis was applied to a physical modeling dataset. The modeling data were created by the Geophysical Key Lab, China National Petroleum Corporation (CNPC). Permission was exclusively given to use the dataset and publish the results for this PhD dissertation. Since the model is known, it is easy to judge if the result of the fracture analysis is correct. Analysis of real data will be presented in the next chapter.

This physical modeling dataset provided a good opportunity to test the workflow presented in Chapter 3, since the acquisition geometry is similar to land seismic survey. The fractured zone is thick enough to introduce detectable residual moveout at the bottom of the layer for using δ inversion. An important feature of the model is that there are geological structures on the bottom of the fractured layer so that the imaging capabilities of the common-angle prestack migration can be tested.

4.2 Model composition and data acquisition

The physical modeling experiment was conducted by the Geophysical Key Lab. The model (Figure 4.1) consists of three layers. The first and third layers are made of epoxylite, which is isotropic with a P wave velocity 2648 m/s and an S wave velocity 1180 m/s. The second layer (to simulate fractures) is composed of epoxy-bounded vertically orientated fiber sheets, which is azimuthally anisotropic and its fast P and S wave direction is along the X-axis (90^o azimuth), and its slow P and S wave direction is along the Y-axis (0^o azimuth). Therefore, simulated fractures are orientated in the X-axis direction and the axis of symmetry of the fractured zone is in the Y-axis direction. The anisotropy is about 10%. The fast P and S wave velocities are 3642 m/s and 2010 m/s in

X direction, while the slow P and S wave velocities are 2960 and 1490 m/s in Y direction. $\delta^{(v)}$ of the fracture zone is about -13.5%. In the bottom of the anisotropic zone, there are two milled out structures, a dome and a thrust fault. The model was submerged in water at an equivalent depth of 1470 m, simulating a deep-water environment and reducing the contamination of surface wave and surface related multiples. The modeling scale is 1:10,000 for temporal and spatial dimensions; and the scaling for velocity is 1:1. The equivalent thickness of the first layer is 495 m; the second layer 602 m; and the third layer 690 m (Wang and Li, 2003).

A wide-azimuth P-wave reflection survey was recorded on the water surface (Wang and Li, 2003). The acquisition geometry is shown in Figure 4.2. There are 1040 source locations in total. The receiver patch is 12 lines x 64 receivers. There are in total 768 receivers for every shot. The sampling rate is 1 ms and the record length is 5 s. To ensure wide azimuth coverage, sources are located in the center of the receiver patch. Receiver lines are perpendicular to the fracture direction, and source lines are parallel to the fracture. In Figure 4.2, four source locations are highlighted in red and the live receivers for these sources are highlighted in blue. After firing four shots, the receiver patch was moved to the next position and another four shots were fired.

Both source and receiver intervals in equivalent distance are 50 m. The natural CMP bin size is 25 x 25 m. The normal fold is 48. The minimum offset is 200 m and the maximum offset is 2122 m. The equivalent depth of the bottom of the fractured layer is 2564 m; the equivalent depth of the top of the two structures (a dome and a thrust fault) is 2354 m. At each CMP location, the offset and azimuth coverage is fairly good, except that there is no acquisition azimuth on the east-west direction, because of the limitation of the modeling device. The distributions of offset and azimuth are shown in Figure 4.3.

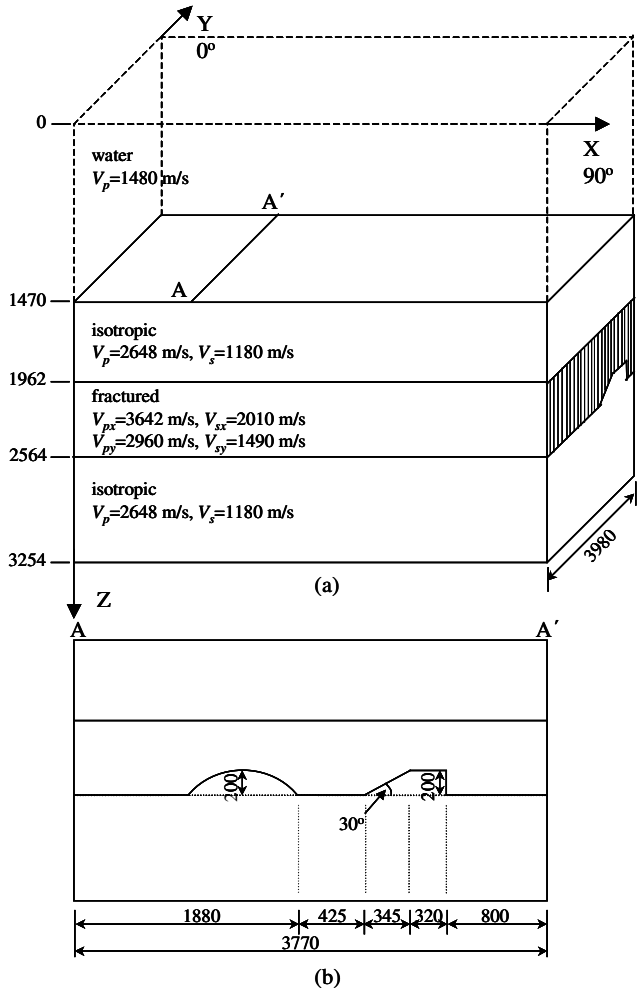

Figure 4.1. Model used for physical experiment in equivalent distance (m). (a) 3D view of the model. (b) A 2D section through the center of the dome. There are two structures on the bottom of the fractured layer, a dome and a thrust fault.

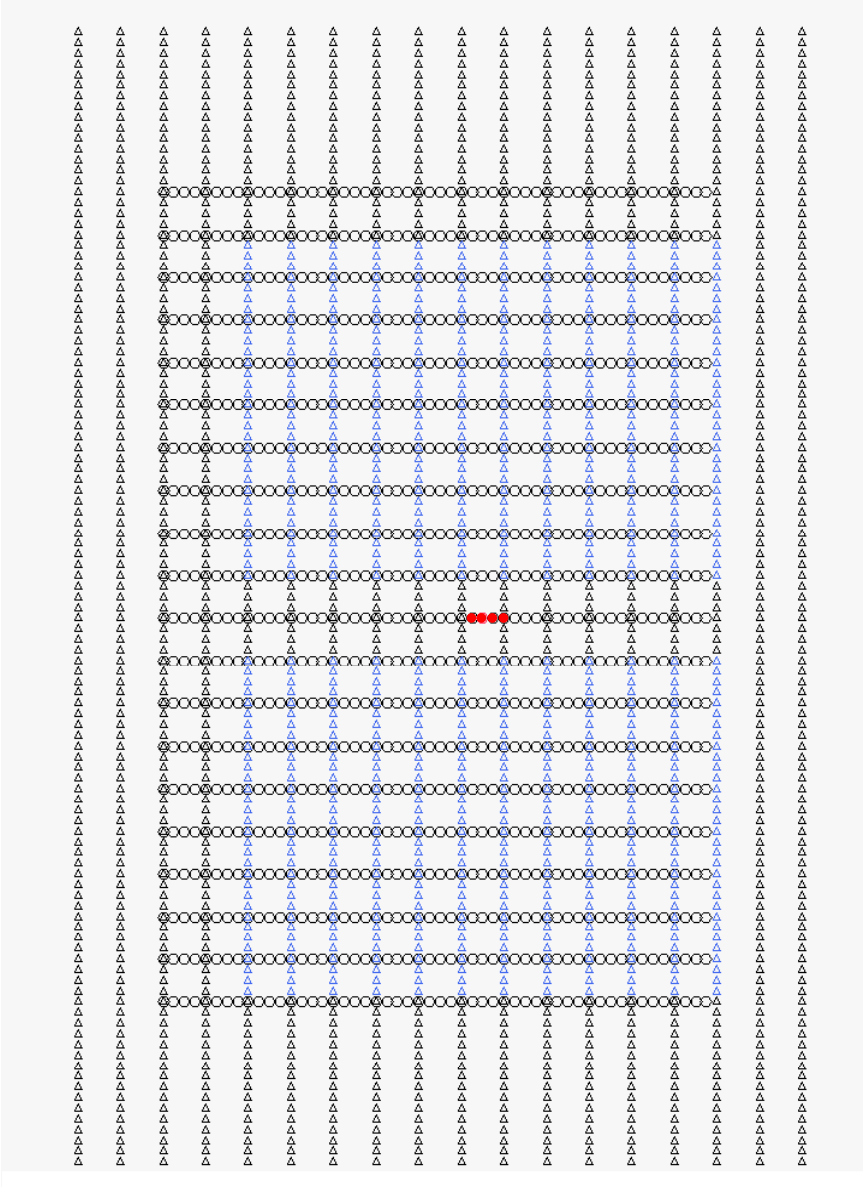

Figure 4.2. The acquisition geometry of the physical modeling experiment. The circles represent source locations and the triangles represent receiver locations. The blue color highlighted receivers are the live receivers for the sources highlighted in red color in the center of the blue receivers.

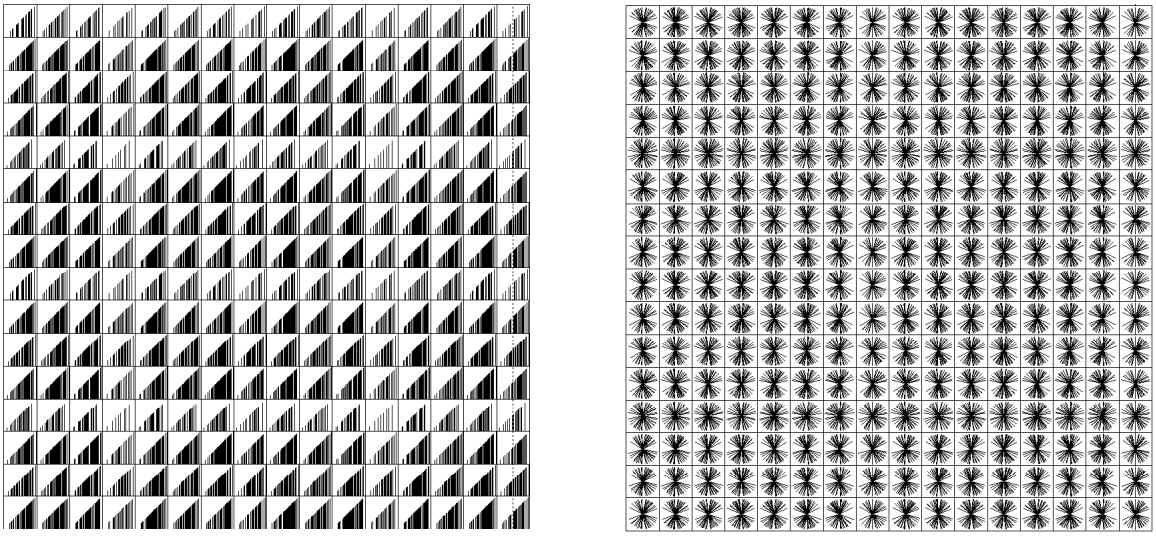

(a) (b)

Figure 4.3. The distribution of offset and azimuth at different CMP locations (each square represents a CMP). (a) Offset distribution. The length of the vertical bars is proportional to the offset. (b) Azimuth distribution. The directions of the bars indicate the directions of acquisition azimuths.

Since both sources and receivers are on the surface of the water, only PP waves were recorded. There might be some interbed converted waves in the recordings, but they are not of interest in this dissertation. Figure 4.4 shows a raw record with Automatic Gain Control (AGC) applied in order to show all reflections. The quality of the data is good. The four primary reflections can be observed, i.e., the water bottom, the top of the fractured layer, the bottom of the fractured layer, and the bottom of the model. The first two primaries are positive peaks, since the first two interfaces have positive impedance contrast (the impedance of the lower layer is higher than that of the top layer). The third and fourth primaries are negative troughs, because the bottom of the fractured layer and the bottom of the model are interfaces with negative impedance contrast. There are also some interbed multiples and possible interbed converted waves in the record with weaker amplitude compared to the primaries. Because the water layer is thick enough, there is no interference of surface multiples with the four primary reflections.

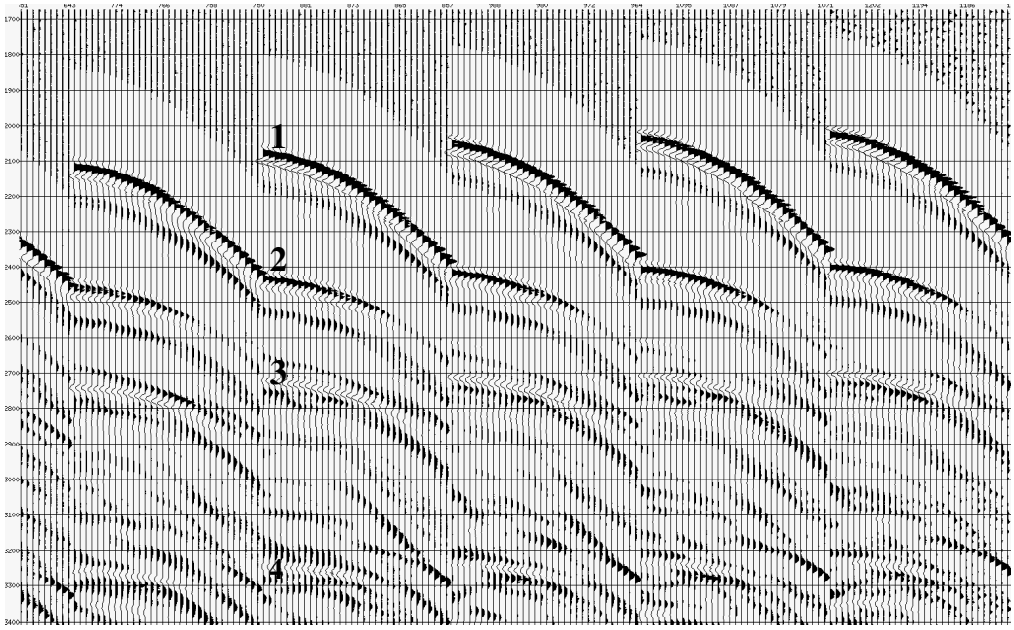

Figure 4.4. A raw record with AGC applied. Four primary reflections are clearly shown. (1) the water bottom; (2) the top of the fractured layer; (3) the bottom of the fractured layer; and (4) the bottom of the model. There are also some multiples and possible interbed converted waves in the record.

4.3 Analysis and interpretation

The pre-processing and data conditioning are relatively straightforward for physical modeled data, because the velocities are known. However there are residual statics on the data, which are caused by small depth variation of sources and receivers. The maximum static is about 20 ms, which translates to an error of about 1.5 mm in depth for sources or receivers. Trim statics were applied to the first reflection (from the water bottom), because the water is isotropic and it should not cause any azimuthal velocity anisotropy. Spherical diverge compensation was applied to the raw data. Then the gathers were divided into eight azimuthal sectors. Each sector is 22.5^{o} wide. For example, the first sector contains the traces whose source-receiver azimuths are in the range from -11.25^{o} to 11.25^{o} and from 168.75^{o} to 191.25^{o}. Area weighting (Zheng et al., 2001) was applied to the data of each sector prior to migration to compensate for the

irregularity of the acquisition geometry. Prestack common-angle time migration was then applied. After migration, the migrated gathers in common-angle domain from the eight sectors were merged together to form amplitude and azimuth preserved, prestack migrated angle gathers.

The migration of the fractured zone used an average velocity; therefore, the third event on the migrated gathers is not flat. Figure 4.5 contains common azimuth stacks at various angle of incident from a super bin (5 x 5 CMPs) of the migrated gathers. Traces in each panel have the same incident angle, but different azimuth directions. The azimuth values increase from right to left from 0^o to 180^o by 22.5^o in each panel. Incident angles increase for different panels from right to left from 6^o to 17^o. The top two events are flat at all incident angles. The third event is not flat, especially at large incident angles. This is the reflection from the bottom of the fractured zone. The P wave velocity of the fractured zone varies in different azimuthal directions, which causes azimuthal variation of residual moveout. At small incident angles, the variation is small. The variation increases with the incident angles. At the incident angle of 16^o, the maximum residual moveout from the fractured zone is about 15 ms. The variation of residual moveout versus azimuth is in sinusoidal pattern. The minimum travel time tends to be at 90^o azimuth and the maximum travel time occurs at 0^o azimuth. Note that the traces at 90^o azimuth are dead, because there are no data recorded in the direction due to the limitation of the modeling device.

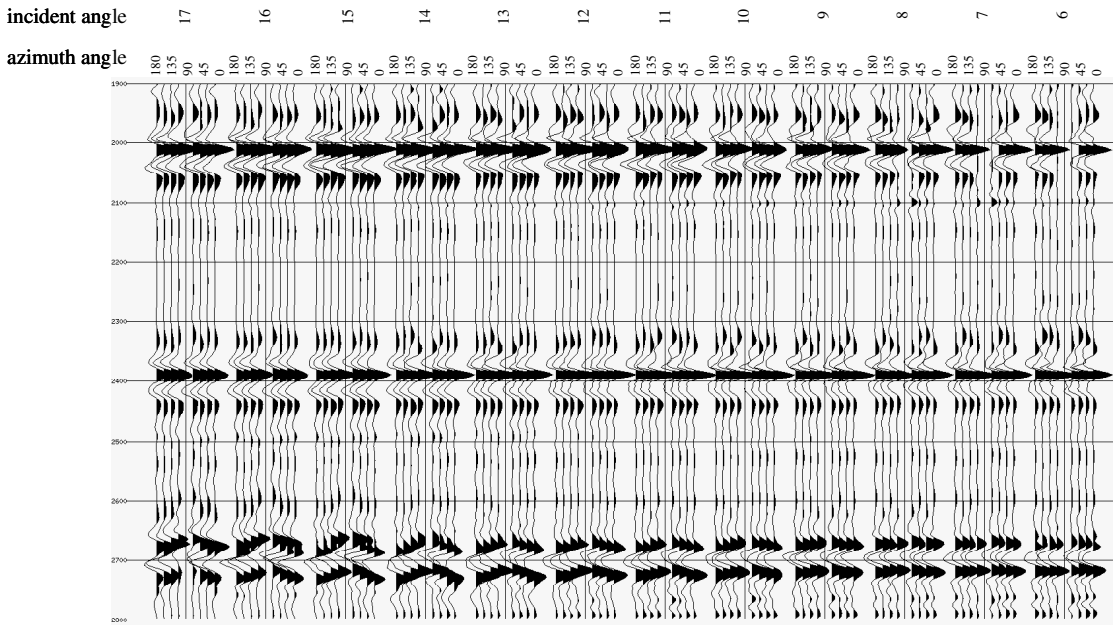

Figure 4.5. Common-angle and common-azimuth stack on a super bin (5 x 5 CMPs) from prestack migrated gathers. Traces in each panel have the same incident angle, but different azimuth angles. The azimuth values increase from right to left from 0^o to 180^o by 22.5^o. Incident angles increase in each panel from right to left from 6^o to 17^o.

To eliminate the impact of the travel time difference in different azimuthal directions, residual statics were estimated and applied for each of the three events, at the water bottom, and the top and the bottom of the fractured zone. As expected, the residual moveouts for the first and second events are negligible. There are significant residual moveouts for the third event, the bottom of the fractured layer. Figure 4.6 shows a migrated, common azimuth and common incident angle stacks with residual moveout correction. Residual statics were calculated and applied to the seismic data. After applying the statics, the amplitude method of fracture analysis was applied to the flattened gathers. The δ inversion was used to calculated the Thomsen's anisotropic parameter $\delta^{(v)}$ from the residual statics measured from the third event.

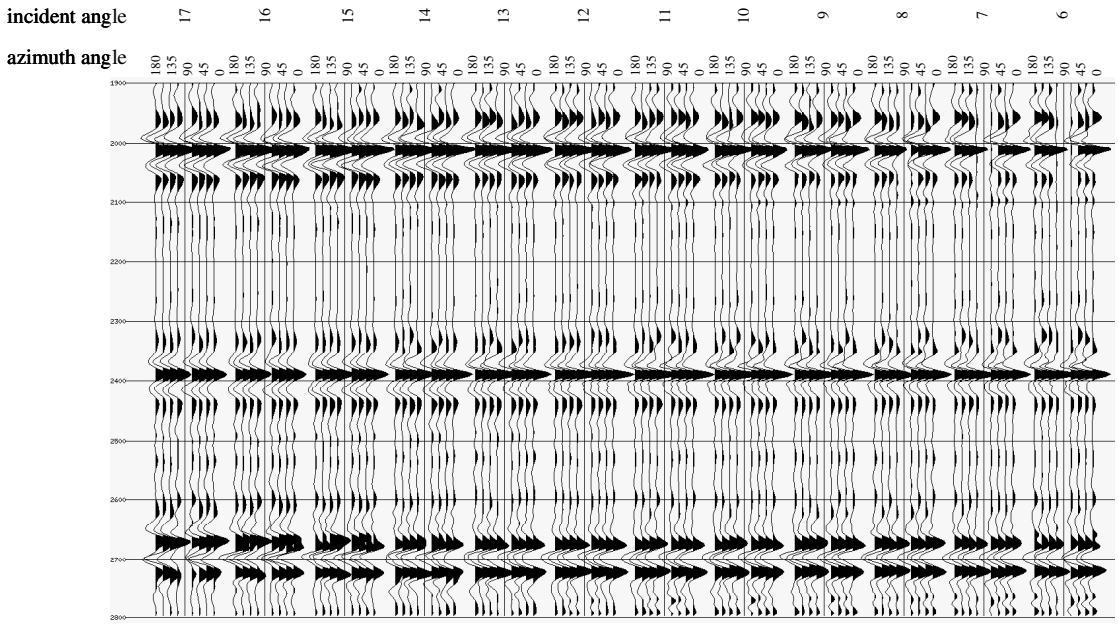

Figure 4.6. Common-angle and common-azimuth stacks from the migrated gathers with residual moveout correction applied to the third event. The gathers can now be used for fracture analysis using the amplitude method.

The result of the amplitude method shows fracture reflectivity on the top and the bottom of the fractured zone (Figure 4.7). In the figure, there are two profiles and one time slice. One profile is along the direction of X-axis, which is parallel to the strike direction of the thrust fault, and the other is along the direction of Y-axis and goes through the dome (the same line as the profile in Figure 4.1 (b)). The time slice is at the bottom of the fractured zone. Two structures of the model are clearly shown in the measured fracture reflectivity. The gray scale shows the intensity of the fracture reflectivity. The lighter the color is, the higher the fracture reflectivity. High fracture reflectivity shows up on the top and bottom of the fractured zone, and little elsewhere due to noise.

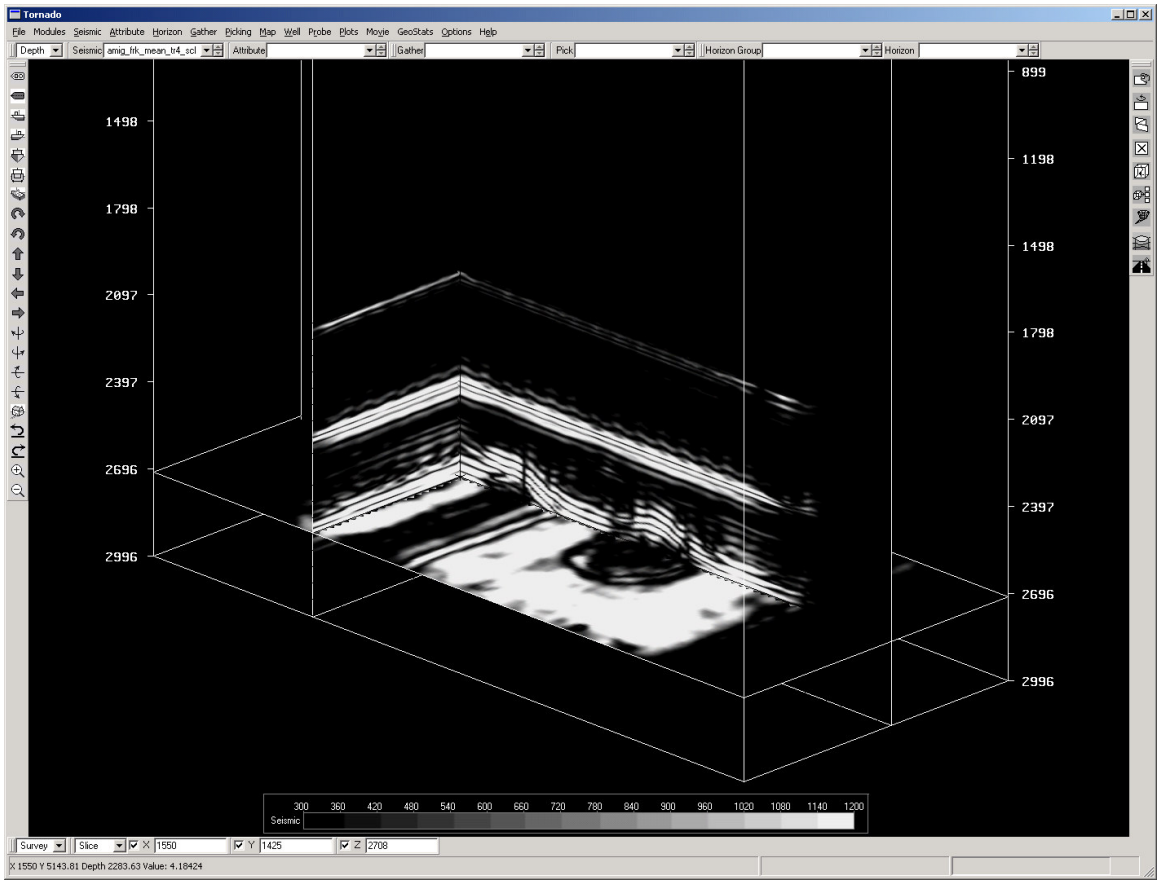

Figure 4.7. Fracture reflectivity obtained from the fracture analysis using the amplitude method. There are two profiles and one time slice in this figure. One profile is parallel to the strike direction of the thrust fault and another is perpendicular to the first one and goes through the dome. The time slice is at the bottom of the fractured zone. Two structures of the model are clearly shown in the measured fracture reflectivity.

On the bottom of the fractured zone, the measured fracture reflectivity follows the structure, except some weakness of the fracture reflectivity on the flanks of the dome. The reason for the weakness of fracture reflectivity is that the normal fold of the survey is only 48. When the data are split into 8 parts, the average fold for each part is only 6. Migration noise is expected to be high especially for high dip structures. The migration noise affects the result of the fracture analysis. Because of the slight variation of the

amplitude of the water-bottom reflection in the raw records caused by modeling system, the result of the fracture analysis shows slight fracture reflectivity.

Figure 4.8 shows the normalized fracture reflectivity from the amplitude method on prestack common-angle migrated gathers overlaid on migrated stack. The color represents the intensity of the measured fracture reflectivity. Red means high. Figure 4.9 is a profile of measured fracture orientation on prestack common-angle migrated gathers with the background wiggle traces of migrated stack. The red color is 90^o and the blue color 0^o. From the description of the model, it is known that the correct orientation of the fracture is 90^o. Because there is 90^o ambiguity of the measured fracture orientation, independent information is needed (Zheng et al., 2004). Taking this into consideration, in this example the amplitude method of fracture analysis on the prestack migrated gathers gives the correct fracture orientation.

The above results are compared with the normalized fracture reflectivity from unmigrated CMP gathers (Figure 4.10) and post stack migrated fracture reflectivity (Zheng and Gray, 2002) (Figure 4.11). The fracture reflectivity from unmigrated gathers is in the wrong place for the bottom of the fractured zone. After post stack migration, the fracture reflectivity moved toward the correct location, but it is still not good.

The residual moveout of the third event (base of the fractured zone) are used in the δ inversion of fracture analysis. The result indicates the fast velocity direction is about in 90^o direction, which is consistent with the observation that the reflection of the third event has the shortest travel time in 90^o direction (Figure 4.5). Meanwhile, it is known that the fracture direction of the model is in 90^o direction, therefore the Thomsen's parameter, $\delta^{(v)}$, must be negative (Equation 2.10). Figure 4.12 shows the distribution of $\delta^{(v)}$ extracted from the residual moveout of the third event, or the reflection from the base of the fractured zone. The color represents the values of $\delta^{(v)}$, and the short bars indicate the estimated fracture orientation.

The estimated $\delta^{(v)}$ for the most area is about -15%, which is close to the $\delta^{(v)}$ of the model (-13.5%). There are some variations of the estimated $\delta^{(v)}$. The edge effect of the migration causes the high $\delta^{(v)}$ around the edges. On the top of the dome and the fault, the $\delta^{(v)}$ values are lower. A constant thickness of the fractured zone (605 m) is used in the calculation. In the area of the top of the dome and the fault the thickness used in calculation is larger than the true thickness, so that the $\delta^{(v)}$ is underestimated. In the area with steep structure, the estimated $\delta^{(v)}$ is small, because the migration fails at high dip for this particular case. Since the data are separated into 8 sectors and the normal CMP fold are only 48 for this modeling data, the fold is only about 6 for each sector in average. Therefore, the migration noise is a big concern. To eliminate the migration noise, the migration dip is limited to 45^{o}.

4.4 Conclusions

The workflow for fracture analysis that was developed in chapter 3 works very well on the physical modeling data. The fracture reflectivity shows up on both top and bottom of the fractured zone. In the structural areas, the fracture reflectivity appears in correct position. From the amplitude method and δ inversion, the estimated fracture orientations give the correct answer when taking the 90^{o} ambiguity into account. The estimated Thomsen's parameter, $\delta^{(v)}$, is reasonable, except on the edges of the model and around the steep reflectors. Migration noise is the cause for the low quality on the steep structure.

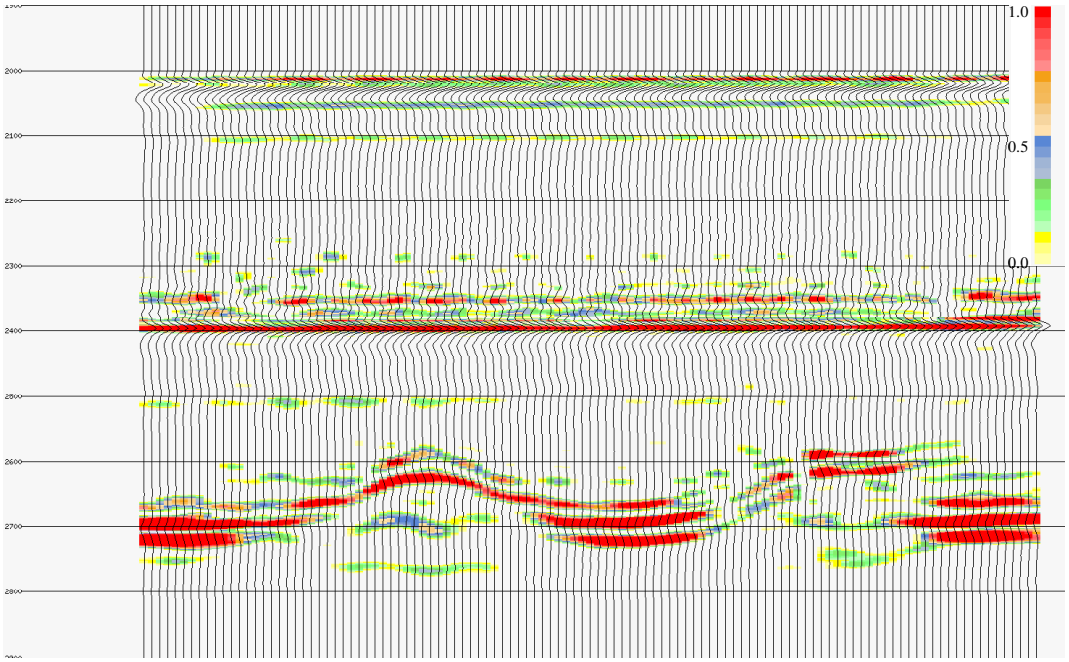

Figure 4.8. A profile of fracture reflectivity (color) from prestack migrated gathers. The background wiggle traces are migrated stack.

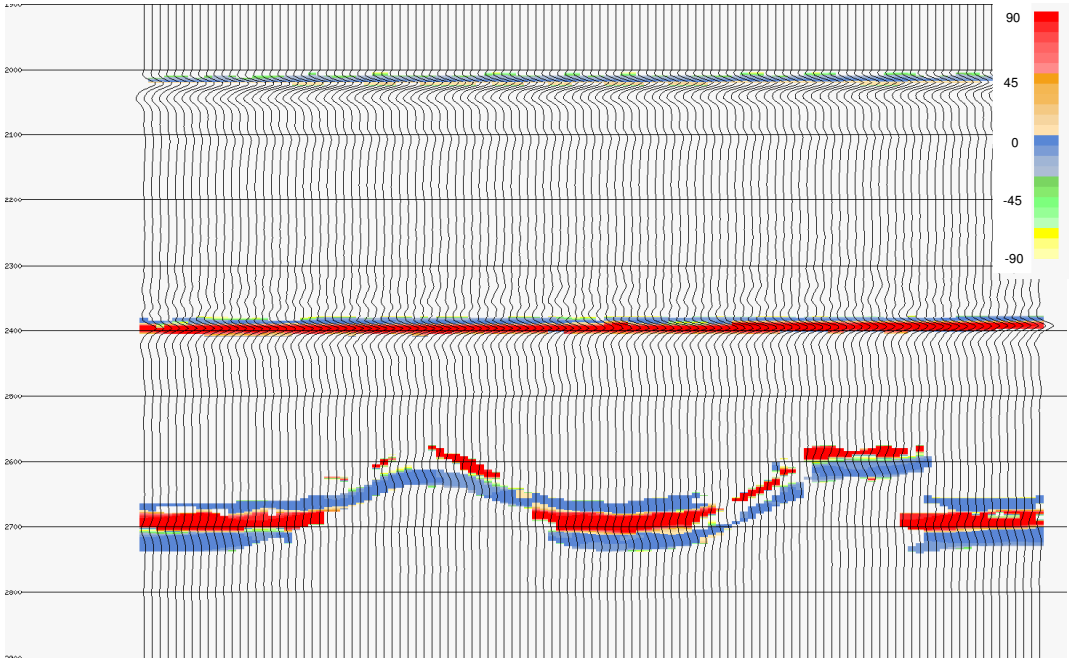

Figure 4.9. A profile (same line as Figure 4.8) of fracture orientation (color) from prestack migrated gathers. The background wiggle traces are migrated stack.

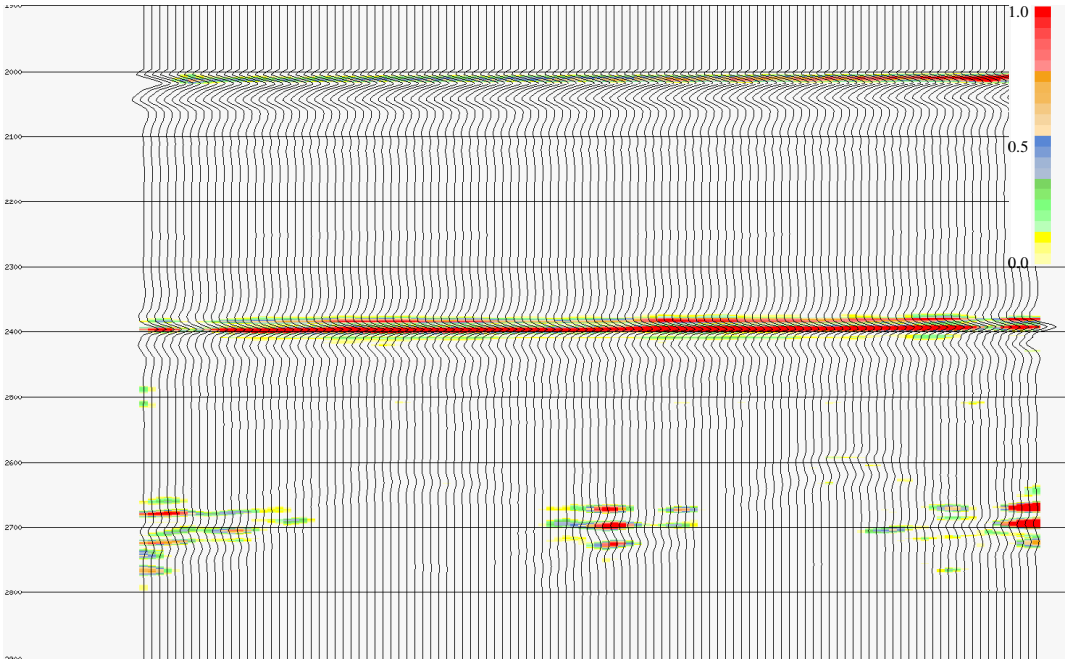

Figure 4.10. Fracture reflectivity (color) and stacked traces (wiggle) from the unmigrated gathers. The base of the fractured zone is not imaged correctly.

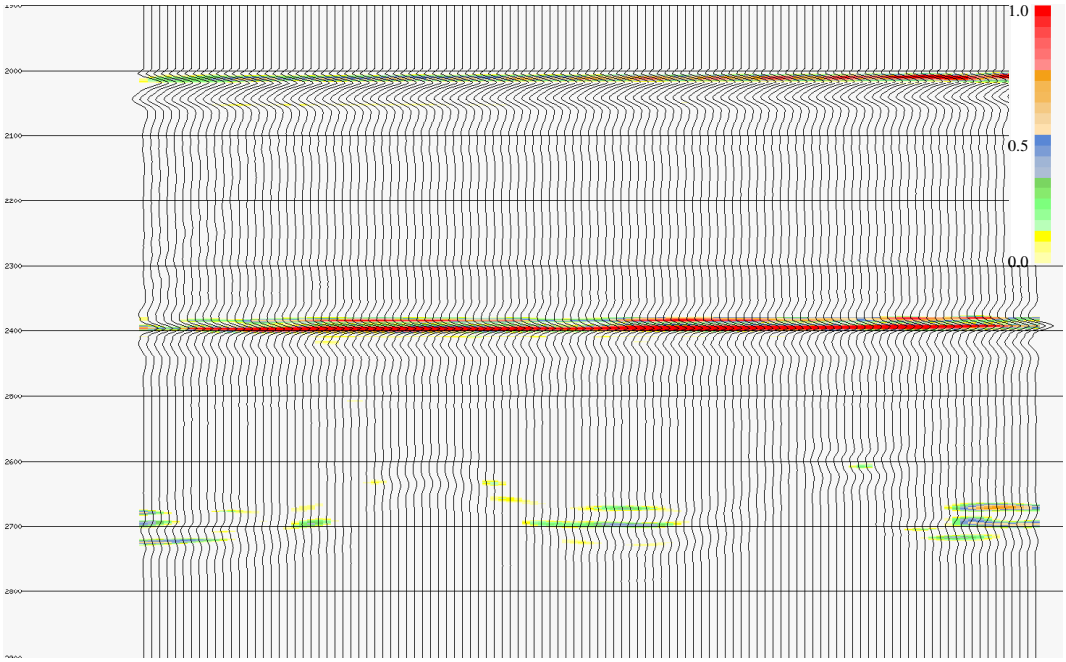

Figure 4.11. The post stack migrated fracture reflectivity (color) and stack (wiggle). They are better than that in the Figure 4.10, but still not right.

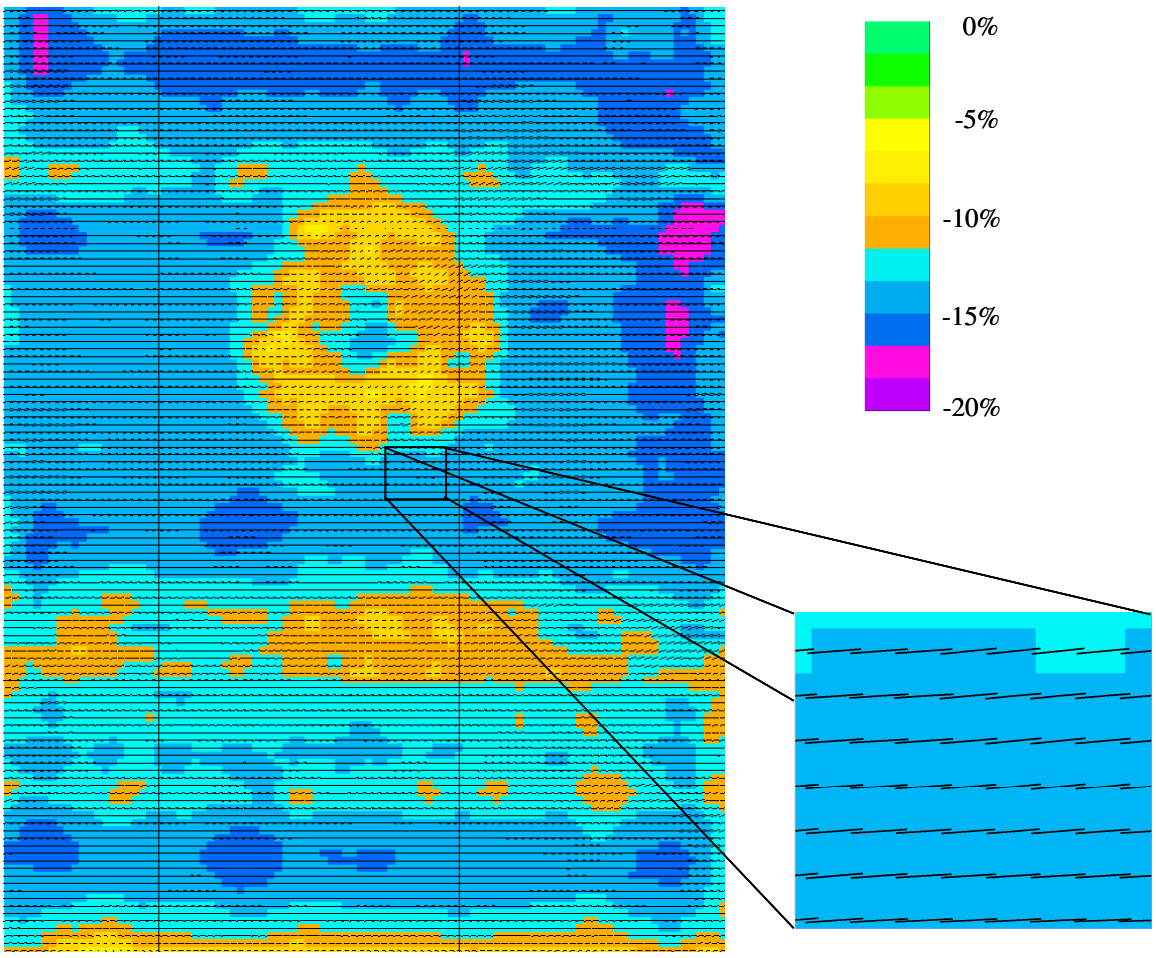

Figure 4.12. The distribution map of the Thomsen's parameter, $\delta^{(v)}$, extracted from the residual moveout on the base of the fractured zone. Except the edges, the $\delta^{(v)}$ value is -15%, close to the $\delta^{(v)}$ of the model (-13.5%). On the tops of the dome and fault, the $\delta^{(v)}$ is smaller, because the thickness of the fractured zone is less than unstructured area and constant thickness is used in the calculation.

Chapter Five: Application of fracture analysis to field data

5.1 Introduction to the Pinedale field

The Pinedale Anticline (Figure 5.1) in Wyoming, USA has been estimated to contain 159 TCF of in-place sweet gas (Law and Spencer, 1989), of which less than 1% has been produced. Pinedale and the adjacent Jonah field are the fastest growing producing fields in the American Rocky Mountains. The reservoirs currently of interest in the Pinedale Anticline are the tight sands of the Lance and Mesaverde Formations (Figure 5.2). These units were deposited during a period of rapid sedimentation in the late Cretaceous. Sediments were eroded off the western upland and carried by fluvial systems flowing to the east. Lithologically, the Lance and Upper Mesaverde consist of fluvial channel sandstones and siltstones, floodplain shales, and minor coals. Single sandstone units average 25 feet thick (Bowker and Robinson, 1997; Montgomery and Robinson, 1997). As a result, the areal extent of these reservoirs tends to be limited, and individual reservoirs may not be commercial. However, when several of these sand bodies are stacked vertically, an amalgamated package can be as thick as 100 feet, and viable commercial wells may be drilled into these stacked sands. Through the entire sequence of more than 3000 feet, a vertical well may encounter up to 100 individual sandstone units. The Lance and Mesaverde were buried by up to 8000 feet of Tertiary section, which compressed these sands so that they are now tight sandstones with low permeability. Source rocks for these reservoirs include discontinuous coals and carbonaceous material in shales interbedded with the sandstones. The reservoir rocks have moderate porosity ranging from 8-12% and usually have low permeability unless enhanced by natural fractures. Evidence for the presence of natural fractures comes from higher production rates, seen in some of the wells in Pinedale and Jonah, for example the Antelope 15-4 (Shaul, 2000). These production rates would simply not be possible without some kind of permeability-enhancing mechanism such as natural fractures. Therefore, the key to producing economically from these formations in the Pinedale Anticline is to find areas where open natural fractures enhance the low permeability of

the reservoir rocks. If a well is drilled near a large swarm of natural fractures, then a hydraulic fracture treatment can connect the wellbore to a larger area of the reservoir (Gray et al., 2003).

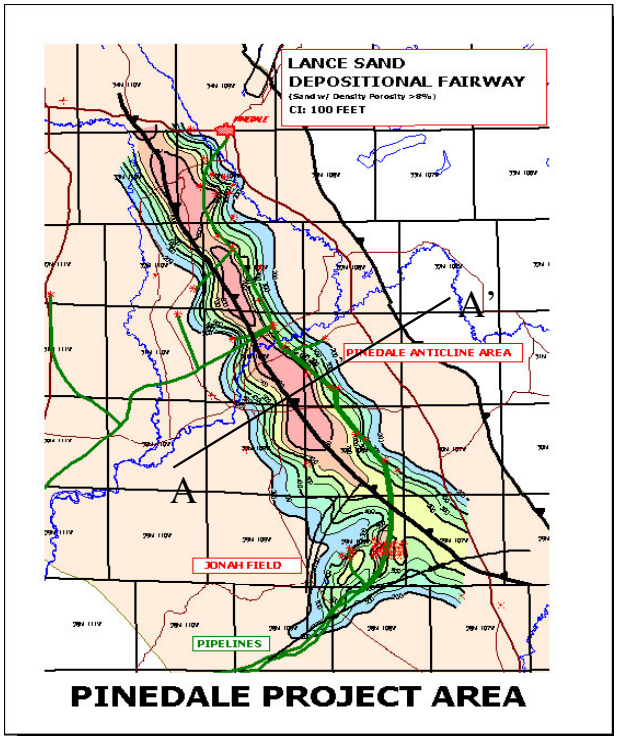

Figure 5.1. Map of the Lance Sand Depositional Fairway over the Pinedale Anticline (from Ultra Petroleum's webpage).

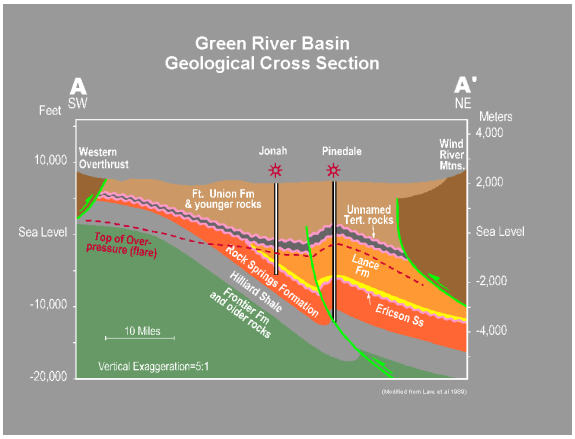

Figure 5.2. Geologic formations in the Pinedale Anticline (from Ultra Petroleum's webpage). The anticline is bordered by two thrust faults. The Lance sand depositional fairway is along the top of the anticline.

5.2 Seismic data processing and fracture analysis

A 3D seismic survey was shot by Veritas DGC Inc. in the Pinedale field, western Wyoming, USA. The survey area is about 324 square miles. The receiver lines run from southwest to northeast with the line interval of 1980 ft and receiver interval of 220 ft. Source lines are in zig-zag pattern. The source interval is 311 ft. The natural CMP bin size is 110 x 110 ft. The normal CMP fold is 55.

Some work has been done on fracture analysis with this dataset (Gray et al., 2003; Zheng and Gray, 2002). However, for these works, fracture analysis was applied in unmigrated gathers. To test the workflow presented in Chapter 3, a small area (about 50 square miles) was selected as a test area. The test area consists of 320 inlines and 360 cross lines. Since Pinedale is a commercially active area, according to the agreement with Veritas DGC Inc., the maps and sections being shown here are without any temporal and spatial references.

Following the workflow in Chapter 3, the seismic data were processed very carefully to ensure the amplitude preservation. The main processes applied before fracture analysis include spherical compensation, weathering statics, surface consistent deconvolution, surface consistent residual statics with a calculation window above the reservoir, band pass filtering and AVO compliant scaling. Then the gathers were divided into eight azimuthal cones, or sub-gathers, based on the acquisition azimuth (the shot-receiver direction). Area weighting was applied to the sub-gather in each cone to compensate for the geometry irregularity, before prestack common-angle time migration. After migration, all migrated gathers from eight cones were merged to form amplitude and azimuth preserved super gathers. Time variant residual statics were calculated, saved and applied to the super gathers to ensure seismic reflections are flat on each CMP gather. The amplitude method of fracture analysis was applied to the flattened gathers, and the δ inversion was applied to the saved residual statics from the bottom of the

reservoir for extracting the Thomsen's parameter, $\delta^{(v)}$. The results from both methods were correlated and verified with the production rates from wells.

5.3 Interpretation of the results from fracture analysis

Figure 5.3 is a map of the total fracture reflectivity over the entire thickness of the reservoir in the test area. The fracture reflectivity was measured from the incident-angle / azimuth variant amplitudes using the amplitude method. Most fractures occur in the area on the west side of the apex of the anticline (vertical purple line through well A) and stop at the thrust fault (dashed purple line on the left hand side of the map). There are some fractures on the east flank of the anticline. Most of them are on the lower portion of the map. There is secondary linear fractured zone from east to west on the top half of the map. This linear feature starts from the apex of the anticline and extends to east. Figure 5.4 show the Thomsen's parameter, $\delta^{(v)}$, measured from the residual moveout of the reflection on the bottom of the reservoir. The maximum $\delta^{(v)}$ is about 10%. The overall pattern of the $\delta^{(v)}$ distribution is similar to the distribution of the fracture reflectivity from the amplitudes (Figure 5.3). Again there are two linear features. The main feature is along the apex of the anticline, from the west side of the apex on the north to the east side of the apex on the south. A secondary feature is in east-west direction. It starts from the apex of the anticline on the top of the map and extends to the east direction.

Figure 5.5 shows the cross correlation of the fracture reflectivity of Figure 5.3 and the Thomsen's parameter, $\delta^{(v)}$, of Figure 5.4. The fracture correlation combines the information from both maps. However, for this project, the $\delta^{(v)}$ distribution contributes more to the correlation than the fracture reflectivity, because the contrast of the fracture reflectivity (Figure 5.3) is smaller than the contrast of $\delta^{(v)}$ (Figure 5.4).

Ten well locations are marked on the three maps. The size of the well symbol corresponds to the production rate of the well. The bigger the symbol is, the higher production rate the well has. The production rates of the 10 wells match the fracture

reflectivity in Figure 5.3 reasonably well. There is a very good matching between the production rates and the $\delta^{(v)}$ distribution in Figure 5.4 and the fracture correlation map in Figure 5.5. All good wells are located right on a highly fractured area or just on the edge of a highly fracture zone. The moderate wells are located on the relative low fractured area. The dry hole C is located on an area with no fracture at all. Well A has a higher production rate (0.4 bcf / year) than well B (0.07 bcf / year), because the $\delta^{(v)}$ value around well A is about 5%, fracture reflectivity is about 10000 and the correlation value is about 11000, all are higher than those around well B. There is a well only a few hundred feet north of well A, but its production rate (0.2 bcf / year) is lower than well A. This is because this well is on the edge of a fractured zone, while well A is right on the fractured zone.

Figure 5.6 shows an inline section (FF') through wells A and B. The wiggle traces are migrated stack, and overlaid color is the fracture reflectivity extracted from the amplitude of the seismic data. The red represents high fracture reflectivity, yellow is moderate, and green is low. From Figure 5.6, it is obvious why well A produced more gas than well B. Well A penetrated a large fractured zone and a few small fractured zones, although its depth is shallower than well B, while well B only penetrated a couple of small fractured zones. Figure 5.7 is another inline section (GG') that goes through well C. It is not a surprise why well C is dry, because it did not penetrate any fractured zones.

Figure 5.8 shows the fracture orientation detected by the amplitude method around well A. In the figure, there is a short bar plotted at each CMP bin. The directions of the short bars represent the estimated fracture orientation. The length of the bars and the background color correspond to fracture correlation as that in Figure 5.5. Figure 5.9 shows the fracture orientation detected from residual moveout and fracture correlation. The orientation in Figure 5.8 varies more often than that in Figure 5.9. However, the overall trend of the fracture orientations from these two methods is perpendicular to each other. As mentioned in Chapter 3, both amplitude method and δ inversion have 90^{o} ambiguity for the estimated fracture orientation. By taking this into account, these two

pictures are close to each other. Since there is no other more reliable information available for solving the ambiguity, the regional stress field might be helpful. Normally, fractures are opened if they are parallel to the major principal stress and closed if they are perpendicular to the major principal stress (Crampin and Leary, 1993; Crampin, 2000). By looking at the structural diagram (Figure 5.2), this area is a compressional area. The main force applied to the area is in southwest-northeast (SW-NE) direction, which causes the development of the anticlines and thrust faults, so that the direction of the major principal stress in this area is in SW-NE direction. Therefore the orientation given by the δ inversion is more likely to be true than what given by the amplitude method. Or the fracture orientation in Figure 5.8 needs 90^{o} rotation.

It is kind of unexpected at the first time to see the secondary fractured band in east-west direction in the area. There must be some geological reason for the linear feature. By looking into the migrated stack, it is found that there is a fault running from east to west and the fracture band is just on the fault. Figure 5.10 is a profile (EE' in Figure 5.3) of the migrated stack, where the fault is marked by a dashed line.

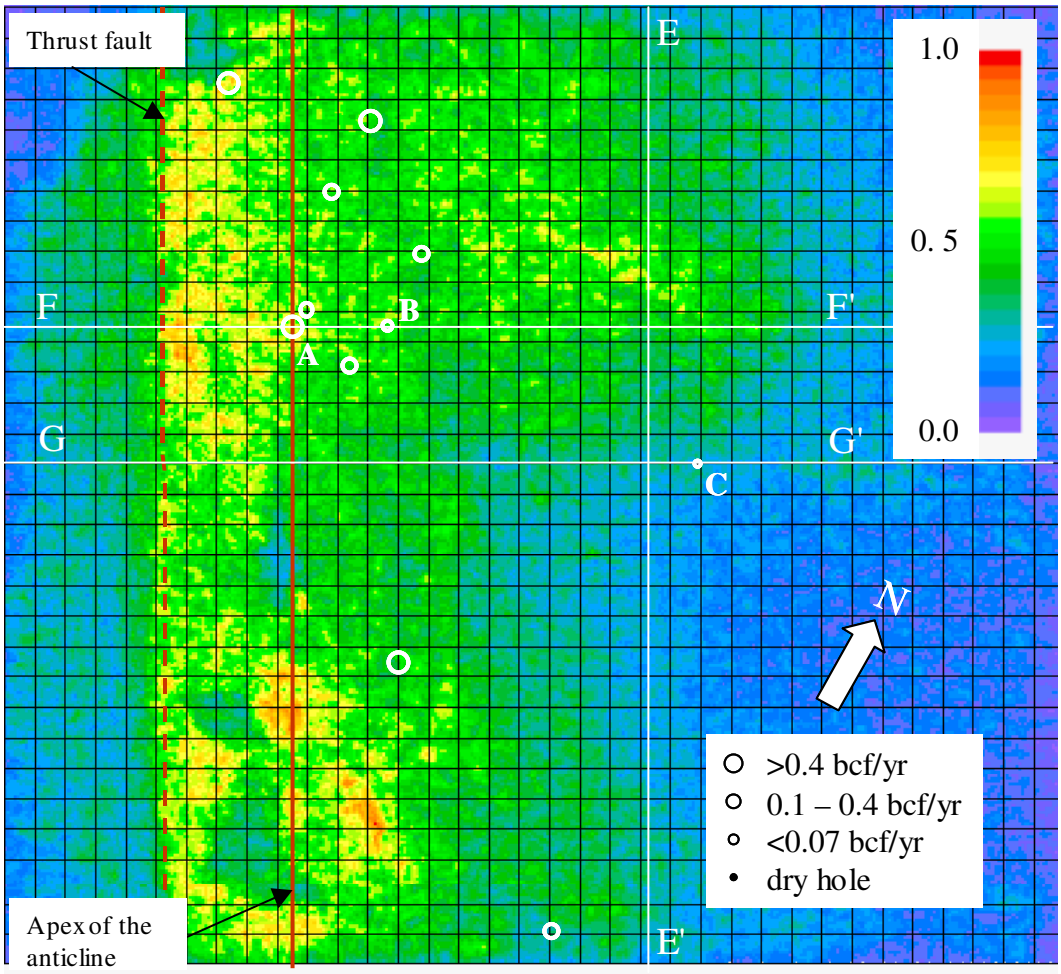

Figure 5.3. Map view of the overall fracture reflectivity through the entire reservoir. The fracture reflectivity is measured using the amplitude method. Ten well locations are marked on the map. The sizes of the circles correspond to the production rates of the wells. The production rates match the fracture reflectivity map reasonable well.

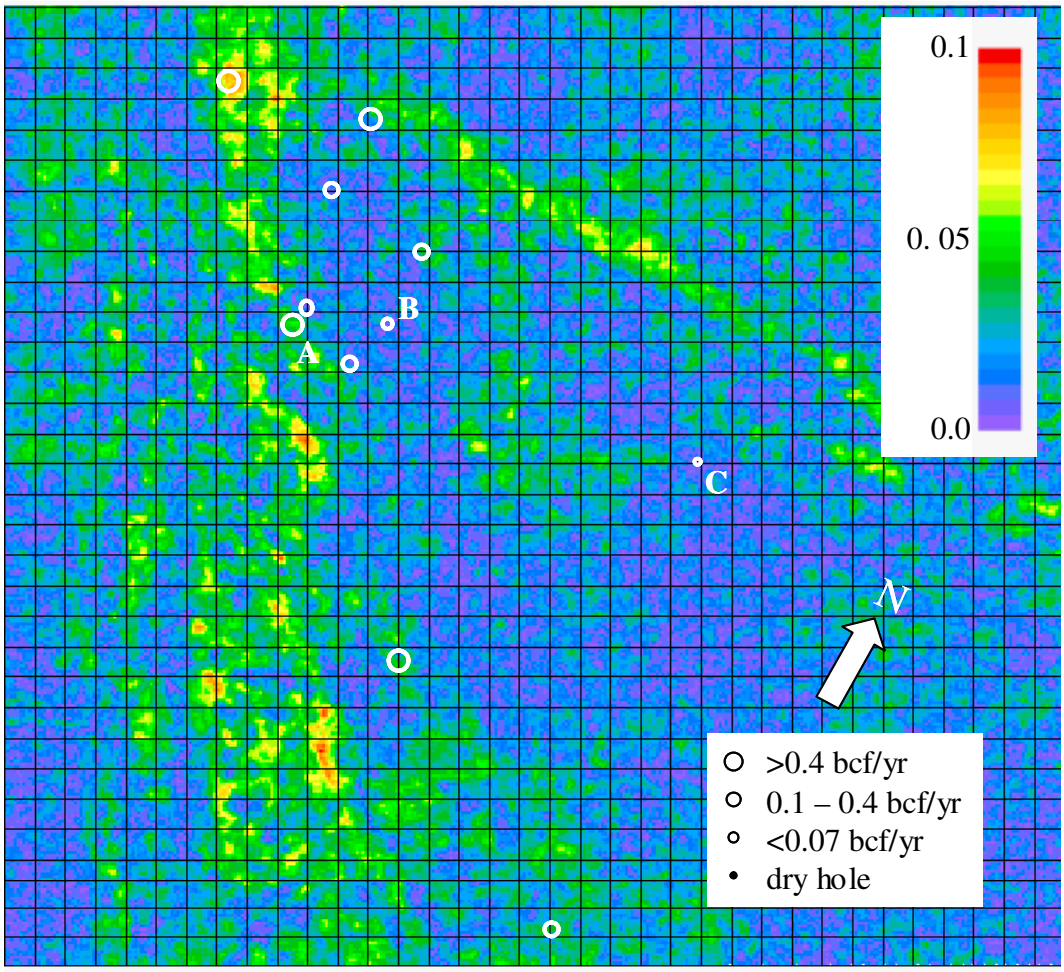

Figure 5.4. The map of the Thomsen's parameter, $\delta^{(v)}$, extracted from the residual moveout on the bottom of the reservoir. The values of $\delta^{(v)}$ correspond to the well production rates very well. Those wells with higher production rates locate in the area with higher $\delta^{(v)}$. Those with low production rates locate on the low $\delta^{(v)}$ area.

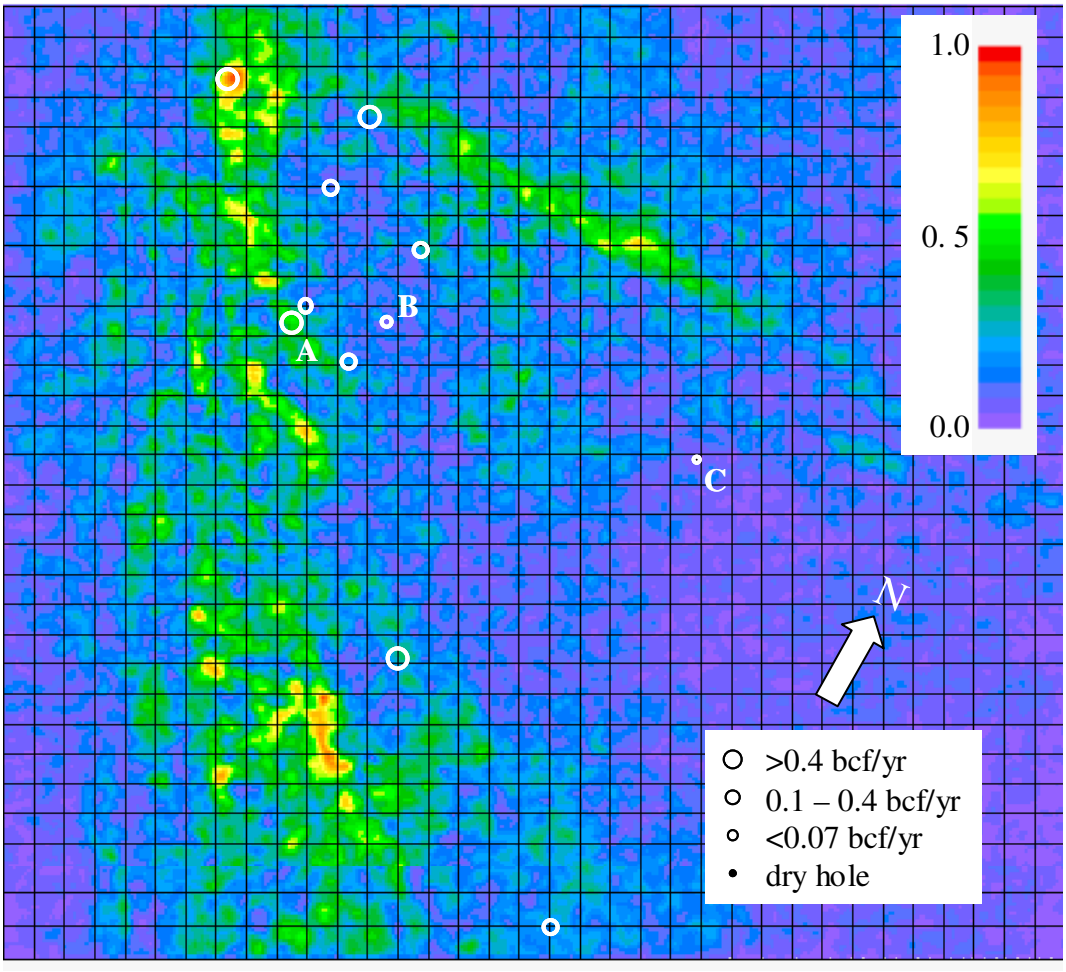

Figure 5.5. The map of the cross correlation of the fracture reflectivity extracted from the amplitude variation with incident-angle / azimuth and the Thomsen's parameter, $\delta^{(v)}$, extracted from the residual moveout on the bottom of the reservoir. The production rates of the 10 wells match this map very well.

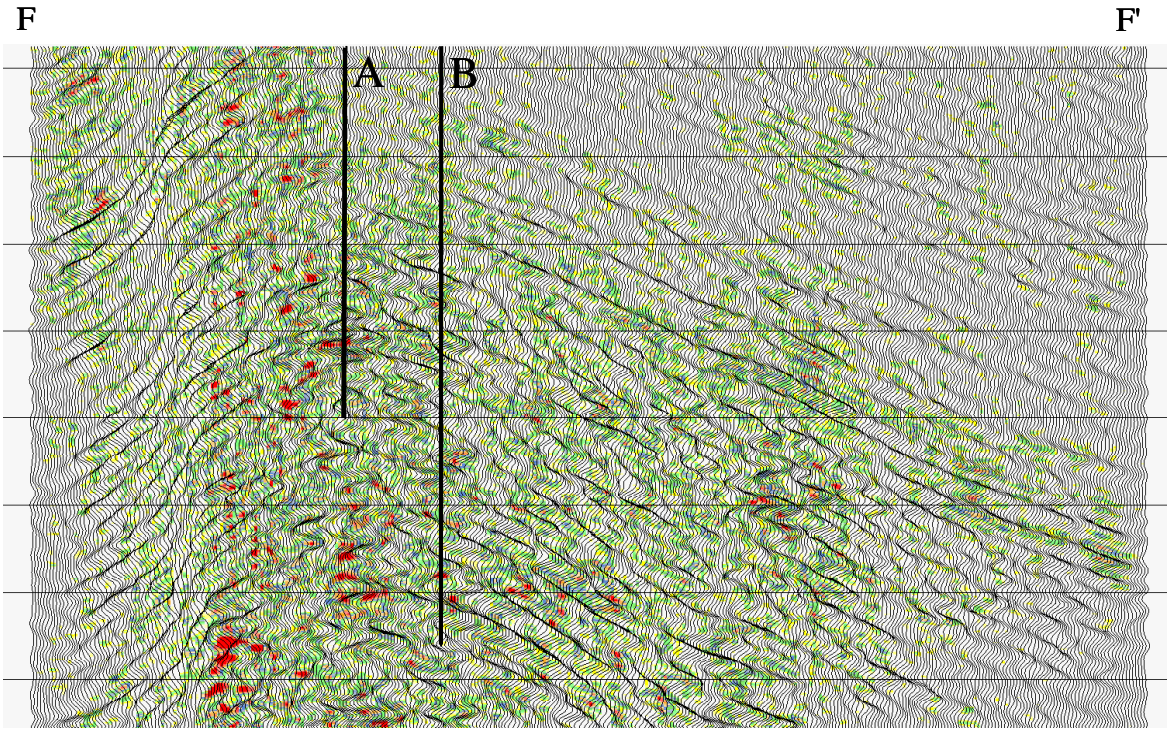

Figure 5.6. An inline section through wells A and B (FF'). Well A penetrated a large fractured zone and a few small fractured zones. Well B only penetrated a couple of small fractured zones. Therefore, well A has a higher production rate than well B.

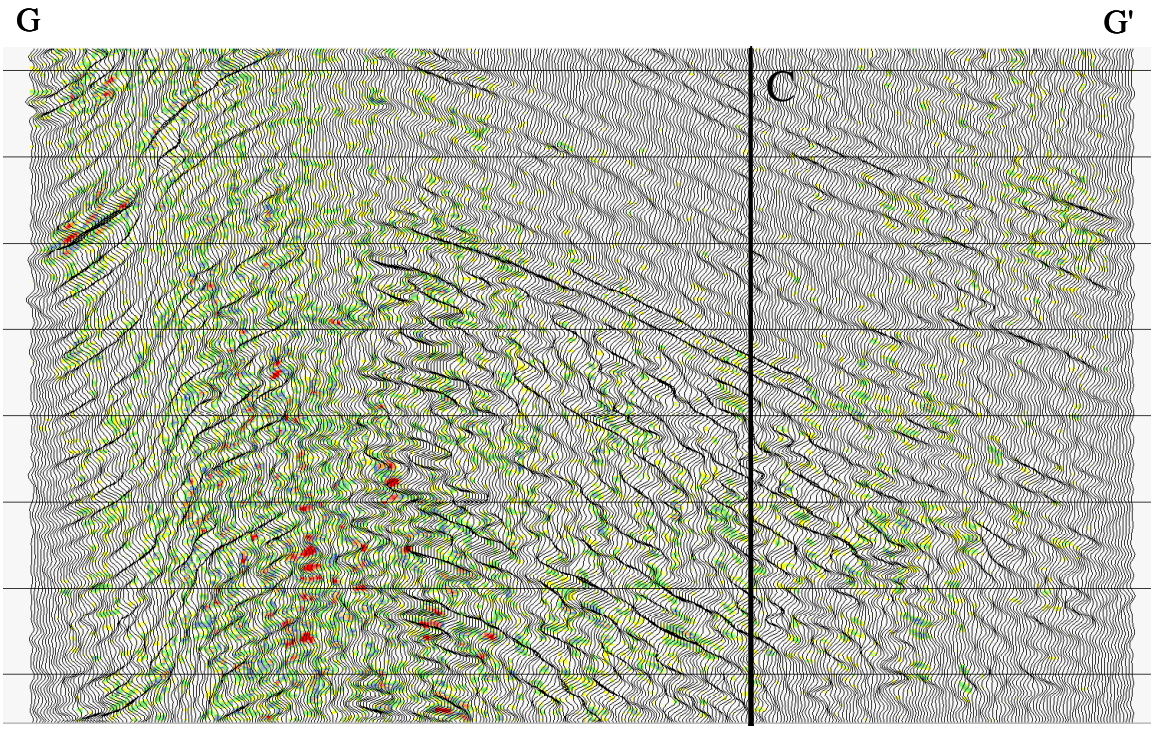

Figure 5.7. An inline section through well C (GG'). This well did not penetrate any fractured zones and produced nothing.

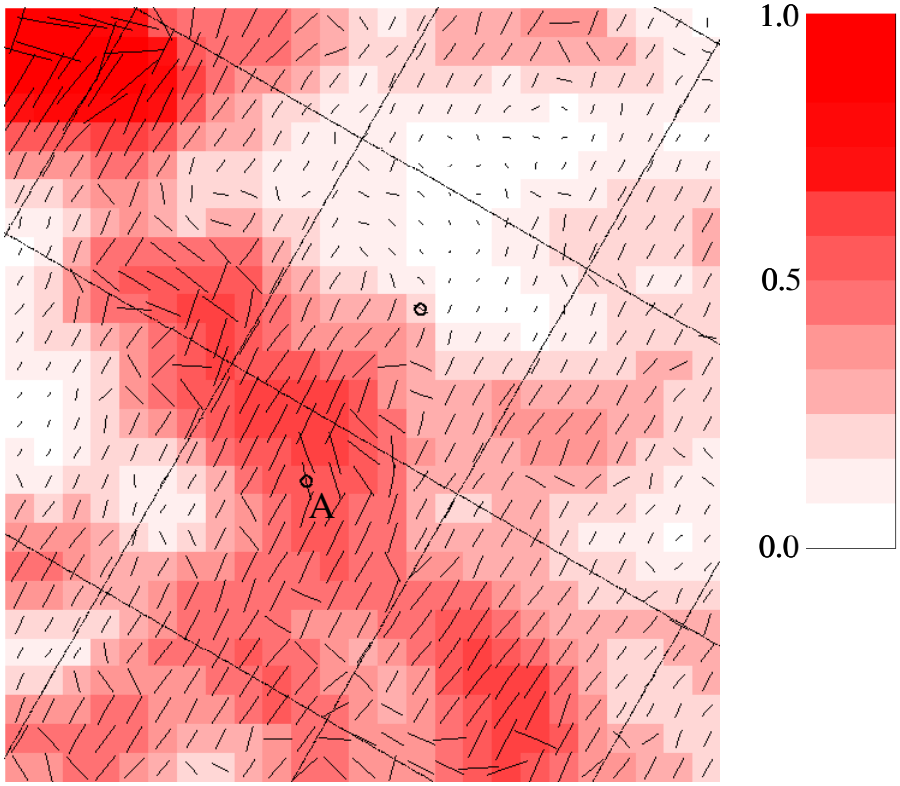

Figure 5.8. Fracture orientation detected by the amplitude method. The direction of the bars in each CMP bin shows the fracture orientation. The background color represents the correlation values as that in Figure 5.5.

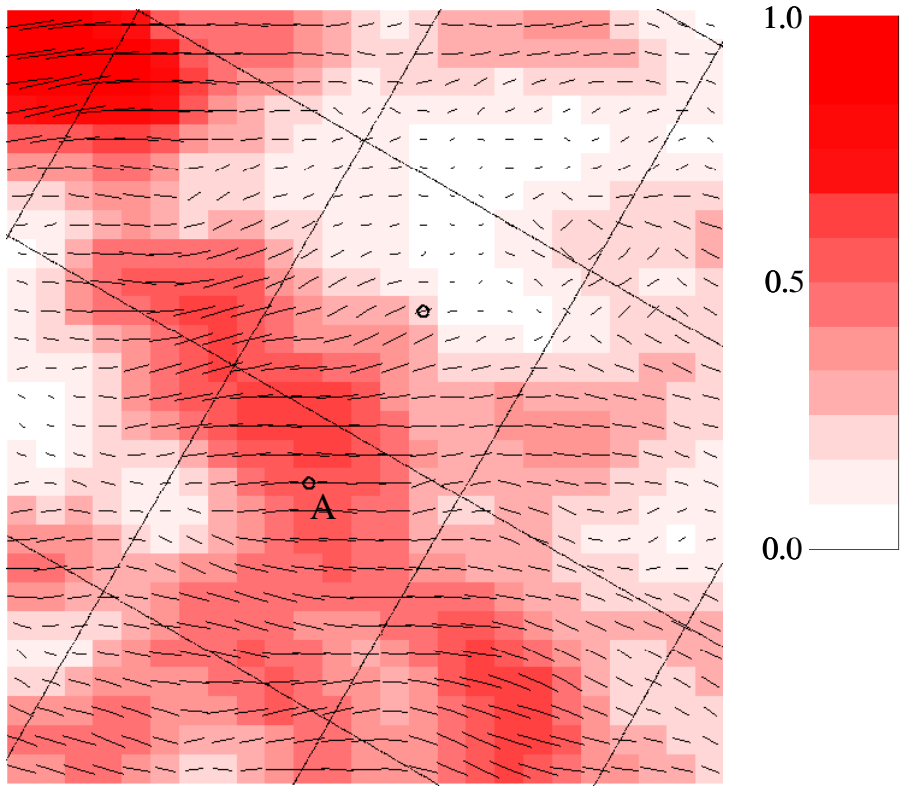

Figure 5.9. Fracture orientation detected by the δ inversion. The direction of the bars in each CMP bin shows the fracture orientation. The background color shows the correlation values as that in Figure 5.5.

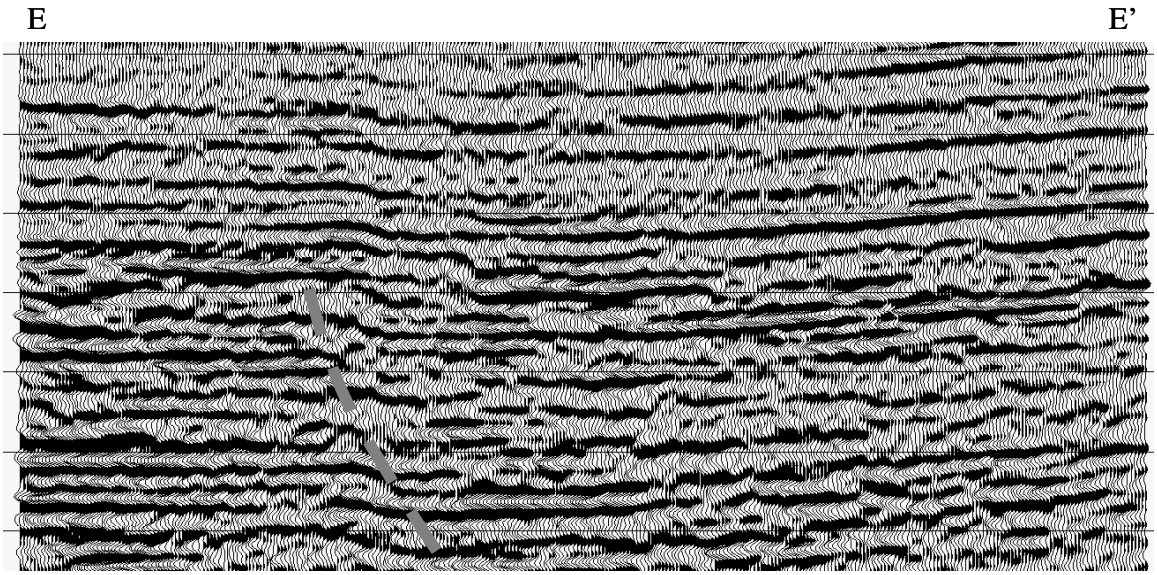

Figure 5.10. A cross line section of the migrated stack (EE' in Figure 5.3), with a fault marked by a dashed line. The location of the fault is the same as the secondary east-west fracture band.

5.4 Conclusions

Fracture analysis was applied to the test area in the Pinedale field. Both the amplitude method and the δ inversion were applied to extract fracture information. The distributions of fracture reflectivity and the Themson's parameter, $\delta^{(v)}$, were obtained, and are similar in major features. Well production rates match these two results. The wells with high production rates locate at the high fracture reflectivity and $\delta^{(v)}$ area. The dry well is at a location with very low fracture reflectivity and $\delta^{(v)}$. The correlation of these two maps provides another tool to check if both fracture reflectivity and $\delta^{(v)}$ are high.

The map of the Thomsen's parameter, $\delta^{(v)}$, provides the general information from the entire reservoir. While the fracture reflectivity provides detailed information at each time sample. These two attributes should be used together in interpretation.

Chapter Six: Conclusions and future work

6.1 Conclusions

Many of the oil and gas reservoirs in the world are fractured reservoirs. Therefore, it is important to understand the distribution and orientation of fractures for optimal development plans. Open fractures can not only provide pore space to hold oil and gas in place, but can also increase permeability to provide a pathway for fluid flowing from reservoir to well locations. When seismic waves travel through a fractured layer, or reflect from a boundary of a fractured layer, the amplitude and travel time will be affected. Thus, there is an opportunity for geophysicists to extract fracture information from seismic data.

There are at least three existing methods for fracture analysis in the oil and gas exploration industry by using PP reflection data; each method has its own advantages and disadvantages. The NMO velocity method and the moveout method measure the azimuthal anisotropy of P wave velocity. They are not sensitive to noise and the polarity of the data, but they can only detect fracture layers from their bottom interfaces, provided the fractured layers are thick enough to cause detectable travel time variation with azimuth. The other method is the amplitude method; it measures the impact of both P and S waves anisotropy and can detect fractured layers from the top and the bottom. However, it is relatively sensitive to noise and the polarity of the data.

The existing methods are adequate in general; but there are some limitations, as some factors influence the precision and accuracy of the results of fracture analysis. A dip reflector may induce “false” azimuthal anisotropy of the seismic amplitudes. Furthermore, in structural areas, detecting fractures from unmigrated CMP gathers will misposition fracture information. Therefore, migration must be incorporated into fracture analysis. The widely used common-offset migration will smear the incident angles. This problem can be solved by common-angle migration. Prestack common-angle time

migration was developed by the author and tested on synthetic and field data. It solves smearing of incident angle, mispositioning and dip induced "false" anisotropy simultaneously. It creates better image than the conventional common-offset migration, and is cost-effective compared to common-angle depth migration.

As an integration of the NMO velocity method and the moveout method, a new method, δ inversion, was developed by the author. It is a method to invert the Thomsen's parameter, $\delta^{(v)}$, from the residual moveout on the base of the fractured layer. The δ inversion was applied to physical modeling data and field data; the inverted values of $\delta^{(v)}$ are reasonable.

The estimated fracture orientation from the above three methods is not unique. It could be correct or off by 90^{o}. Integrating other information, such as FMI log, can solve this 90^{o} ambiguity.

A practical workflow for fracture analysis from PP reflection data is presented in this dissertation. Both amplitude method and δ inversion are employed in the workflow. The outputs of the workflow are four data volumes: (1) fracture reflectivity, (2) distribution of Thomsen's parameter, $\delta^{(v)}$, (3) fracture orientation from the amplitude method, and (4) fracture orientation from δ inversion. The fracture reflectivity gives detailed information on every time sample. In contrast, the distribution of $\delta^{(v)}$ gives the information for the entire fractured layer. These two products can be used together to produce a cross correlation of the total fracture reflectivity over the entire reservoir and the $\delta^{(v)}$ distribution. This correlation highlights the areas where both $\delta^{(v)}$ and fracture reflectivity are high. The fracture orientation from both methods should be almost parallel or perpendicular (because of the 90^{o} ambiguity). Otherwise, the whole processing should be reviewed carefully. This workflow was applied to both physical modeling data and field data. The results from modeling data match the original model and the results from the field data match the well production rates.

6.2 Future work

To solve the 90° ambiguity of the estimated fracture orientation, other information is needed. In this dissertation, examples are given to solve the problem with the help of FMI log and regional stress field. For future work, one possible approach is to apply inversion on different azimuths to find out the direction of the fast shear wave. This direction is the strike direction of the fractures. The procedure for multi-azimuth inversion may be: (1) applying AVO inversion on the migrated gathers on each azimuth cone by using GeoGain function (Smith and Gidlow, 1987) to get azimuthal dependent S wave reflectivity in PP time; (2) with a model built from sonic logs, applying acoustic inversion to the S wave reflectivity on each cone to get the S impedances at different azimuths; (3) comparing the S wave impedance at the different azimuths to find fast S and slow S wave directions. The fast S wave direction is the direction of the fracture strike. The relative difference of the velocities of the fast and slow S waves is the fracture density.

If possible, multi-component seismic data should be used for fracture analysis. The fast S wave direction can be found from shear wave splitting analysis. Hence, the Thomsen's parameter, $\gamma^{(v)}$, can be calculated from the difference of the fast and slow wave velocities. Combined with the δ inversion from the vertical component data, both $\delta^{(v)}$ and $\gamma^{(v)}$ can be quantified. The 90° ambiguity of the fracture orientation can also be solved. Therefore, it is optimal to use both PP and PS data for fracture analysis.

References

Aguilera, R., 1995, Naturally fractured reservoirs: Second edition, PennWell Publishing Company.

Alford, R. M., 1986, Shear data in the presence of azimuthal anisotropy: 56th Ann. Internat. Mtg., Soc. of Expl. Geophys., 476 – 479.

Backus, G.E., 1962, Long-wave elastic anisotropy produced by horizontal layering: J. Geophys. Res., **67**, 4427 - 4440.

Bowker, K.A. and Robinson, J.W., 1997, Jonah Field: A Shallow Sweetspot in the Basin-Centered Gas Accumulation of the northern Green River Basin, Wyoming, American Association of Petroleum Geologists Bulletin, **81**, 1219.

Bullen, K.E. and Bolt B. A., 1985, An introduction to the theory of seismology, 4th edition: Cambridge University Press.

Castagna, J.P. and Swan, H.W., 1997, Principles of AVO crossplotting: The Leading Edge, **16**, No. 4, 337 – 342.

Castagna, J.P., Swan, H.W. and Foster, D.J., 1998, Framework for AVO gradient and intercept interpretation: Geophysics, **63**, 948 – 956.

Chaimov, T.A., Beaudoin, G.J., Haggard, W.W., Mueller, M.C. and Thomsen, L.A., 1995, Shear-wave anisotropiy and coalbed methane productivity: 65th Ann. Internat. Mtg., Soc. of Expl. Geophys., 305-308.

Chapman, M. and Liu, E., 2004, Frequency dependent azimuthal amplitude variations in reflections from a fractured layer: 74th Ann. Internat. Mtg., Soc. of Expl. Geophys., 151-154.

Chen, H, Brown, R.L. and Castagna, J.P., 2005, AVO for one- and two-fracture set models: Geophysics, **70**, No. 2, C1 - C5.

Chi, X., He, Z. and Huang, D., 2004, The detection of seismic fractured zone by bispectrum and time-frequency analysis: 74th Ann. Internat. Mtg., Soc. of Expl. Geophys., 187-190.

Craft, K.L., Mallick, S., Meister, L.J. and Van Dok, R., 1997, Azimuthal anisotropy analysis from P-wave seismic traveltime data: 67th Ann. Internat. Mtg., Soc. of Expl. Geophys., 1214 – 1216.

Crampin, S., 2000, The potential of shear-wave splitting in a stress-sensitive compliant crust: a new understanding of pre-fracturing deformation from time-lapse studies: 70th Ann. Internat. Mtg., Soc. of Expl. Geophys., 1520-1523.

Crampin, S., Evans, R., Üçer, B., Doyle, M., Davis, J.P., Yegorkina, G.V. and Miller, A., 1980, Observations of dilatancy-induced polarization anomalies and earthquake prediction: Nature, **286**, 874 – 877.

Crampin, S. and Leary, P. C., 1993, Limits to crack density: the state of fractures in crustal rocks: 63rd Ann. Internat. Mtg., Soc. of Expl. Geophys., 758 – 761.

Dix, C. H., 1955, Seismic velocities from surface measurements: Geophysics, **20,** 68-86.

Gaiser, J.E., 2000, Advantages of 3-D PS-wave data to unravel S-wave birefringence for fracture detection: 70th Ann. Internat. Mtg., Soc. of Expl. Geophys., 1201 - 1204.

Garotta, R., 1989, Detection of azimuthal anisotropy: 59th Ann. Internat. Mtg., Soc. of Expl. Geophys., 861 – 863.

Gray, F.D., Boerner, S., Todorovic-Marinic, D. and Zheng, Y., 2003, Analyzing fractures from seismic for improvedfrilling success: World Oil, October, 62 – 69.

Gray, F.D. and Head, K., 2000, Fracture detection in the Manderson Field: A 3-D AVAZ case history, 70th Ann. Internat. Mtg., Soc. of Expl. Geophys., 1413-1416.

Gray, F.D., Todorovic-Marinic, D. and Lahr, M., 2002, Seismic Fracture Analysis on the Pinedale Anticline: Implications for Improving Drilling Success: 72nd Ann. Internat. Mtg., Soc. of Expl. Geophys., 532-535.

Gray, S. H., 1992, Frequency-selective design of the Kirchhoff migration operator: Geophys. Prosp., **40,** 565-572.

Grechka, V. and Tsvankin, I., 2002, Feasibility of Seismic Characterization of Multiple fracture sets: 72nd Ann. Internat. Mtg., Soc. of Expl. Geophys., 1646-1649.

Hall, S. A. and Kendall, J-M., 2003, fracture characterization at Valhall: Application of P-wave amplitude variation with offset and azimuth (AVOA) analysis to a 3D ocean-bottom data set: Geophysics, **68**, 1150 – 1160.

Helbig, K., 1984, Anisotropy and dispersion in periodically layered media: Geophysics, **49,** 364 - 373.

Johansen, T.A., Jakobsen, M, Agersborg, R. and Ruud, B.O., 2004, The P-P and P-S response of a fractured reservoir: 74th Ann. Internat. Mtg., Soc. of Expl. Geophys., 199-202.

Law, B.E. and C.W. Spencer, 1989, Geology of tight gas reservoirs in the Pinedale Anticline area, Wyoming, and the Multiwell Experiment site, Colorado: U.S. Geological Survey Bulletin 1886.

Lefeuvre, F., Nicoletis, L., Ansel, V. and Cliet, C., 1992, Detection and measure of the shear-wave birefringence from vertical seismic data: theory and applications, Geophysics, **57**, 1463 – 1481.

Levin, F.K., 1971, Apparent velocity from dipping interface reflections: Geophysics, **36**, 510-516.

Li, X. -Y., 1999, Fracture detection using azimuthal variation of P-wave moveout from orthogonal seismic survey lines: Geophysics, **64,** 1193-1201.

Lumley, D. E., Claerbout, J. F. and Bevc, D., 1994, Anti-aliased Kirchhoff 3-D migration, 64th Ann. Internat. Mtg: Soc. of Expl. Geophys., 1282-1285.

Luo, M. and Evans, B.J., 2004, An amplitude-based multiazimuth approach to mapping fractures using P-waver 3D seismic data: Geophysics, **69**, 690 - 698.

Lynn, H.B. and Thomsen, L., 1990, Reflection shear-wave data collected near the pricipal axis of azimuthal anisotropy: Geophysics, **55**, 147 – 156.

Lynn, H.B., Simon, K.M., Bates, C. and Van Dok, R., 1996, Azimuthal anisotropy in P-wave (muiltiazimuth) data: The Leading Edge, **15**, No. 8, 923 – 928.

MacBeth, C. and Lynn, H., 2001, Mapping fractures and stress using full-offset full-azimuth 3D PP data, 71st Ann. Internat. Mtg., Soc. of Expl. Geophys., 110-113.

Mallick, S., Craft, K. L., Meister, L. J. and Chambers, R. E., 1998, Determination of the principal directions of azimuthal anisotropy from P-wave seismic data: Geophysics, **63**, 692 – 706.

Montgomery, S.L. and Robinson, J.W., 1997, Jonah Field, Sublette County, Wyoming: Gas production from overpressured Upper Cretaceous Lance Sandstones of the

Green River Basin, American Association of Petroleum Geologists Bulletin, **81**, 1049-1062.

Mueller, M., 1992, Using shear waves to predict lateral variability in vertical fracture intensity: The Leading Edge, **11**, No. 2, 29 – 35.

Nebrija, E.L., Naini, B.R. and Ahmed, S., 2004, Fracture characterization using transmitted shear waves in a 3C azimuthal offset VSP: 74th Ann. Internat. Mtg., Soc. of Expl. Geophys., 139 - 142.

Nelson, R.A., 2001, Geologic analysis of Naturally Fractured reservoirs: Second edition, Gulf Professional Pulishing.

Olofsson, B., Probert, T, Kommedal, J.H. and Barkved, O.I., 2003, Azimuthal anisotropy from the Valhall 4C 3D survey: The Leading Edge, **22**, No. 12, 1228 – 1235.

Parney, B., 2004, Interpreting seismic fracture indicators under geologic and engineering models: CSEG Nat. Convention.

Rüger, A., 1998, Variation of P-wave reflectivity with offset and azimuth in anisotropic media: Geophysics, **63,** 935 - 947.

Rüger, A., 2002, Reflection Coefficients and Azimuthal AVO Analysis in Anisotropic Media: Geophysical Monograph Series, Number 10, Soc. of Expl. Geophys.

Rutherford, S.R. and Williams, R.H., 1989, Amplitude-versus-offset variations in gas sands: Geophysics, **54**, 608 – 688.

Sayers, C.M., 2004, Seismic anisotropy of shales: What determines the sign of Thomsen's delta parameter: 74th Ann. Internat. Mtg., Soc. of Expl. Geophys., 103-106.

Shaul, R., 2000, Jonah field could hold $15 bilion in natural gas: Sublette County Journal, Vol. 5, No. 6.

Shuey, R.T., 1985, A simplification of Zoeppritz equations: geophysics, **50**, 609 – 614.

Smith, G. C. and Gidlow, P. M., 1987, Weighted stacking for rock property estimation and detection of gas: Geophys. Prosp., Eur. Assn. Geosci. Eng., **35,** 993-1014.

Teng, L. and Mavko, G., 1996, Fracture signatures on P wave AVOZ: 66th Ann. Internat. Mtg., Soc. of Expl. Geophys. 1818 – 1821.

Thomsen, L.A., 1986, Weak elastic anisotropy: Geophysics, **51**, 1954 – 1966.

Thomsen, L.A., 1988, Reflection seismology over azimuthally anisotropic media: Geophysics, **53**, 304 – 313.

Thomsen, L., Tsvankin, I. and Mueller, M. C., 1995 Layer-stripping of azimuthal anisotropy from reflection shear-wave data: 65th Ann. Internat. Mtg., Soc. of Expl. Geophys., 289-292.

Tsvankin, I., 1997, Reflection moveout and parameter estimation for horizontal transverse isotropy: Geophysics, **62,** 614-629.

Tsvankin, I., 2005, Seismic Signatures and Analysis of Reflection data in Anisotropic Media: Elsevier Ltd.

Van Dok, R.R., Gaiser, J.E. and Byerley, G., 2003, Near-surface shear-wave birefringence in the North Seaa: Ekofisk 2D/4C test: The Leading Edge, **22**, No. 12, 1236 – 1242.

Wang, S. and Li, X, 2003, Fracture detection using 3D seismic data: A physical modeling study: 73rd Ann. Internat. Mtg., Soc. Expl. Geophys., 2303-2306.

Xu, Y. and Lu, L., 1991, Analysis of azimuthal anisotropic P-wave reflection, 61st Ann. Internat. Mtg., Soc. of Expl. Geophys., 698-700.

Zheng, Y. and Gray, D., 2002, Integrating seismic fracture analysis with migration: 72nd Ann. Internat. Mtg., Soc. of Expl. Geophys., 1642-1645.

Zheng, Y., Gray, S., Cheadle, S. and Anderson, P., 2001, Factors affecting AVO analysis of prestack migrated gathers: 71st Ann. Internat. Mtg., Soc. of Expl. Geophys., 989-992

Zheng, Y., Todorovic-Marinic, D. and Larson, G., 2004, Fracture detection: ambiguity and practical solution: 74th Ann. Internat. Mtg., Soc. of Expl. Geophys., 1575-1578.

Zheng, Y. and Wang, S., 2005, Fracture analysis on prestack migrated gathers: A physical modeling study: presented at CSEG Nat. Mtg., Calgary, Canada.

List of publications

Gray, D., Boerner, S., Todorovic-Marinic, D. and Zheng, Y., 2003, Analyzing Fractures from Seismic for Improved Drilling Success: World Oil, October, 2003.

Gray, D., Boerner, S., Todorovic-Marinic, D. and Zheng, Y., 2003, Fractured Reservoir Characterization using AVAZ on the Pinedale Anticline, Wyoming: Recorder, CSEG, 28, No. 6.

Liu, Y., Chang, X., Liu, F. and Zheng, Y., 2002, Three-dimensional velocity image beneath the Kang-Dian tethyan tectonic zone of China: Can. J. Earth Sci., 39, 1517 – 1525.

Todorovic-Marinic, D., Gray, D., Zheng, Y., Larson, G. and Pelletier J., 2003, Envelope of Fracture Density: presented at CSEG Nat. Mtg., Calgary, Canada.

Todorovic-Marinic, D., Gray, D., Zheng, Y., Larson, G. and Pelletier J., 2003, Interpretation of the fractures using envelope of Fracture Density: presented at the 1st International Congress of Geosciences for the Oil Industry and XI Symposium of Geophysics and Exposition, Cancun, Mexico.

Todorovic-Marinic, D., Larson, G., Gray, D., Cheadle, S., Soule, G. and Zheng, Y., 2004, Identifying vertical Productive Fractures in the Narraway Gas Field using the Envelope of the Anisotropic gradient: First Break, **22**, 10, 45 – 50.

Zheng, Y. and Gray, D.F., 2002, Integrating seismic fracture analysis with migration: 72nd Ann. Internat. Mtg., Soc. of Expl. Geophys., 1642-1645.

Zheng, Y. and Gray, D.F., 2002, Migrating Fracture Attributes: presented at CSEG annual convention: presented at CSEG Nat. Mtg., Calgary, Canada.

Zheng, Y. and Wang, S., 2005, Fracture analysis on prestack migrated gathers: A physical modeling study: presented at CSEG Nat. Mtg., Calgary, Canada.

Zheng, Y., 2000, Migration redatuming and velocity conversion: 70th Ann. Internat. Mtg., Soc. of Expl. Geophys., 501-504.

Zheng, Y., Gray, S., Cheadle, S. and Anderson, P., 2001, Factors affecting AVO analysis of prestack migrated gathers: 71st Ann. Internat. Mtg., Soc. of Expl. Geophys., 989-992.

Zheng, Y., Roberts, G. and Ratcliffe, A., 2003, High resolution residual velocity analysis and application: presented at CSEG Nat. Mtg., Calgary, Canada.

Zheng, Y., Todorovic-Marinic, D. and Larson, G., 2004, Seismic Fracture Detection: Ambiguity and practical solution: 74th Ann. Internat. Mtg., Soc. of Expl. Geophys., 1575-1578.

APPENDIX A: ELASTIC STIFFNESS MATRIX AND THOMSEN'S PARAMETERS

After Bullen and Bolt (1985) and Thomsen (1986), both stress and strain have nine components. For linear materials, the relationship between stress and strain is:

$$\sigma_{ij} = \sum_{k=1}^{3}\sum_{l=1}^{3} C_{ijkl}\varepsilon_{kl}, i, j = 1,2,3 \qquad \text{(A1)}$$

where σ_{ij} is a 3x3 stress tensor, ε_{kl} is a 3x3 strain tensor, C_{ijkl} is a 3x3x3x3 stiffness tensor. Both axes x_1 and x_2 are horizontal (x_1 is parallel to the paper and x_2 is perpendicular to the paper), while axis x_3 is vertical. Because of the symmetry of stress ($\sigma_{ij} = \sigma_{ji}$) and strain ($\varepsilon_{kl} = \varepsilon_{lk}$), only six of the components of stress and strain are independent.

With a change of indices using Voigt recipe (Tsvankin, 2005; Thomsen, 1986),

ij	kl	11	22	33	32=23	31=13	12=21	
↓	↓	↓	↓	↓	↓	↓	↓	(A2)
α	β	1	2	3	4	5	6	

equation (A1) can be rewritten as:

$$\sigma_{\alpha} = \sum_{\beta=1}^{6} C_{\alpha\beta}\varepsilon_{\beta}, \alpha = 1,2,...,6 \qquad \text{(A3)}$$

where $C_{\alpha\beta}$ is a 6x6 stiffness matrix. Because it is a symmetrical matrix (Bullen and Bolt, 1985), there are only 21 independent elements.

For isotropic media, the stiffness matrix is:

$$\sigma_{\alpha\beta} = \begin{pmatrix} C_{33} & C_{33}-2C_{44} & C_{33}-2C_{44} & & & \\ C_{33}-2C_{44} & C_{33} & C_{33}-2C_{44} & & & \\ C_{33}-2C_{44} & C_{33}-2C_{44} & C_{33} & & & \\ & & & C_{44} & & \\ & & & & C_{44} & \\ & & & & & C_{44} \end{pmatrix} \qquad \text{(A4)}$$

where only nonzero elements are shown.

There are only two independent elements for isotropic media, C_{33} and C_{44}. These two elements can be replaced by the Lamé parameter, λ and μ, which are more widely used, and equation (A4) becomes:

$$\sigma_{\alpha\beta} = \begin{pmatrix} \lambda+2\mu & \lambda & \lambda & & & \\ \lambda & \lambda+2\mu & \lambda & & & \\ \lambda & \lambda & \lambda+2\mu & & & \\ & & & \mu & & \\ & & & & \mu & \\ & & & & & \mu \end{pmatrix} \qquad \text{(A5)}$$

VTI media can be considered as a stack of horizontally layered rocks (Figure A1). Their elastic properties are the same for different azimuthal angles, but different for the different ray angles with the vertical axis. HTI media can be considered as 90^o rotated (around a horizontal axis, say x_2). Figure A1 is the analogy of VTI and HTI media.

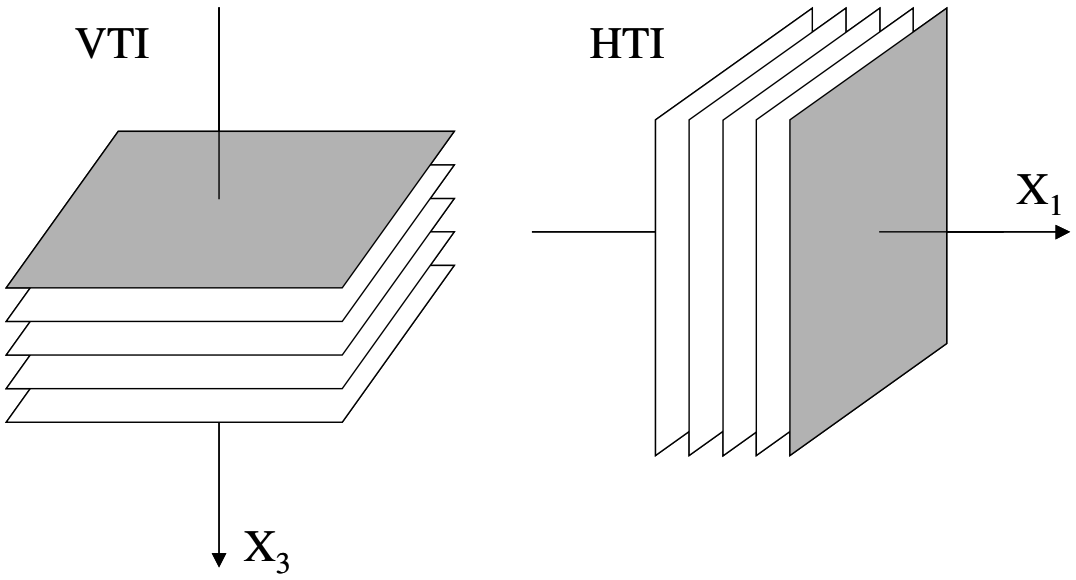

Figure A1. The analogy between VTI and HTI models helps to extend solutions for VTI to HTI media (After Rüger, 2002)

After Thomsen (1986) and Rüger (2002), the stiffness matrix for VTI media is:

$$\sigma_{\alpha\beta}^{VTI} = \begin{pmatrix} C_{11} & C_{11}-2C_{66} & C_{13} & & & \\ C_{11}-2C_{66} & C_{11} & C_{13} & & & \\ C_{13} & C_{13} & C_{33} & & & \\ & & & C_{44} & & \\ & & & & C_{44} & \\ & & & & & C_{66} \end{pmatrix} \quad \text{(A6)}$$

Thomsen's anisotropic parameters are defined as:

$$\varepsilon = \frac{C_{11}-C_{33}}{2C_{33}}$$
$$\delta = \frac{(C_{13}+C_{44})^2-(C_{33}-C_{44})^2}{2C_{33}(C_{33}-C_{44})} \quad \text{(A7)}$$
$$\gamma = \frac{C_{66}-C_{44}}{2C_{44}}$$

For HTI, compared to VTI, axes x_1 and x_3 are interchanged. Therefore, C_{11} and C_{33} are interchanged, and so on. The stiffness matrix becomes:

$$\sigma_{\alpha\beta}^{HTI} = \begin{pmatrix} C_{11} & C_{13} & C_{13} & & & \\ C_{13} & C_{33} & (C_{33}-2C_{44}) & & & \\ C_{13} & (C_{33}-2C_{44}) & C_{33} & & & \\ & & & C_{44} & & \\ & & & & C_{66} & \\ & & & & & C_{66} \end{pmatrix} \quad \text{(A8)}$$

Thomsen's parameters for HTI media have the same expression as VTI media, but traditionally, a superscript of $^{(v)}$ is added as $\varepsilon^{(v)}$, $\delta^{(v)}$ and $\gamma^{(v)}$.

APPENDIX B: CLASSIFICATION OF AVO RESPONSES

From different seismic interfaces, AVO (**A**mplitude-**V**ersus-**O**ffset) characteristics are different. Rutherford and Williams (1989) defined three types of AVO responses, Class I, II, and III. Later, Castagna and Swan (1997) defined another type of AVO response, Class IV. Currently, the classification of these four classes is widely used in industry. All the four classes are originally about a shale seal underlain by a sand reservoir with different impedance contrast. In practice, the classification of AVO responses is also used for the other types of geological interfaces. Figure B1 shows the amplitude variation with offset for different classes.

- **Class I**: Both P and S wave impedances in the underlying sand are higher than that of the shale. The sand is mature, and is compacted moderately to highly. In seismic response, there is a peak at near offset and the amplitude decreases with offset, with the possibility of polarity change if adequate offset range is available.

- **Class II**: The P wave impedance of the sand is about the same as the overlying shale, while the S wave impedance of the sand is higher than that of the shale. Typically, the sand is moderate compacted. This kind of interface produces weak amplitude at zero offset (either positive or negative). Amplitudes appear as a trough at far offset, and increase with offset. There may be a polarity change if the zero offset amplitude is positive, but usually it is not detectable, because it occurs at near offset where the signal is often below the noise level.

- **Class III**: The P wave impedance of the sand is lower than that of the shale, but S wave impedance is higher. The sand is typically unconsolidated. In seismic response, amplitudes start with a trough at near offset and increase to a stronger trough at far offset.

- **Class IV**: Both P and S wave impedance of the sand is lower than that of the shale. The sand is also unconsolidated. The seismic amplitude appears as a trough at near offset and decreases with offset. It becomes a weaker trough at far offset.

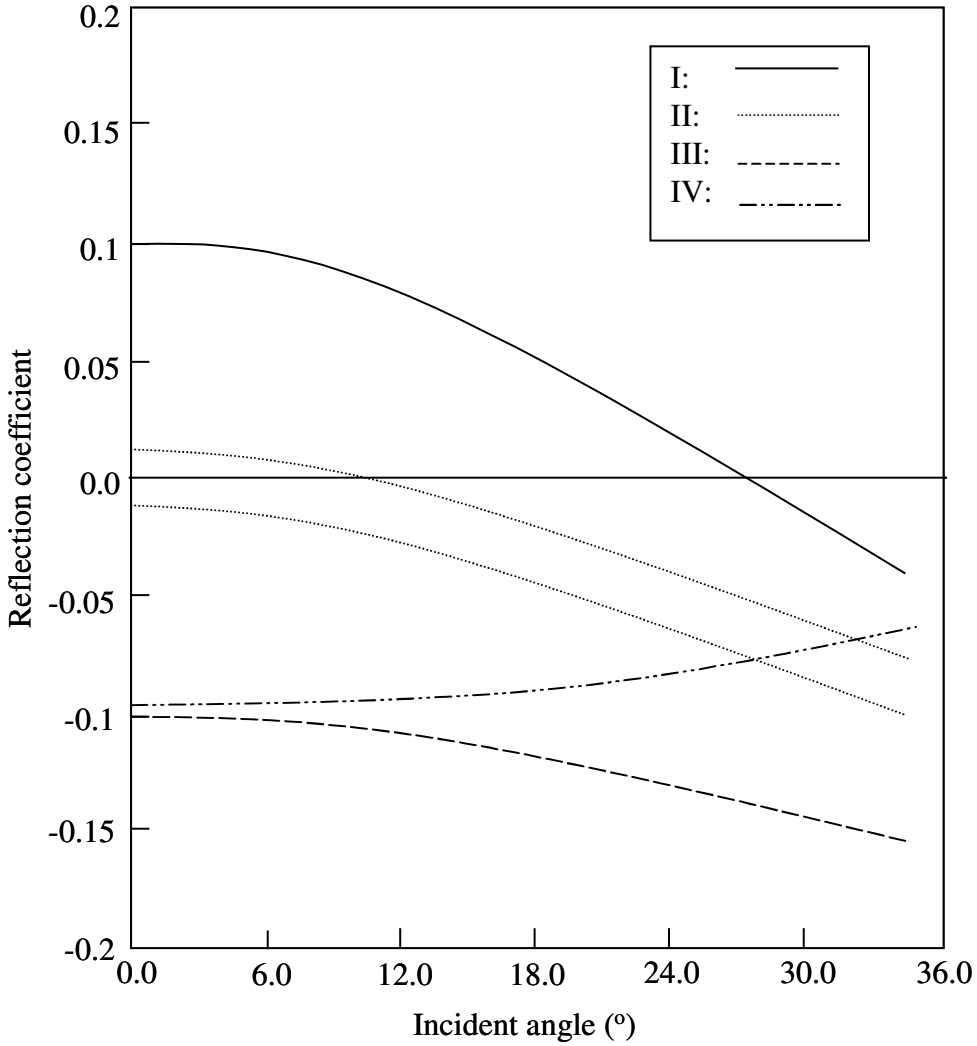

Figure B1. Amplitude variation with offset for all four classes of AVO responses. (After Rutherford and Williams, 1989; Castagna et al. 1998).